TRIBOLOGICAL STUDIES OF MICRO/NANOSCALE THIN SOLID FILMS

BY

JUNGKYU LEE

DISSERTATION

Submitted in partial fulfillment of the requirements
for the degree of Doctor of Philosophy in Mechanical Engineering
in the Graduate College of the
University of Illinois at Urbana-Champaign, 2012

Urbana, Illinois

Doctoral Committee:

Professor Andreas A. Polycarpou, Chair and Director of Research
Professor Lawrence A. Bergman
Professor John R. Abelson
Associate Professor Ioannis Chasiotis

Abstract

Use of thin films has received significant attention in recent years because of their advantages in controlling friction and wear of the bulk material. There have been significant advances in modern applications such as in magnetic disks for data storage and microelectromechanical systems (MEMS) with the introduction of thin solid films coated on substrates. However, due to harsh operating conditions and higher performance requirements, it is necessary to explore new materials and develop experimental and theoretical framework to better understand the coating system.

In this work, five different topics in regard to thin solid films have been studied. First, the adhesion behavior of thin film layers in contact with a solid under shearing motion was investigated. Experimental results of pull-off adhesive forces using various coating materials show that adhesion can be controlled by choosing different coating materials with the aid of appropriate shearing force. Second, the mechanical and tribological properties for a novel material, $La_5Ca_9Cu_{24}O_{41}$ (LCCO), were evaluated, revealing that LCCO can be an attractive candidate as a nanothermal layer showing good tribological characteristics as well as thermal properties. Third, the contact behavior of thin films coated on substrate was investigated using a nanoindentation tester and a dynamic stiffness tester. When a hard layer is coated on a soft substrate, both asperity interaction and soft substrate deformation should be considered. Fourth, the wear behavior of a layered sphere at the sliding inception was analyzed based on the finite element approach. The relationships among potential wear, material properties, and

normal load were obtained. Fifth, the yielding behavior of hafnium diboride (HfB_2) hard coatings was studied showing that plastic deformation at the interface was the dominant failure mechanism of the HfB_2 films.

Acknowledgements

I have worked with a number of excellent people in the last five years for my Ph.D. study. I am very pleased to thank the many people who have helped me complete my doctoral course and this thesis. First and foremost, I would like to express my deepest gratitude to my advisor Andreas A. Polycarpou for his continuous guidance and support of my Ph.D. study and research. His enthusiasm, wide knowledge, constructive comments and important support have been a great help during my doctoral research period. He could not have been a better professor and advisor for me.

My gratitude also goes to my research group members in the Microtribodynamics laboratory for their friendship, advice, discussion and all the things that I have had with them in the last five years, which will be in my memory forever. I would like to thank Raja Katta, Emerson Escorbar Nunez, Chang-Dong Yeo, Antonis Vakis, Melih Eriten, Nick Demas, Sujana Chandrasekar, Surya Mishra, Eric Gertner, Wasim Akram, Shahla Chowdhury and Seung Min Yeo. I would also like to thank all the other people who have helped me successfully finish my doctoral course in one or another way. In particular, I am very grateful to Professor John R. Abelson and Andrew Cloud in the department of material science and engineering for inspiring and leading me to the new field.

I would also extend my sincere thanks to the support of Seagate Technology LLC, National Science Foundation (NSF), Defense Advanced Research Projects Agency (DARPA). I would like to thank the National Center for Supercomputing Applications (NCSA) for providing me access to their computational resources.

Last but not least, I would like to thank my wife Younghee Song for her dedication, love, emotional support and unchanged confidence in me. Also, my adorable two daughters, Claire and Chloe, have been a great strength and energy to me during my doctoral research. My warmest thanks also go to my parents for their love and constant support.

Table of Contents

List of Figures

List of Tables

List of Symbols and Abbreviations

A	Contact area
AFM	Atomic force microscopy
A_n	Nominal contact area
arc-PVD	Cathodic arc deposition
a_y	Contact radius at critical interference
C	Function of the Poisson's ratio
COC	Carbon over coat
CVD	Chemical vapor deposition
d_c	Residual scratch track width
DLC	Diamond like carbon
E'	Combined modulus of two asperities
E^*	Combined modulus
E_f	Elastic modulus of film
E_i	Reduced elastic modulus of the indenter
E_r	Reduced elastic modulus
F	Force
FEA	Finite Element Analysis
FFT	Fast Fourier Transform
G_c	Energy release rate
H	Hardness
h	Wear depth
HAMR	Heat Assisted Magnetic Recording
h_c	Contact depth
HDI	Head Disk Interface
HMS	Head Media Spacing
HTT	High Temperature Tribometer

ICP	Inductively Coupled Plasma
ICP-DRIE	Inductively Coupled Plasma-Deep Reactive Ion Etching
K	Proportional constant
K_{ab}	Adhesive wear coefficient
K_c	Contact stiffness
K_w	Wear coefficient
L_c	Critical normal load
LCCO	$La_5Ca_9Cu_{24}O_{41}$
m	Mass
MEMS	Microelectromechanical System
P	Normal contact load
p	Normal contact pressure
P^*	Dimensionless normal load
PEEQ	Equivalent plastic strain
PLD	Pulsed laser deposition
p_m	Mean contact pressure
P_{max}	Peak indentation load
$P_{precursor}$	Precursor pressure
PR	Photoresist
PSA	Pressure Sensitive Adhesive
PZT	Lead Zirconate Titanate
R	Asperity radius
R_a	Radius of asperity
RMS	Root mean square
R_{pt}	Radius of pole tip
R_q	Root mean square roughness
S	Sliding distance
SEM	Surface Electron Microscope

SFA	Surface Force Apparatus
t	Film thickness
T_{sub}	Substrate temperature
UV	Ultra Violet
V	Wear volume
V_a^*	Dimensionless wear area for deformed asperity
V_c	Area of semicircle of protruded pole tip
V_s^*	Dimensionless plastically deformed are of substrate
V_w	Wear area
XRD	X-ray Diffractometer
Y_0	Yield strength
δ	Displacement
ζ_c	Damping constant
η	Areal density of asperities
μ	Friction coefficient
v	Poisson's ratio
v_i	Poisson's ratio of indenter
v_s	Poisson's ratio of substrate
σ_a	Adhesion strength at the interface
σ_c	Local stress
σ_{ij}	Normal stress
σ_{VM}	Von Mises stress
σ_y	Yield strength
τ_c	Shear strength at the interface
τ_{ij}	Shear stress
ψ	Plasticity index
ω_c	Critical interface at the inception of plastic deformation

1. Introduction

1.1. Overview

The study of friction, adhesion and wear has enormous practical importance, since the performance of many mechanical and electromechanical systems depends on appropriate friction and wear performance. Traditionally, the most common way of reducing friction and wear is introducing lubricants between the two moving parts together with design and selection of improved bulk materials. In modern applications such as microelectromechanical systems (MEMS) and magnetic storage head/disk interfaces, there is a need to reduce or control friction and wear under different working conditions. However, the use of liquid lubricants is limited for such applications as compared to other conventional types of devices. Another approach to friction and wear control is to utilize some sort of protective coatings.

The use of appropriate surface coatings might contribute to improving resistance to wear and achieve the required frictional characteristics that were not previously achievable because the surface is the most important part affecting contacting and sliding surfaces. Despite the fact that many tribologists have developed an understanding of the behavior of surfaces in contact, standard characterization methods are still not well established.

To make a further advancement in understanding of thin solid films for tribological applications, systematic investigations of the material behavior ranging from property measurements, friction, wear and adhesion behavior characterization, analytical

and computational modeling are necessary. This research deals with experimental work analyzing the adhesion behavior of thin films under dynamic motion, characterization of friction and wear behavior of new material such as magnetic mode oxide and hafnium diboride coatings. It also includes material property measurements, wear behavior of layered spheres at sliding inception analyzed with the finite element method and yielding behavior of hafnium diboride coating with consideration of adhesion and shear strength at the interface.

The first part of the study is focused on adhesion behavior of solid thin films. It is well known that adhesion plays a critical role at solid interfaces, usually resulting in local asperities within an interface adhering to each other with the possibility of the interface interlocking. This concept goes back to Tabor (Bowden et al., 1973) whose work showed that a clean steel or brass rod pressed on a soft material such as indium can cause the two metals to adhere. Even though we understand the fundamental laws of adhesion, the physical behavior of two contact surfaces associated with relative motion of the two bodies is not well understood. For this reason, the adhesion behavior between two contacting surfaces was investigated. In order to study this phenomenon, a novel instrument was developed to measure the dynamic interfacial forces. Using this instrument, the pull-off force of two contacting bodies with various combinations of shapes and materials under different horizontal speeds (giving different shearing conditions) was measured and analyzed.

The second part of the study in this work deals with the analysis of magnetic

mode oxide thin film materials. Evaluation of mechanical and tribological properties of thin film material is of great importance for the design and development of engineering components with structural and wear performance. It has been reported by Hess et al. (Hess et al., 2001) that quasi-one-dimensional spin ladder materials exhibit larger thermal conductivity due to the magnetic excitations of the one-dimensional spin ladders. The measured thermal conductivity of bulk LCCO is reported to be around 100 W/Km at room temperature along the direction parallel to the chains. However, to be used for nanothermal conduction, LCCO material should be deposited in the form of thin films on relevant substrate materials. Successful pulsed laser deposition assisted growth of polycrystalline and epitaxial-like LCCO thin films on various substrates was recently reported (Pervolaraki, 2009) and the anisotropic thermal conductivity of LCCO thin films was measured using the dynamic 3ω technique (Athanasopoulous et al., 2010). To characterize the material properties such as hardness, Young's modulus, friction and wear behavior of thin films, nanoindentation and nanoscratch techniques were performed.

The third part of this work is on rough surface contact behavior of various thin film materials measured with a nanoindentation instrument by pressing a flat tip into the rough surface and using a separate dynamic stiffness tester. Since Greenwood-Williamson has developed a contact model of rough surfaces (Greenwood et al., 1966), many researchers extended this model to include plasticity and the effect of asperity interactions. However, there is very limited experimental data correlating with existing models due to the complexity in experimentation, especially at small (sub-mm) scales.

Therefore, a flat punch with a microscale nominal area was made to investigate the contact behaviors of layered specimens. The experiments were performed using an instrumented nanoindenter integrated with the flat tip. The contact stiffness of the rough surface contact was obtained from load-unload displacement curves. An alternative method of measuring contact stiffness, a dynamic stiffness tester based on the resonant frequency method was also used. The obtained contact stiffness results, representing the contact stiffness of the corresponding rough surface, were compared with existing rough surface contact models.

The fourth part of this work is on the wear modeling of sliding contact between two nano-scale asperities. This work is motivated by the need to predict wear behavior of the pole tip in hard disk drives against contact with a thermal asperity. A finite element model of two asperities considering the effect of a single layer on a substrate is developed to calculate the deformed area of asperity and yielded area of the substrate. A relation between the dimensionless potential wear, material properties, and dimensionless normal load was obtained.

The last part of this work is on the yielding behavior of hafnium diboride hard coating films. Hard coatings have been used for the protection of substrate material and play an important role controlling friction and wear. The performance of the coating system does not only rely on the behavior of the hard coating material itself but also on the process occurring at the interface and substrate. The behavior of coating systems can be completely understood only if information about the coating properties, adhesion

strength and substrate properties are available. To this end, analysis of hafnium diboride coatings fabricated at various deposition conditions were performed including the measurement of hardness, modulus and roughness. Then the adhesion strength at the interface was measured by using a nanoscratch technique. Further analysis was performed using the finite element analysis, providing the understanding of yielding mechanism of hard hafnium diboride coating.

1.2. Outline of Thesis

Figure 1.1 shows the outline of the research work presented in this dissertation. The nanoindentation technique was used to measure the hardness and modulus affecting the tribological performance of thin solid films throughout the research. The nanoscratch testing method is also used as a basic tool to measure friction coefficient and wear resistance of thin solid films. Based on the measurement results obtained from nanoindentation and nanoscratch tests, in-depth studies on the tribological behavior of thin solid were conducted.

In chapter 2, titled reversible solid adhesion, the adhesion of thin layered films contacting with a solid were measured. Various controlled thin films including a sample fabricated using MEMS technology were prepared, and pull-in and pull-off forces were measured under various shearing conditions. The measured values were investigated with respect to the material properties as well as the shearing conditions.

Chapter 3 is titled nanomechanical and nanotribological characterization of magnetic-mode oxide thin films for thermal management. A full characterization of a

novel material, LCCO, including its nanotribological behavior as well as measurement of material properties deposited on silicon substrate was conducted. Initial characterizations were performed using an AFM, and a surface profiler to investigate the change of morphology and roughness with respect to the change of deposition condition and nanoindentation at room temperature and at elevated temperature. Nanoscratch experiments for various normal loads, sliding velocity and number of passes were performed.

Chapter 4 is titled effect of roughness on the contact of microscale thin-films: experimental study and comparision with existing models. The contact stiffnesses of various layered surfaces were measured using nanoindentation integrated with a flat tip and an improved dynamic stiffness tester. The measurements results were compared with existing contact models and limitations of the existing models were discussed.

Chapter 5 is titled wear modeling and analysis of head overcoat on protruded pole tip due to contact with thermal asperities. The sliding contact behavior of two asperities describing the pole tip coated with carbon overcoat and the asperity on disk was investigated. Contact analyses were done for various sliding interception conditions using FEA. Wear behavior of the pole tip was predicted by obtaining yielded and deformed areas from FEA results and summarized with an Archard-type wear model.

Chapter 6 is titled synthesis and tribological behavior of hafnium diboride coatings. Thin films of hafnium diboride are deposited by chemical vapor deposition under various deposition conditions. Mechanical properties such as hardness and roughness were

measured. The nanoindentation technique was employed to quantify the adhesion and shear strength at the interface. Finite element analysis was performed to construct the yield zone map with pressure contour.

Lastly, all research findings are summarized in chapter 7.

In addition, in the Appendix, derived formulas for calculating contact stiffness from existing analytical models are given.

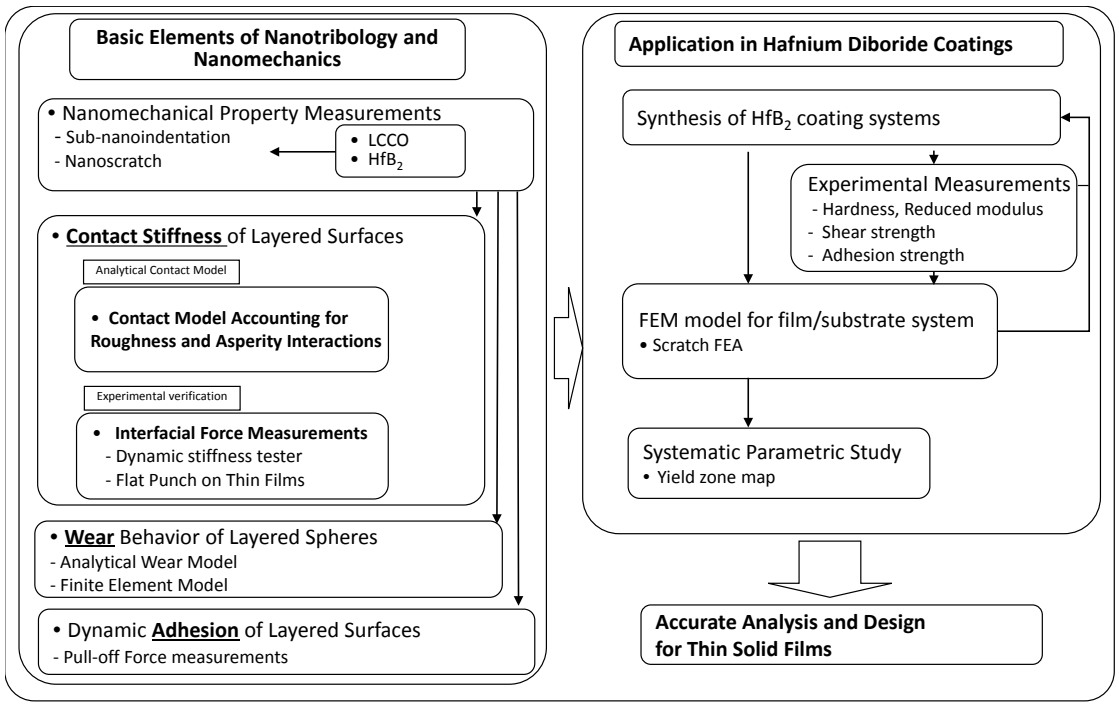

Figure 1.1 Outline of research works presented on the dissertation.

2. Reversible Solid Adhesion

2.1. Introduction

In micro applications such as magnetic storage hard disk drives and MEMS, capillary adhesion and solid surface adhesion are very important and have been studied extensively in recent years. Such micro applications involve (a) large surface-to-volume ratios, (b) low loads, (c) surface roughness that are two-to-three orders of magnitude lower (in the nanometer range) compared to conventional applications and (d) cleaner (less contaminated) surfaces. In these applications, research has focused on understanding and controlling such adhesive interaction via geometrical changes (contacting surface area and surface roughness) or via chemical modification to the surfaces (e.g., using molecularly thin lubricants) (Shi et al., 2005; Tayebi et al., 2005; Suh et al., 2003, Lee et al., 2004; Yu et al., 2005; Xue et al., 2007).

As one of the important adhesion mechanisms, mechanical interlocking also contributes to the adhesive bond. Contact mechanics and tribology communities have known for at least half a century that adhesion plays a critical role at solid (metallic and other) interfaces, usually resulting in local asperities within an interface adhering to each other with the possibility of the interface ‘interlocking.’ The beginning of this concept goes back to Tabor (Bowden et al., 1973), which showed that a clean steel or brass rod pressed on a soft material such as indium can cause the two metals to adhere (bond) as illustrated in Figure 2.1. Also, experiments in ultra-high vacuum between metals (where no oxides are present) result in very high friction due to strong adhesion between bare

metals. In surface contacts and tribological applications friction is low because of the presence of oxides and contaminants on the surfaces (such as lubricants). Reducing interfacial oxides and contaminants on the surfaces (such as lubricants), increase interfacial adhesion. In classical (macro) applications, adhesive friction and adhesive wear are considered precursors to catastrophic failures as they result in high friction and material removal because of the two surfaces adhering to each other. Traditionally, these problems are typically avoided with the presence of lubricants, protective surface coatings and the selection of appropriate materials. Such intrinsic aspect of adhesion between two solid interfaces can be adversely utilized for many applications where sufficiently strong bonding (via adhesion) as well as easy debonding (via reversible adhesion) is required.

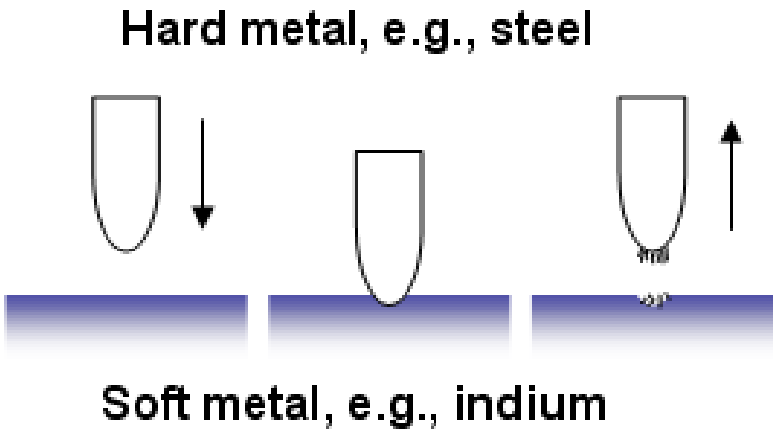

Figure 2.1 Schematic showing principle of solid adhesion.

The objective of this work is to investigate how to make two surfaces bond firmly and then debond easily using two solids. The basic idea of inducing a strong bond between two surfaces is by applying external force to induce interlocking of surface asperities. Debonding can be achieved by applying shear force perpendicular to the interface of two contacting surfaces, which results in breaking the junctions between asperities. To verify the above mentioned bonding and debonding mechanisms, the atomic force microscope (AFM) can be used as a common technique measuring surface forces (Hugel et al., 2001; Cumpson et al., 2003). However, this method is limited to measuring small forces up to 100 μN because of the stiffness of the cantilever (made out of silicon). Thus, it is not suitable for investigating the contact behavior of large sized surfaces ranging from several hundreds of microns to several mm^2. Furthermore, complex and non-linear bending behavior of cantilever makes it hard to ensure "perfect" contact of two surfaces. Therefore, an instrument was developed for measuring the surface forces up to 20 mN with two piezoelectric actuators moving in vertical and horizontal directions, respectively.

In this work, it is investigated how strong of an adhesive force is generated from various controlled solid surfaces and how much pull-off force is required when shearing motion is applied to two contacting surfaces using the developed instrument.

2.2. Experimental Setup for Interfacial Force Measurements

Adhesion and friction forces for micro and nanoscale contact systems are typically measured using cantilever type instruments along with optical tools (AFM), as

well as surface force apparatus (SFA) (Benz et al., 2006). However, dependent upon the material and contact conditions, cantilever type instruments and the compliant SFA are difficult to calibrate.

For these reasons, a novel instrument has been developed by Yeo et al. (Yeo el al., 2008) to measure the forces directly from a custom-build force transducer in line with approaching and contacting surfaces. The experimental setup that was used to capture the adhesion data can be seen in Figure 2.2. The experimental setup has two closed-loop piezoelectric actuators moving in vertical and horizontal directions. The vertical and horizontal movements of two stages can be independently controlled by a Labview program. The program supplies an input voltage between 0 to 4 volts. The piezo stages that were used in this experiment are P-845.60 and P-780 nanopositioning stages made by Physik Instrumente with a maximum travel range of 90 and 80 μm, respectively with controlled movements of less than 5nm. The capacitance type transducer is attached to the vertical stage and one of the samples is directly attached to the end of the transducer to measure the adhesion and pull-off forces from the interaction of two samples. The Labview program monitors the vertical displacement of the piezo stages (P-845.60) and can determine the degree of force applied to the sample by controlling the displacement of the stage.

The uniqueness of this instrument is that in addition to nanometer positioning accuracy, it also uses a high resolution capacitance-type force transducer developed by Yu and Bonin (Yu et al., 2005). Three different transducers were used in the test to cover

the different range of contact force. Detailed specifications of the transducers used in the experiment are listed in Table 2.1. Alignment of two surfaces is ensured using a tilting stage (with 3 degrees-of-freedom) and a microscope.

Table 2.1 Specification of force transducer.

Force Constant	**Displacement Constant**	**Spring Constant**	**Moving Mass**
0.22 V/gram	0.48 V/um	21312 N/m	58 mg
2.28 V/gram	0.61 V/um	2634 N/m	24.3 mg
5.66 V/gram	3.31 V/um	5740 N/m	33.3 mg

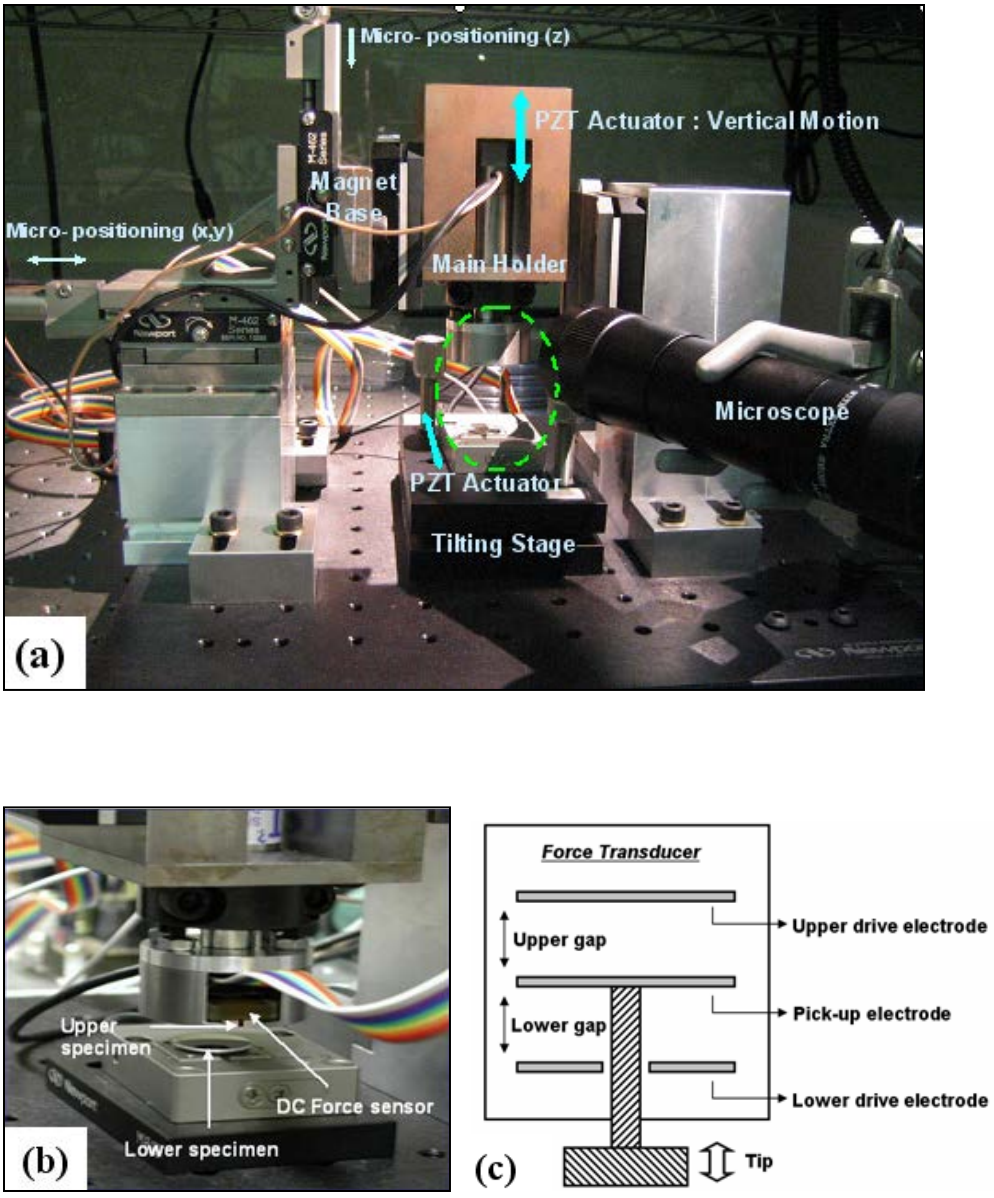

Figure 2.2 Dynamic adhesion tester: (a) overall view, (b) close up of the interface, and (c) dynamic capacitive force transducer.

2.3. Test Conditions

In this research, the bonding and debonding behaviors for various interface contact conditions were investigated. The schematic of Figure 2.3 depicts such measurement conditions under vertical movement of the upper piezoelectric stage and horizontal movement of the bottom stage.

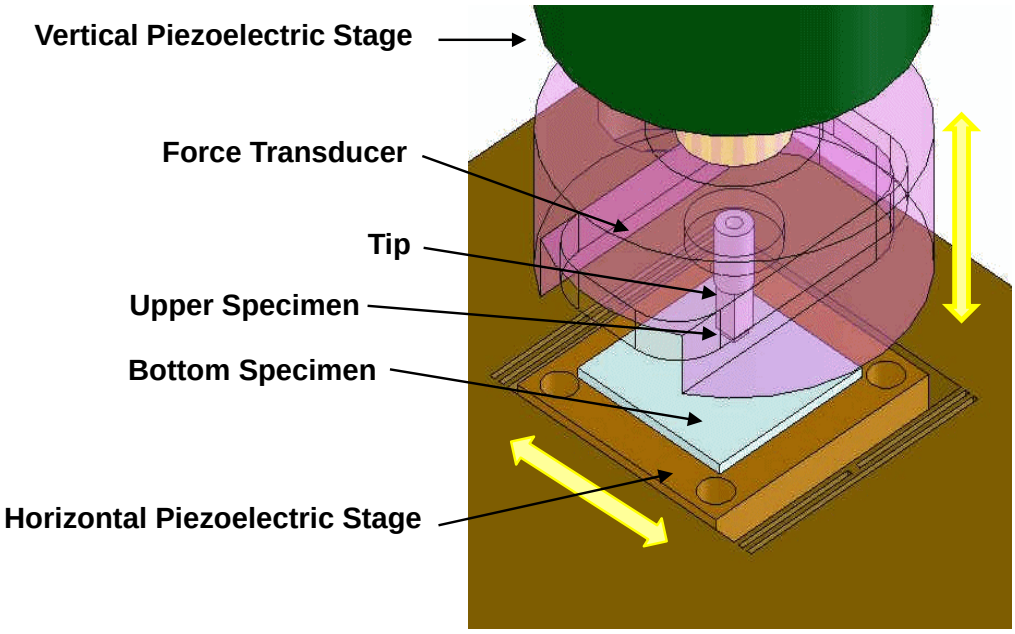

Figure 2.3 Schematics showing horizontal and vertical motions of stages.

Figure 2.4 shows the displacement profile of the piezoelectric stage where the upper sample provides a vertical movement and the bottom surface moves horizontally. The sample on the bottom surface sits on the bottom piezoelectric stage which provides horizontal movements. The upper sample is attached to the transducer through the tip, with which the force data measured for the two surfaces in relative motion is obtained. The upper sample and transducer are again connected to the piezoelectric stage which

moves vertically.

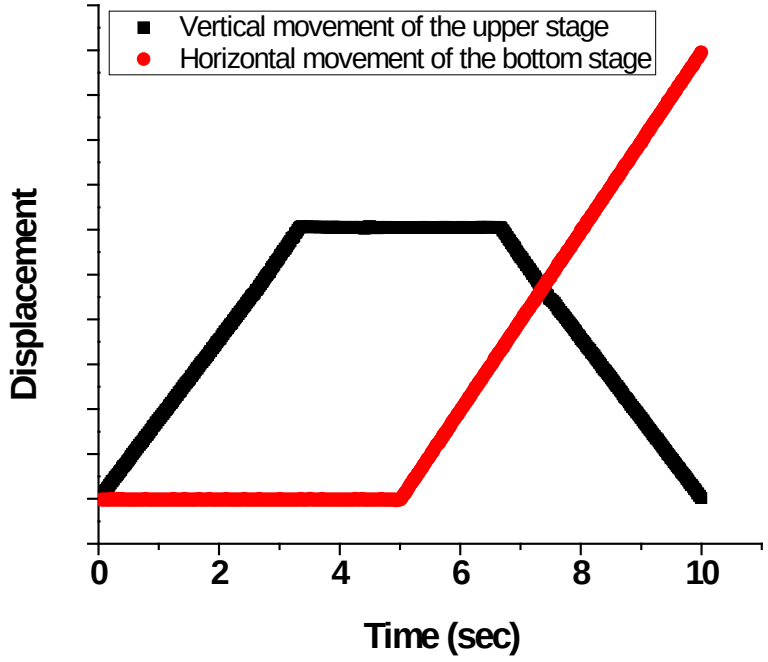

Figure 2.4 Displacement profiles of the piezoelectric stages.

The black solid line depicts the motion of the upper stage. The upper sample moves toward the static bottom sample making contact with the bottom sample, where the bottom surface provides horizontal motion, moves 5 seconds later. For the first five seconds, the upper sample makes the approach to the bottom surface where in the following five seconds, the two surfaces remain in contact. In the next five seconds, the upper sample retracts from the bottom sample. The horizontal stage whose motion is shown with the red solid line continues to be static for the first 5 seconds maintaining the interfacial contact and then starts to move with a velocity from 0 μm/s to 5 μm/s. Max.

contact force is determined with Max. displacement of the upper stage, and the horizontal velocity is varied with different samples. The horizontal stage remains fixed when it is set to have zero velocity while the upper sample makes contact with bottom surface. When the horizontal stage moves with a certain velocity other than zero, it applies a shearing force to the two contacting surfaces. Applied shearing force plays a role in breaking the junction between asperities formed in the two surfaces and liquid column created by meniscus force.

2.4. Preliminary Test Results and Discussion

When two surfaces are brought into contact, they may snap-to-contact when they are at a certain distance apart due to the presence of attractive intermolecular (adhesive) forces such as van der Waals forces. This force is known as pull-in force. Once the surfaces are in adhesive (interlocking) contact, any applied surface displacement gives rise to contact and adhesive forces. When the two surfaces are pulled apart in normal directions in the absence of vibrations, a certain magnitude of force is needed to separate the contacting surfaces, which is called pull-off force. This force is the strength of the bond between two surfaces. The pull-in and pull-off force can be affected by the following parameters.

A. Physical/Geometrical property

- Surface roughness
- Surface energy
- Hardness and elastic modulus

- Nominal contact area

B. Interface conditions

- Dry contact
- Humidity involved
- Lubrication

C. Contact system dynamics

- Shearing velocity

Adhesive forces between two surfaces are affected by several different modes of adhesion (Israelachivili, 1985; Kendall, 1994; London 1936), namely, mechanical interlocking, electrostatic forces, adsorption and diffusion. It is postulated that when two surfaces do not contact each other, electrostatic forces which arise from the two different materials with different electrostatic charges contribute to generating adhesive forces. When two adhesive surfaces interlock with the surface irregularities, however, the interlocking mechanism may contribute significantly to the overall adhesion. In reality, it is hard to distinguish these different modes of adhesion. Thus, it is verified experimentally with different samples how much adhesion forces can be generated.

Using the instrument, the adhesive force between <100> silicon surfaces (nominal contact area of 1×1 mm^2) was measured. The silicon was in static condition on the bottom piezoelectric actuator while the top silicon surface attached on the upper piezoelectric actuator was approaching. Figure 2.5 depicts a representative force-

displacement curve measured using the adhesion tester under 40% humidity at room temperature. As seen in Figure 2.5, there are different regions showing different approaching and retracing behaviors. When the top surface is far away from the surface, there are no interactions between the two surfaces. As the top surface approaches closer to the bottom surface, a jump-to-contact event is observed due to attractive van der Waals forces. After the jump-in event, the movement of the top surface is coupled with the bottom surface, so the displacement of the top surface appears in the curve as a straight line. After the upper stage stops advancing and begins to retract, with a certain amount of hysteresis, the upper surface pulls away from the bottom surface. Once after the upper sample is detached from the bottom surface, the upper sample remains in its undisturbed position with zero contact force. The maximum force required to separate the two contacting surfaces is defined as a pull-off force in the following experiments.

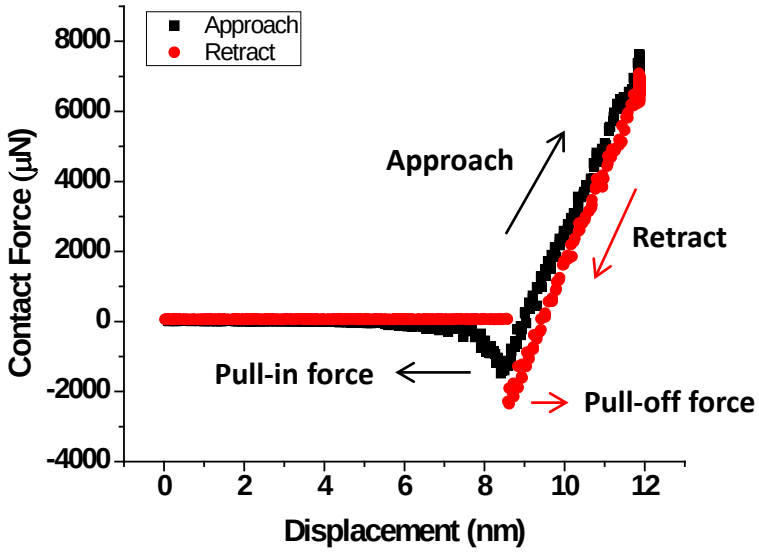

Figure 2.5 Representative force-displacement curve between 1x1 mm^2 silicon surfaces under stationary horizontal conditions.

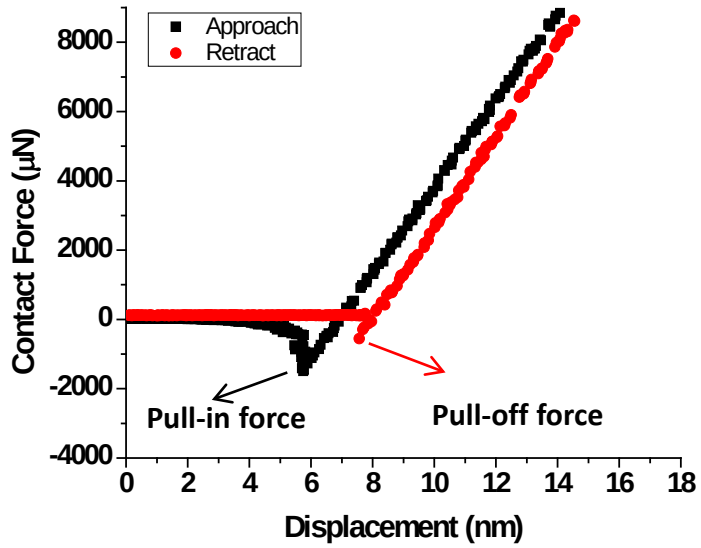

Figure 2.6 Representative force-displacement curve between 1x1 mm^2 silicon surfaces when the bottom surface moves in horizontal direction during retraction.

Figure 2.6 shows a representative force-displacement curve between two surfaces made out of silicon when the bottom surface moves in horizontal direction with a velocity of 5 μm/s. Approaching behavior of the top surface is the same as the result shown earlier in Figure 2.5. It can be seen that the retracting behavior of the top surface is different when the bottom surface moves horizontally. Compared with the result obtained from static condition, pull-off force is reduced significantly compared to the force obtained from static condition (no horizontal movement). This is mainly due to molecules (high humidity) formed between the two contacting surfaces, and the adhesive force is mainly determined by the meniscus (water bridges between surface asperities). According to Hu et al. (Hu et al., 1995), no water adsorption occurs below 20% humidity. Then, as the humidity level increases, the water grows. Above 45% humidity level, the whole surface will be covered with a water layer. In the case of experimental results done by Yeo under 60% humidity (Yeo, 2008), the measured pull-off force values were increased by shear force. He suspected that the increased pull-off force values are caused by the agglomerated water molecules during shearing motion. Considering that the experiment was done under 40% humidity condition, we assume that the silicon surface is not fully covered by a water layer. In such a case, the liquid bridges can be broken by controlling the surface dynamics, e.g. by applying a shear force in the horizontal direction, and the pull-off force (bond strength) will be very small, thus achieving reversible adhesion and debonding. This is shown schematically in Figure 2.7.

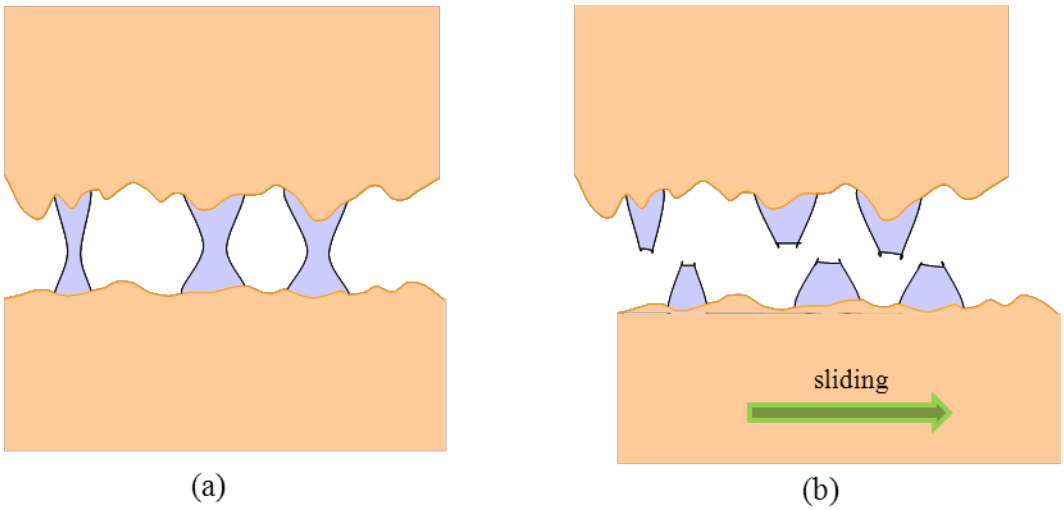

Figure 2.7 Schematics showing (a) the formation of liquid meniscus bridges (high bond strength), (b) breaking of the meniscus bridges (debonding) using tangential surface dynamics.

Under dry contact conditions, the effects of water molecules are negligible and the contacts between asperities become dominant. Depending on the contact conditions such as external forces applied, surface roughness, and stiffness of the surface, the degree of material cohesion and attractive force can change. When the shearing force is applied to asperity junctions, these junctions will be broken and thus the two surfaces can be detached with less force. Schematics showing the formation of asperity junctions in dry contact and breaking of asperity junction due to the relative motions of the two surfaces are shown in Figure 2.8.

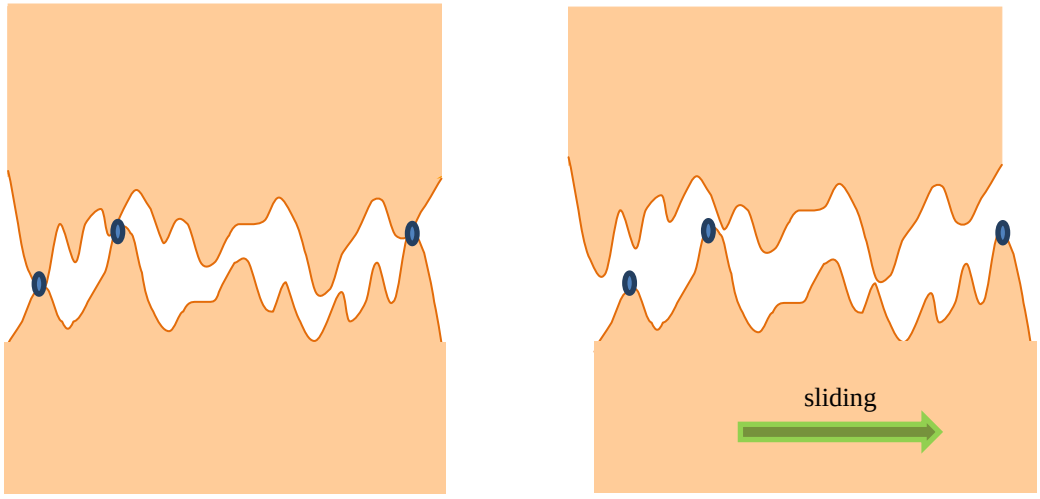

Figure 2.8 Schematics showing (a) the formation of asperity junctions in dry contact, (b) breaking of asperity junction due to the relative motions of the two surfaces.

2.5. Test Samples

Several different samples were prepared in this test in order to compare different pull-off forces. Silicon wafer which has a very smooth surface was mainly used. The reason is that silicon wafer has sub-nanometer roughness, which allows it to have high interfacial adhesion. Moreover, a steel ball, gold coated on silicon and pressure sensitive adhesive (PSA) and a sample coated with 8 μm thick photoresist (PR) were also utilized in the experiment.

The PSA sample used for storing small samples like AFM tips was utilized. Among a variety of polymers used to manufacture PSA, for example, acrylic, copolymers, butyl rubber-based systems, silicones, urethanes, vinyl esters, and the like, silicone based rubber-like PSA which has a thickness of 330 μm was used in the experiment.

PR (AZ4620, Clariant) coated specimen was prepared using a spin coating process to have regular 8.3 μm film thickness. And then it was baked at 60℃ for 1 minute and cured for 2 hours at room temperature.

Au sputtered specimen was prepared using conventional microfabrication techniques as shown in Figure 2.10 (c). A schematic of the processing sequence for the fabrication of the 200×200 μm^2 Au sputtered specimen is shown in Figure 2.9. The fabrication started with double-sided photolithography. A double-sided polished 4 inch wafer (Silicon Quest, 500 μm thick, n-doped, (100) oriented) was pre-baked at 110 ºC for 2 minutes to dry the residual moisture and to improve the adhesion of PR. An adhesion promoter, AP8000 (Dow Chemical), was spun on the wafer for 30 sec at 3000 rpm to increase the adhesion of the PR to the substrate. PR4620 (AZ-Electronics) was spun on the wafer for 30 sec at 3000 rpm to result in a 8.3 μm thick film, and was subsequently soft-baked for 2 min at 60 ºC and 2 min at 110 ºC on the hotplates to remove the solvents and enhance the adhesion between the PR film and substrate. The same PR spin-coating and soft-baking procedure was repeated for the backside of the wafer. Using a Cr mask (front side pattern) made on the soda-lime glass plate, the latent image of the desired pattern was created on the PR film by exposing it under UV radiation at 405 nm with a dose of 125 mJ/cm^2. The exposure was done in the EV420 contact aligner. The developer solution was prepared using a mixture of 100 mL of DI wafer and 25 mL of 400 K developer (Clariant). Only the alignment marks on both edges of the wafer was developed without immersing the wafer in the developer solution. The actual patterns of

the front side were not developed at this time to prevent them from being developed twice. Another exposure with the same dose was done on the backside of the wafer using a Cr mask (back side pattern) and with the back-to-front alignment – aligning the alignment mark pattern in the backside Cr mask with the alignment mark in the PR layer that was developed in the previous step. The wafer (exposed on both front and back sides) was fully immersed into the developer solution for 2 minutes or more until all the patterns were clearly developed on both sides. After the residual developer was sufficiently washed out by DI quench and repeated rinse, the wafer was baked at 110 ºC for 2 minutes to dry out the moisture. The developed patterns were thoroughly inspected using an optical microscope.

The front side of the wafer was then etched in an ICP etcher (Plasma-Therm SLR770) using a time-multiplexed Bosch process with SF_6 for etching and C_4F_8 for sidewall passivation. The patterned PR served as an etch mask. Five hours etching time was used to create an array of posts with heights of 200 μm. Once the desired depth was reached, the wafer was flipped and etched on the backside of the wafer until the die-delineating lines were completely etched through. Upon the completion of etching, PR on the dies was stripped in 400T PR stripper (Clariant). A 1 μm thick Au layer was deposited on the front side of the wafer using DC magnetron sputtering (~10^{-2} Torr of Ar background pressure) prior to the backside etching in ICP-DRIE.

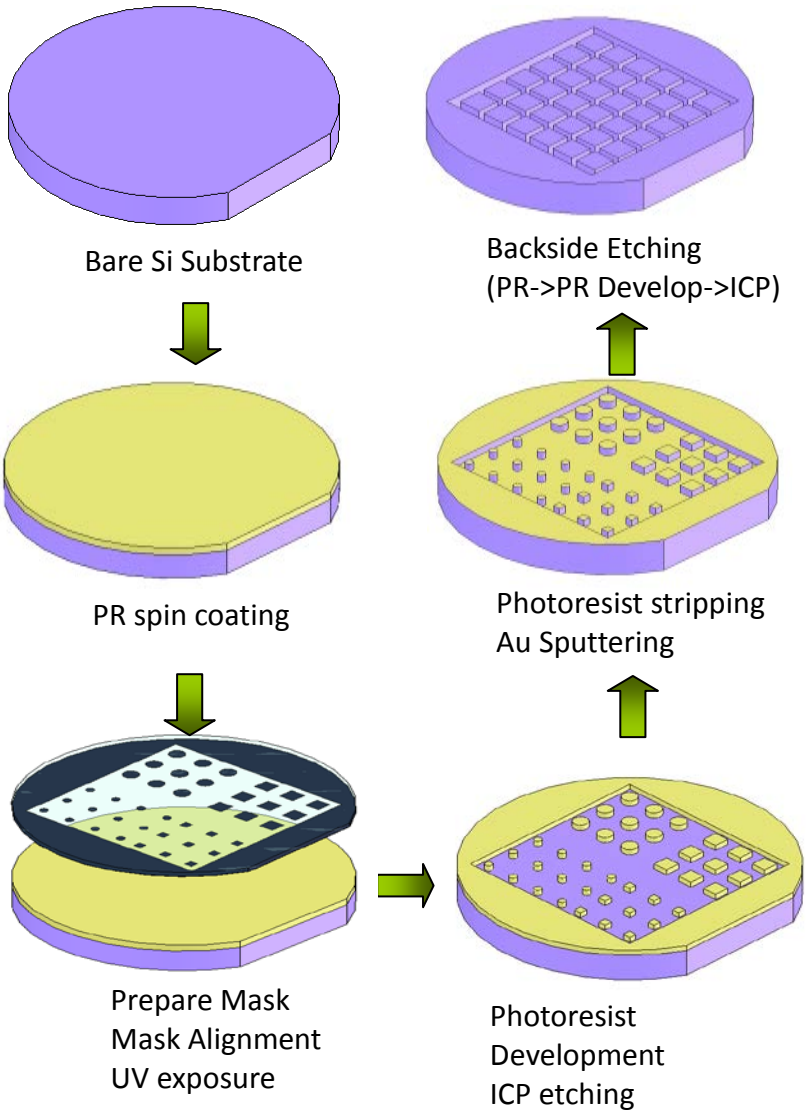

Figure 2.9 Schematics of the processing sequence for the fabrication of 200×200 μm^2 Au sputtered sample.

All samples were rinsed in acetone before being finally rinsed in isopropyl alcohol, and then air dried. The roughnesses of the specimen used in the experiment are shown in Table 2.2 and the surface measurement results, which were measured with a

Dimension 3100 atomic force microscope for the samples used in the test, are shown in Figure 2.10.

Table 2.2 List of test samples.

Sample name	**RMS roughness (5x5 μm^2)**
Ball Sample	
Steel ball (ϕ1.6 mm)	5.25 nm
Plane Surface	
<100> Silicon wafer	0.11 nm
1 μm thick Au sputtered on silicon (200×200 μm^2)	3.84 nm
1 μm thick Au sputtered on silicon (1×1 mm^2)	3.84 nm
8 μm thick photoresist coated on silicon	-
Pressure sensitive adhesive	-

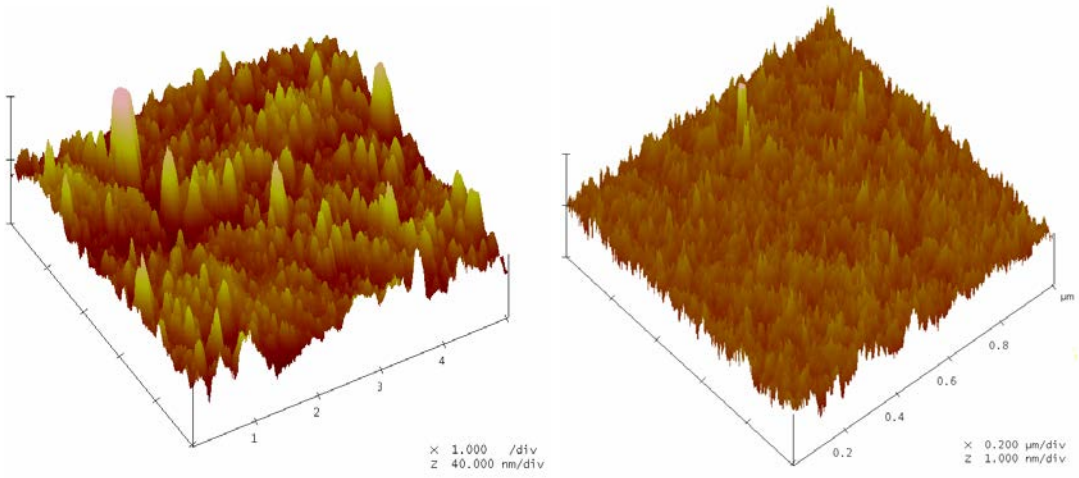

(a) (b)

Figure 2.10 (cont. on next page)

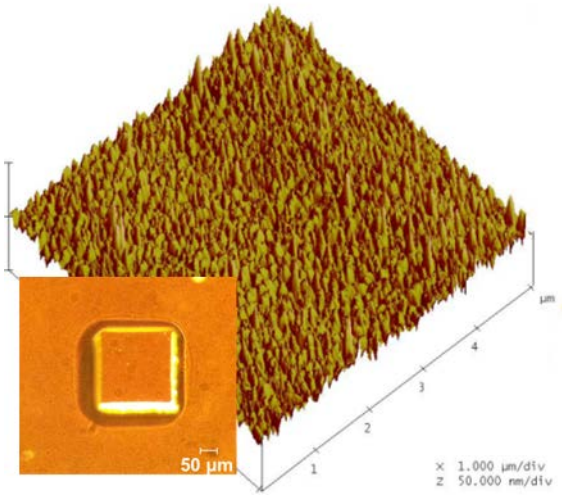

(c)

Figure 2.10 AFM images of test samples, (a) steel ball, (b) silicon (100), and (c) 1 µm thick Au sputtered on silicon wafer. The inset in (c) shows the optical image of 200×200 μm^2 Au sputtered sample.

2.6. Test Results and Discussion

2.6.1 Horizontal Dynamics for 1 mm^2 Silicon Wafer to Silicon Wafer

Using two bare silicon wafers, the dynamic adhesive force was measured. The samples used in this test had a nominal contact area of 1 mm^2. The behavior of dynamic adhesion is shown in Figure 2.11. The contact pressure calculated with nominal contact area was 3 kPa for a silicon wafer surface which has an area of 1×1 mm^2 at 3000 µN contact force.

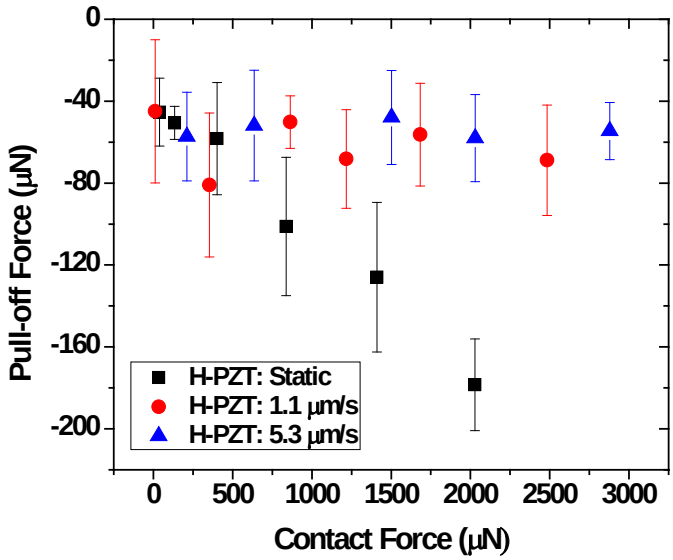

Figure 2.11 Pull-off force vs. contact force for the contact between 1mm^2 silicon wafer with 0, 1.1 and 5.3 μm/s horizontal stage velocity

The horizontal piezoelectric stage begins its movement during midway of the contact process. The maximum displacement of the vertical piezoelectric stage varies the contact force. The pull-off force during horizontal movement of the bottom plate was obtained. The pull-off force increases when the bottom sample is stationary and contact force increases. For example, when the contact force of 2000 μN applied with zero velocity of the bottom stage resulted in a pull-off force of 180 μN whereas the pull-off force was measured at 55 μN when the horizontal stage was moving with a velocity of 5.3 μm/s. In this study, the pull-off force was almost independent of the horizontal stage's velocity. This implies that the adhesion force rapidly decreases with the aid of shearing force even though the normal contact force is being applied.

2.6.2 Horizontal Dynamics between Steel Ball and Pressure Sensitive Adhesive

PSA is characterized as being normally tacky and exhibiting instant tack when applied to a substrate. Figure 2.12 depicts the pull-off forces when the steel ball and pressure sensitive adhesive (PSA) come into contact. Once the bottom sample showed dynamic motion in horizontal direction, the pull-off force decreased.

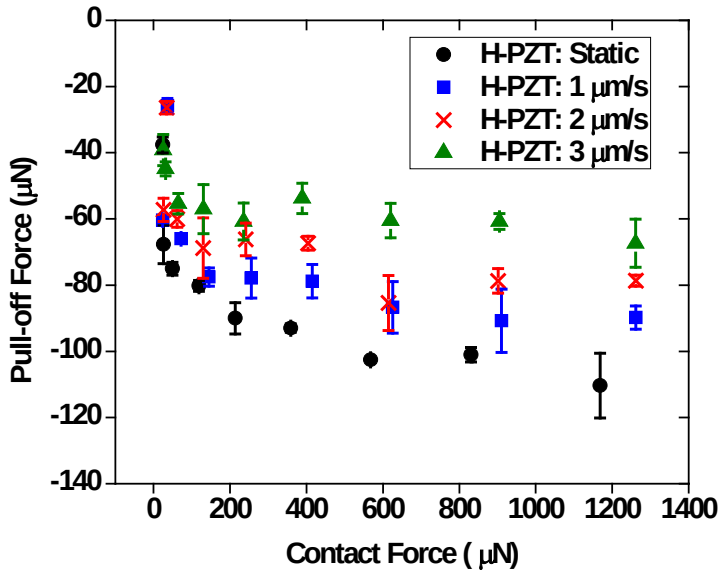

Figure 2.12 Pull-off force vs. contact force for the contact between steel ball of 1.6 mm in diameter and pressure sensitive adhesive at 0, 1, 2 and 3 μm/s horizontal stage velocity.

A faster horizontal motion gave lower pull-off forces. It was also found that PSA reduced the standard deviation of the measurements compared to solid surface contact, such as silicon wafer (indicating better repeatability). This also implies that the soft and sticky surface of PSA creates a stable and predictable interfacial contact. Two contacting

surfaces stably contact each other due to the soft characteristic of PSA surface because flow of the “flexible” PSA material cover the asperity of the harder steel ball. Such characteristic of soft surface can result in obtaining stable interfacial contacting but, it is not good enough to increase the contact pressure. Moreover, the intrinsic sticky characteristic brings a limit for decreasing the pull-off force drastically at a given range of horizontal stage’s velocity. To be applied to an application that demands several MPa contact pressure, PSA is required to change the thickness and hardness.

2.6.3 Horizontal Dynamics between Steel Ball and Photoresist Coated on Silicon Wafer

Figure 2.13 describes the experiment result on PR coated on silicon wafer substrate making a contact with steel ball of 1.6 mm in diameter. The PR (AZ4620) used was made by Clariant. PR coated surface was prepared using the spin coating process to obtain a nominal 8 μm film thickness. Subsequently, it was baked at 60 ℃ for 1 minute and cured for 2 hours at room temperature. By not using a fully baked PR, the “sticky” property of the PR resin was utilized.

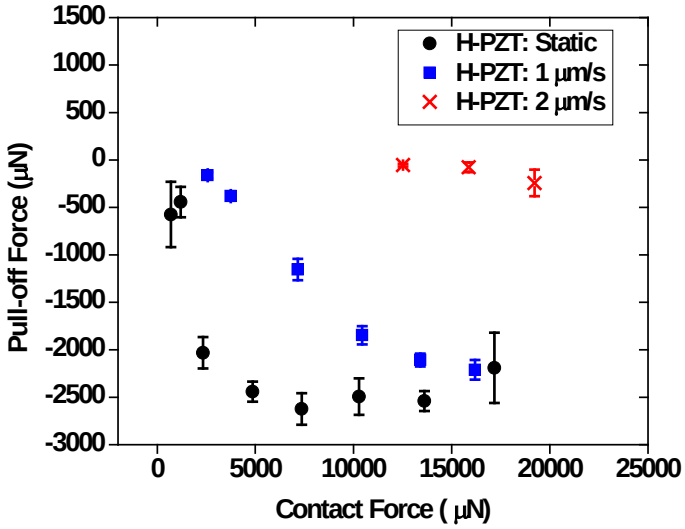

Figure 2.13 Pull-off force vs. contact force for the contact between steel ball of 1.6 mm in diameter and photoresist coated on silicon wafer surface at 0, 1, and 2 μm/s horizontal stage velocity.

PR, which tends to be sticky on hard surfaces, requires a higher range of contact pressure than thick and soft PSA. When a steel ball of 1.6 mm in diameter makes contact with the silicon wafer coated with PR under the contact force of 13000 μN, the contact pressure is assumed to be in the range of 28.74 to 54.37 MPa. This calculation result is obtained from FEM analysis using ABAQUS. Note that the elastic modulus of hard baked PR (2 minute at 60 ℃) is 4 GPa. Thus, the soft baked PR (1 minute at 60 ℃) is assumed to have the elastic modulus ranging from 1 to 4 GPa.

The pull-off force decreased as the velocity of the horizontal stage increased, which is similar to the previous results besides the fact that pull-off force values are saturated after a certain amount of contact force (7500 μN) when the bottom sample is

stationery as seen in Figure 2.13. This is caused by the fact that the PR layer is penetrated with the contact force over 7500 μN. Once after the PR layer is penetrated, the steel ball starts to make a contact with hard substrate (Si) and pull-off force will not be dominated by the sticky characteristic of PR layer.

When the contact force of 13,000 μN was applied to PR with no horizontal movement, it was found that the measured pull-off force was 2500 μN whereas when the horizontal stage was moving with a velocity of 2 μm/s, the measured pull-off force was only 15 μN, which is more than two orders of magnitude reduction. The exact ratio of two pull-off forces measured under static condition and at a velocity of 2 μm/s is as much as 167 times. This clearly means that when a hard surface is coated with a polymer, higher adhesion force can be achieved due to the fact that flexible PR can readily deform to adhere to opposing surface. On the other hand, opposing surface can be easily detached with low shearing force to break the soft junction formed by the soft PR. However, the PR used in this experiment has time-dependent properties and thus, its sticky characteristic becomes significantly weak when it is left more than one day at room temperature.

2.6.4 Horizontal Dynamics for 200×200 μm^2 Au Coated Silicon Wafer and Au Coated Silicon Wafer

Figure 2.14 describes the test results of pull-off force when the silicon surface has sputtered 1 μm thick gold film with 200×200 μm^2 size and makes contact with an identical surface. The controlled area of 200×200 μm sized gold pillar was fabricated

with a standard photolithography process, as described earlier. Bare silicon wafer was coated with PR through a spin coating process and then was exposed to UV light using mask before being fabricated through inductively coupled plasma (ICP) etching process.

Two humidity levels were investigated in this study, 55% and 30% to simulate usual humidity levels of summer and winter, respectively. The contact pressure calculated with nominal contact area ranges from 12.5 kPa to 75 kPa for a silicon wafer surface which has an area of 200×200 μm^2 and a contact force that varies from 500 μN to 3000 μN.

The overall trend of the pull off force with gold coated surface shows a similar behavior as the previous tests. The pull-off force decreased when the horizontal stage moved in the horizontal direction, compared with in static horizontal stage. In this case, the difference of humidity level gave different pull-off force values.

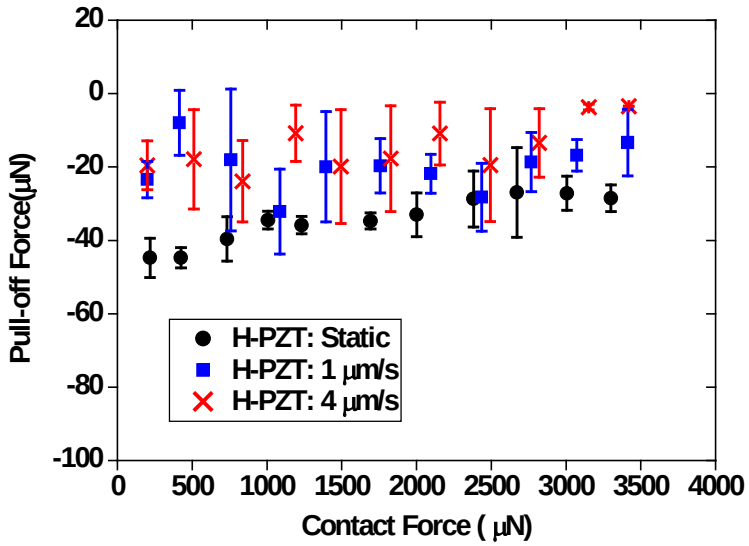

(a)

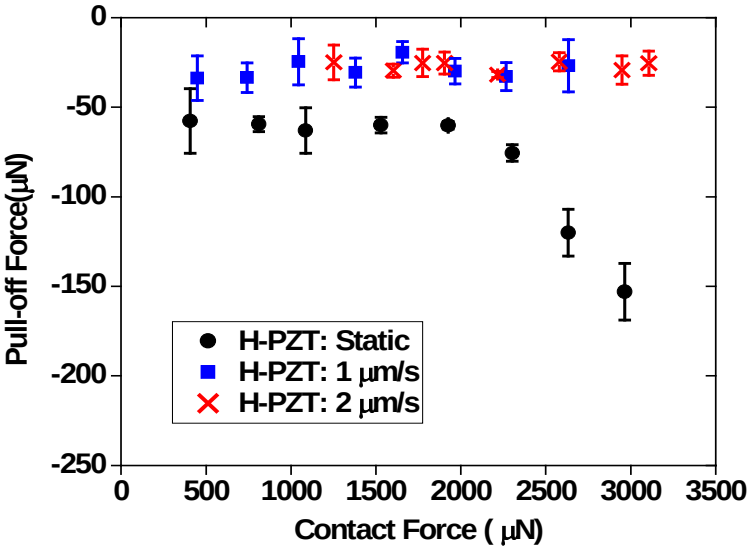

(b)

Figure 2.14 Pull-off force vs. contact force for the contact between 200 × 200 μm^2 Au coated silicon wafer and Au coated silicon wafer; (a) 55% humidity level (b) 30% humidity level.

2.6.5 Horizontal Dynamics for 1×1 mm^2 Au Coated Silicon Wafer and Au Coated Silicon Wafer

Figure 2.15 shows the test results with contacting two surfaces between 1×1 mm^2 sized gold coated silicon sample and gold coated silicon sample. It was found that the gold coated surface had relatively higher adhesion force than bare surface wafer and lower pull-off force when shearing motion was applied. When 3450 μN of contact force was applied to the sample, the difference of pull-off force for the case where there was 0 μm/s horizontal motion and 1 μm/s was 24.2 times.

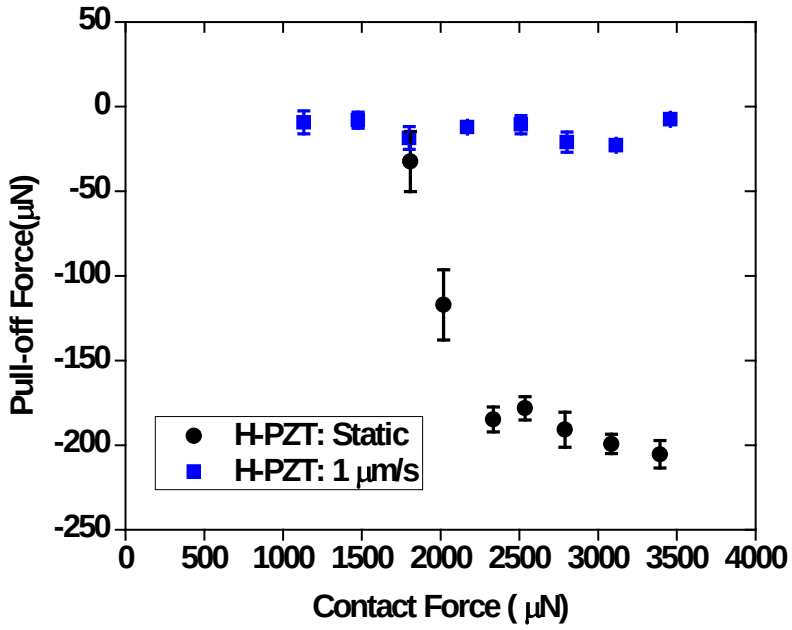

Figure 2.15 Pull-off force vs. contact force for the contact between 1×1 mm^2 Au coated silicon wafer and Au coated silicon wafer.

2.7. Summary

The adhesion behavior between two contacting surfaces was investigated. The experimental adhesion tests were performed under changes of horizontal speed, which gave different shearing conditions with various combinations of contact shapes and materials. As a result of these tests, it has been found that faster horizontal motion gives lower pull-off force. It has been also found that the pull-off force is dependent on the material of the contacting surfaces, surface roughness and applied contact force. According to Bowden and Tabor (Bowden et al., 1973), adhesion comes from the interlocking of the surface asperities. When the applied load is directed perpendicularly to the contacting surfaces, the two surfaces hold together because of adhesion. Such junctions are more easily formed when there is water or another liquid film. When there is moisture absorbed at the interface between the two contacting surfaces, adhesion produced in such an atmosphere drastically increases. However, the adhesion is reduced by shearing of junctions at the points of close contact. These results were compared with the test done with a gold coated pillar sample.

Adhesion also depends on the mechanical properties of the contacting surfaces. This was proven by comparing a bare silicon sample with a gold coated sample. When the gold coated sample was used, an increase in the adhesion force was seen. Furthermore, the pull-off force of the gold coated sample decreased as well. For the gold coated sample with an area of 1 mm^2 under a contact force of 3000 μN, the adhesion force increased up to 24.2 times more than the pull-off force whereas the PR coated sample gave a ratio of

167, which indicates that the adhesion force can be controlled via surface modification.

A unique dynamic adhesion tester was build and demonstrated that can perform dynamic adhesion measurements with sliding motion as well. This study provides proof of concept that using proper material selection and interface surface design (contacting surface area), the adhesion force can be maximized and minimized with the proper aid of shearing force. Based on the experimental validation of solid surface adhesion, it is expected that desired adhesion and pull-off adhesive force can be achieved through proper material selection (thin film and substrate material) and geometrical changes (surface roughness and surface texturing).

3. Nanomechanical and Nanotribological Characterization of Magnetic-mode Oxide Thin Films for Thermal Management

3.1. Introduction

To increase the areal density of hard disk drives, it is important to decrease the gap between head and media. It is suggested that magnetic spacing of less than 7 nm is required to achieve 1 Tb/in^2 or more (Wood, 2000; Gui, 2003). At such small head-media spacing (HMS), intermittent contacts between a slider and a disk are unavoidable and result in data erasure due to interfacial heating and contact stresses (Liu et al., 2005).

There are several works related to the mechanical behavior of head-disk interfaces (HDI). Suzuki et al. measured the flash temperature during impacts between a slider and an artificial asperity made on a disk and showed that the temperature during an impact was about 150 °C (Suzuki et al., 1989). Suk et al. demonstrated experimentally by dropping a small stainless steel ball of 0.8 mm in radius on rotating disks to see if the disk was not plastically damaged by high-speed contacts and showed that flash temperature induced data erasure resulting from frictional heating was the dominant factor for data erasure (Suk et al., 2000). Yu et al. performed finite element analysis (FEA) for flash temperature analysis on oblique impact problems between a slider corner and a rotating disk for different layer/substrate disk combinations and showed that thermal response was affected by the thermal conductivity of surface layers (Yu et al., 2010). For 100 nm thick CrV layer on top of glass substrate, flash temperature reached up to 118 °C while diamond like carbon (DLC) layer which has the same thickness as CrV

on top of glass substrate reached up to 625 °C. Considering the higher thermal conductivity of CrV (69.1 w/mK) than that of DLC (0.52 w/mK), higher temperature was obtained as expected (shown in Figure 3.1). Although DLC has been widely used due to its superior properties like high hardness and very low friction coefficient, Yu's analysis showed that thermal property was also very important in protecting magnetic layer underneath it.

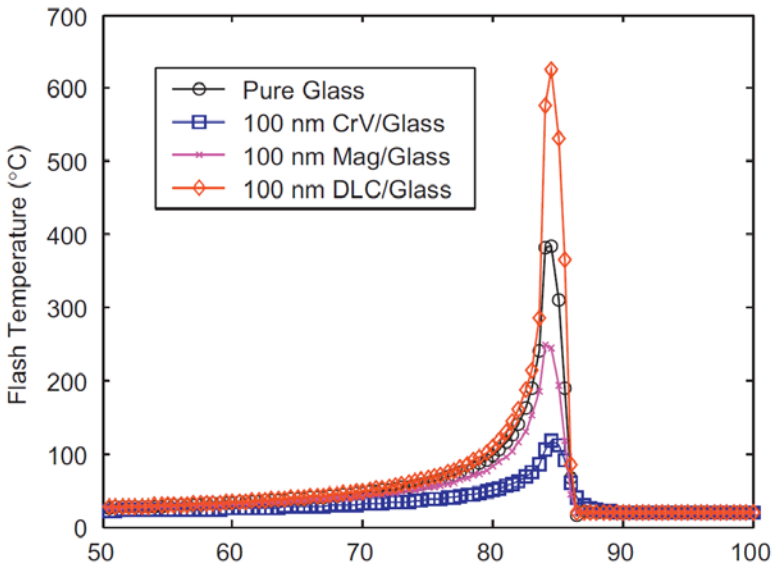

Figure 3.1 Comparison of the flash temperatures in the sliding direction underneath the impacting spherical slider at 6 μs for different materials (Yu et al., 2010).

Therefore, it is clear that thermal conductivity of HDI layers is very crucial in quickly dissipating the heat during impact, thus avoiding data erasures due to flash temperatures. Moreover, for heat assisted magnetic recording (HAMR) achieved by locally heating up the recording media to drop the coercivity of the magnetic material to

allow magnetic recording with a relatively weak magnetic field, it is important to induce localized heating avoiding thermal distortions and internal thermal stresses in HAMR (Black et al., 2007).

It has been reported that quasi one-dimensional spin ladder materials such as $SrCuO_2$, Sr_2CuO_3 and $((Sr,Ca,La)_{14}Cu_{24}O_{41})Sr_{14}Cu_{24}O_{41}$ exhibit larger thermal conductivity due to the magnetic excitations of the one-dimensional spin ladders by Hess et al. (Sologubenko et al., 2001; Hess et al., 2001). One dimensional magnon-mediated thermal conductivity of bulk $La_5Ca_9Cu_{24}O_{41}$ (LCCO) is around 100 W/mK at room temperature along the direction parallel to the chains (Hess et al., 2001). However, to be used for nanothermal conduction, LCCO material should be deposited as a form of thin films on relevant substrate materials. Among many film deposition methods such as chemical vapor deposition (CVD), sputtering, pulsed laser deposition (PLD) and cathodic arc deposition (arc-PVD), electrohydrodynamic deposition, PLD can be used to obtain epitaxial multi-component oxide thin films (Androulakis et al., 2004; Gardelis et al., 2004; Morales et al., 2005). Successful pulsed laser deposition (PLD) assisted growth of polycrystalline and epitaxial-like LCCO thin films on various substrates was recently reported (Pervolaraki et al., 2009; Pervolaraki et al., 2010). The anisotropic thermal conductivity of LCCO thin films was measured using the dynamic 3ω technique (Athanasopoulos et al., 2010).

In this study, we examined the structural, morphological characteristics of thin LCCO films deposited on MgO rock salt, $SrTiO_3$ (STO) perovskite and Si substrates and

measured the nanomechanical properties of it using the nanoindentation and nanoscratch techniques. Our attention was mainly focused on the Si substrate due to its compatibility with the present microchip and the potential use in hard disk drive industry.

3.2. Experimental Details

Thin LCCO films were grown on (0 0 1) MgO, (1 0 0) STO and (1 0 0) Si single crystals using PLD technique. PLD was chosen for the deposition of LCCO films due to the versatility of high oxygen ambient pressure and high success rates in stoichiometric transfer. KrF excimer laser radiation (COMPex Pro 201) was used for the ablation of the stoichiometric pristine LCCO targets. The detailed procedure for preparing pure LCCO pellets is described by Pervolaraki (Pervolaraki, 2009). Pulse repetition rate of 10 Hz, partial pressure of oxygen, PO_2, of 0.2 mbar, substrate temperature of 650 °C and fluence varying from 1.2 to 1.35 J/cm^2 were used for the deposition of the films. The target was continuously rotated at a separation of ~4 cm from the substrate. The substrates were cleaned ultrasonically in the sequence of acetone, methanol, isopropanol and distilled water. The native oxide of the Si substrate was preserved since no further treatment was applied.

The crystallographic structure of the films was initially investigated using an X-Ray diffractometer (XRD), SHIMADZU (XRD 6000). The step height of the films was measured using two different apparatus, non-contact optical profilometer (Ambios Xi-100) and a contact profilometer (Tencor P-15), were used for comparison. To evaluate the morphology and the root-mean-square (RMS) roughness of the films, we employed

non-contact mode AFM (Dimension 3100).

Nanoindenation and nanoscratch tests were performed using a Hysitron TS 75 Triboscope shown in Figure 3.2 to obtain the reduced modulus, hardness and friction coefficient at room temperature. Two different indenters (a cube corner and a Berkovich) which have three-sided pyramidal shape were used to measure the reduced modulus and hardness. A cube corner tip, shown in Figure 3.3 (a) and (b), has a total included angle of 90° and relatively sharper end radius (< 50 nm) than the Berkovich tip, was used to cover shallow indentation depths from 20 to 50 nm and the Bekvovich tip, which has a total included angle of 142.3° with an average radius of curvature of about 150 nm, was used for contact depths greater than 50 nm.

Figure 3.2 Photograph of Triboscope TS 75 used for nanoindentation and nanoscratch experiments.

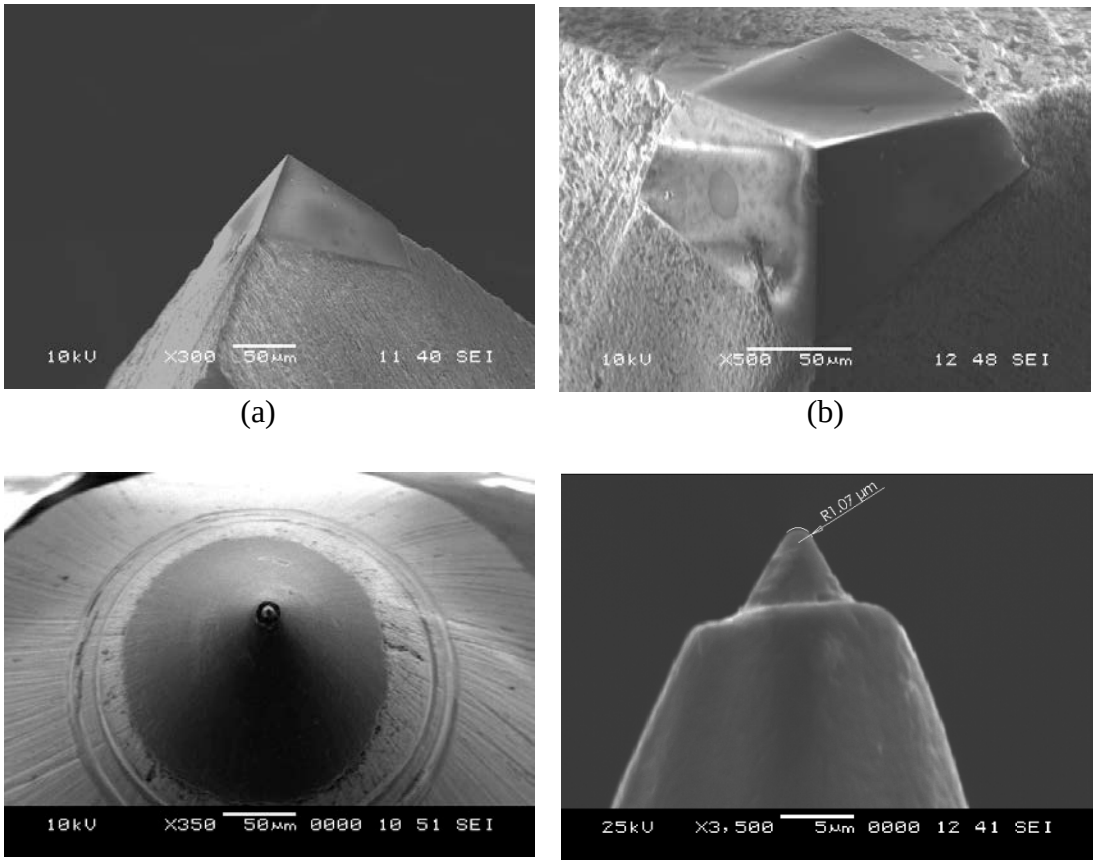

(a) (b)

(c) (d)

Figure 3.3 SEM images of cube corner (a, b) and conospherical (c, d) indenters used for nanoindentation and nanoscratch experiments. The side view (d) of conospherical tip shows the radius (1.07 μm) of the indenter.

All measurements were performed in load controlled mode with partial-unloading indent profile to allow depth profiling. The peak loads were 500 – 600 μN when measured with cube corner tip and 6000 – 8000 μN with the Berkovich tip. Maximum peak loads were slightly adjusted to have the same contact depth for different specimens. Each indent consisted of 10 partial unloadings with a progressively increasing load and each unloading segment was analyzed with the Oliver and Pharr method (Oliver et al.,

1992) to determine the hardness and reduced modulus values.

Based on Oliver and Pharr's (1992), the hardness is given by

$$H = \frac{P_{\max}}{A} \tag{3.1}$$

where P_{max} is the peak indentation load and A is the projected contact area of the indentation.

The reduced elastic modulus, $E_{r,}$ is calculated using the following equation:

$$E_r = \frac{\sqrt{\pi}}{2\beta}\frac{S}{\sqrt{A}} \tag{3.2}$$

where S is the stiffness of the tested sample and β = 1.034 for a pyramid. The elastic modulus of the test specimen can be found out from

$$\frac{1}{E_r} = \frac{1-\nu^2}{E} + \frac{1-\nu_i^2}{E_i} \tag{3.3}$$

where E, E_i, ν and ν_i are the elastic moduli and Poisson's ratio of the indenter and specimen, where E=1040 GPa, ν=0.07 for the diamond indenter.

Nanoindentation was performed also at high temperatures to characterize the nanomechanical properties of LCCO thin films at elevated temperature up to 250 °C (as they are intended for use as thermal conducting layers).

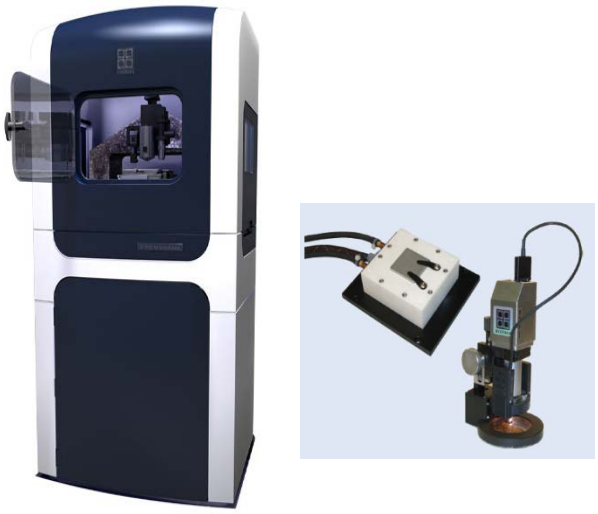

(a) (b)

Figure 3.4 Image of (a) TI 950 Triboindenter and (b) temperature control stage and heat shield used for nanoindentation at elevated temperature up to 250 °C (Hysitron Inc.).

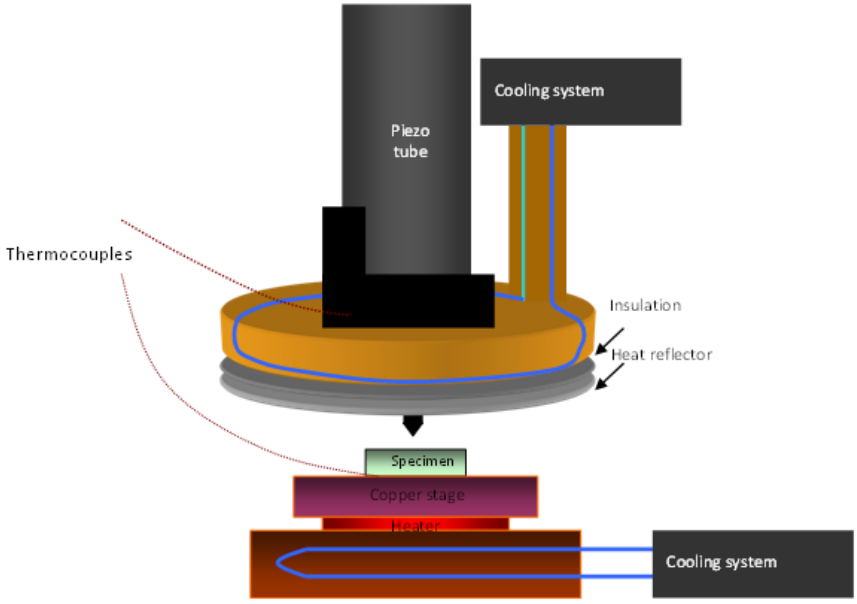

Figure 3.5 Schematic of heating stage and thermal control unit for the high temperature experiments.

A newly developed commercial instrument, a Hysitron TI 950 Triboindenter, which is equipped with a temperature control stage and heat shield was adopted in the experiment as shown in Figure 3.4. A more detailed schematic of the heating stage and thermal control unit is shown in Figure 3.5. A heat reflector is located under the transducer to protect the transducer from the heat and two thermocouples monitoring the temperature of the transducer and heated specimen are used.

Unlike nanoindentation at room temperature, nanoindentation at high temperature is not well established. Schuh et al. (Schuh et al., 2006) suggested a procedure which can produce clean load-displacement data from fused silica at elevated temperature up to 405 °C. They found that open-loop temperature control is more stable and direct contact between indenter and the heated specimen is required until the system reached the equilibrated state. However, when following the procedure as Schuh et al., different behavior of the system was observed. First, under open-loop temperature control mode, the system was not stabilized. Second, once after the contact was made with the indenter and heated specimen, a position of the transducer is moved to the negative direction and the system stopped automatically with an error signal. To avoid these two issues, a modified procedure was adopted. To minimize thermal drift of the system, the Berkovich tip used in this experiment was located around 100 nm above the surface for 20 minutes to reach equilibrium steady conditions with the heated sample, before actual indentation is made under closed-loop temperature control mode.

Nanoscratch tests were performed using a 60° conospherical tip (Figure 3.3 (c)

and (d)) with a tip end radius of 1 μm (integrated with nanoscratch tester, Triboscope TS 75) to examine the scratch behavior of LCCO thin films. A two dimensional capacitive force transducer was used to capture the force and displacement along both normal and lateral directions. The coefficient of friction, defined as the ratio of the lateral force over normal force, was calculated. The applied normal load was varied from 100 to 500 μN under 10 μm scan length and 0.33 μm/s sliding velocity, and the sliding velocity varied from 0.3 to 1.8 μm/s under normal load of 500 μN (to examine) the effect of frictional heating. Multiple-passes were performed up to 80 cycles to observe the wear resistance of the samples.

3.3. Test Results and Discussion

3.3.1 X-ray Diffraction Analysis

The film thickness was determined by the number of laser pulses and fluence applied in each deposition as seen in Table 3.1, where the sample name, deposition temperature as well as substrate material are also shown. The X-ray diffraction patterns of LCCO-Si A, B and C films grown after deposition of 7000, 5000 and 3000 pulses, respectively were obtained. The films are b-axis textured with ~ 5 polycrystalline peaks presented in the XRD plots of Figure 3.6. The highest degree of b-axis texturing is observed in the diffraction pattern of LCCO-Si A, which is the thickest film. The reflection of the Si single crystal from the last layer is of low intensity.

Table 3.1 PLD conditions used for the fabrication of all samples

Sample Name	T_{sub} (°C)	Fluence (J/cm^2)	Number of deposition pulses	Substrate
LCCO-MgO	575	5.8	10000	MgO (1 0 0)
LCCO-STO	600	2.2	7000	STO (0 0 1)
LCCO-Si	464	1.1	10000	Si:B (1 0 0)
LCCO-Si A	650	1.35	7000	Si (1 0 0)
LCCO-Si B	650	1.2	5000	Si (1 0 0)
LCCO-Si C	650	1.3	3000	Si (1 0 0)

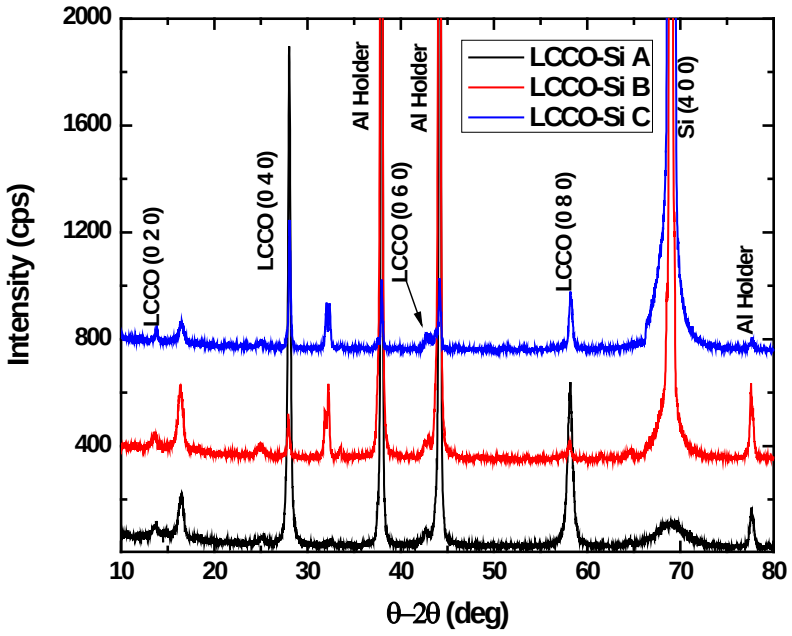

Figure 3.6 X-ray diffraction patterns of LCCO-Si A, LCCO-Si B and LCCO-Si C, respectively. The films are b-axis textured and the highest peaks are obtained from Si substrate and Al holder.

The XRD spectrum of b-axis textured LCCO-MgO thin film grown at a substrate temperature of 575°C is demonstrated in Figure 3.7. X-ray diffraction pattern from the LCCO-STO sample deposited at 600°C is plotted in Figure 3.8. In the linear plot of Figure 3.8 the film appears to be epitaxial-like while the logarithmic scale reveals low intensity LCCO polycrystalline peaks. We conclude that the LCCO-STO film is highly b-axis textured rather than epitaxial-like.

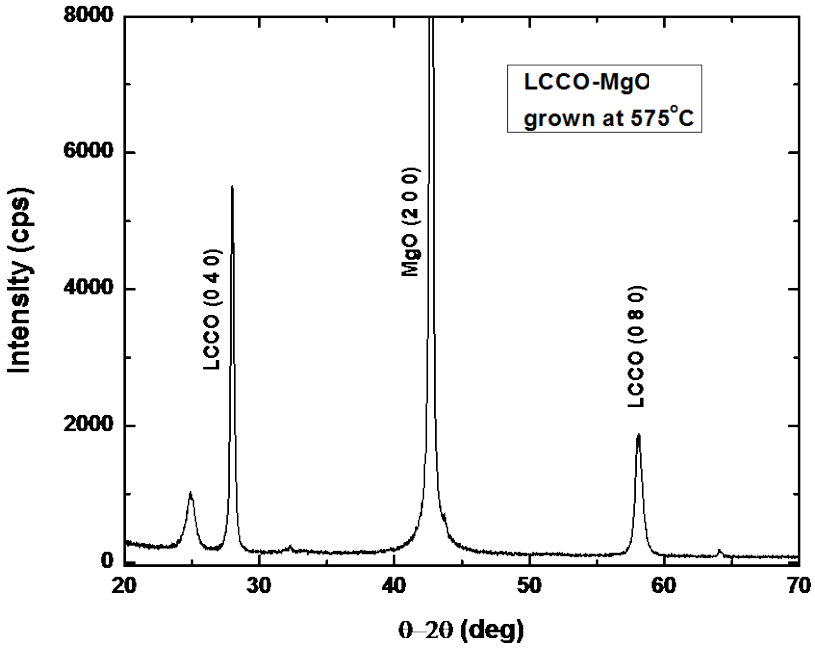

Figure 3.7 X-ray diffraction spectrum of LCCO-MgO thin film grown at substrate temperature of 575°C. The film is b-axis textured with the high intensity (2 0 0) MgO peak present.

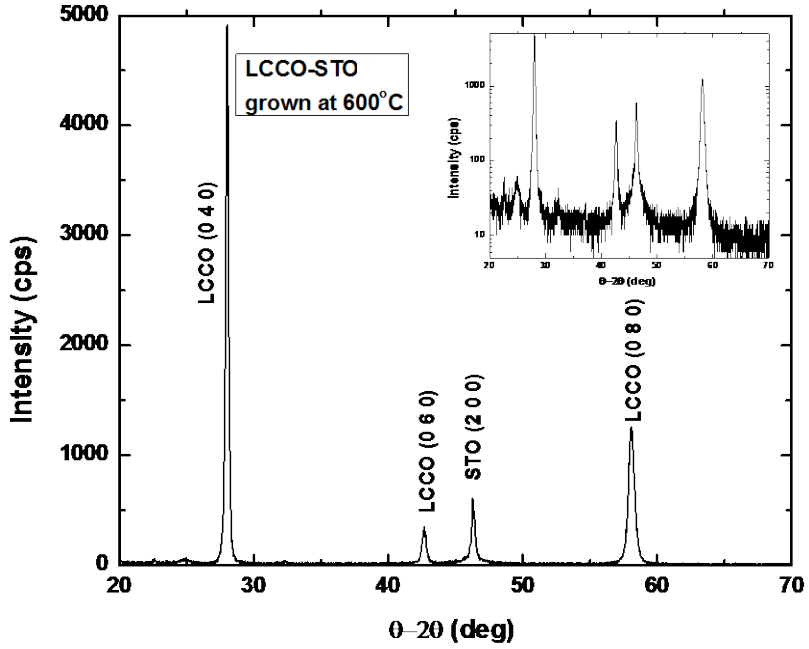

Figure 3.8 X-ray diffraction spectrum of LCCO-STO thin film grown at substrate temperature of 600°C. Inner LCCO-STO XRD plot on logarithmic scale reveals low intensity LCCO polycrystalline peaks.

3.3.2 Profiling and AFM Analysis

The thickness measurements utilizing a non-contact optical profilometer and a contact Tencor profiler were performed for six different films.

The measured step heights for LCCO-Si B using the Tencor profiler were 378 nm while 373 nm was obtained when measured with the optical profilometer as shown in Figure 3.9. Identical step height results for LCCO-Si A and C thin films using different profiling methods were also obtained. Several measurements for each specimen were performed and averaged thicknesses for LCCO-Si A, B and C were equal to 579, 378 and

190 nm, respectively and for LCCO-MgO, STO and Si were 447, 427 and 37 nm, respectively.

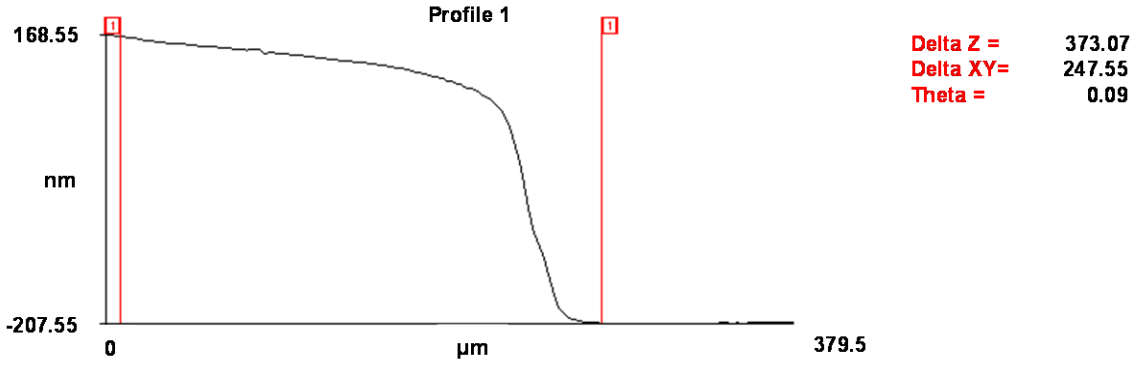

(a)

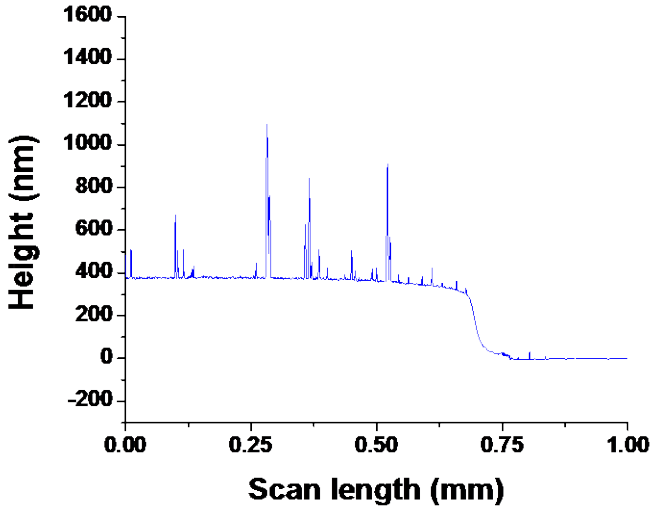

(b)

Figure 3.9 (a) Step thickness measurement of LCCO-Si B thin film using optical profiling and b) Tencor profiler. Step height equals (a) 373 nm and (b) 378 nm, respectively.

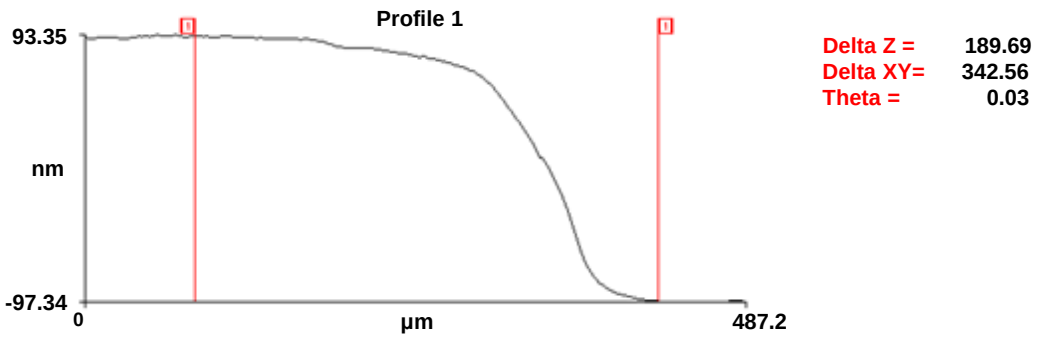

(a)

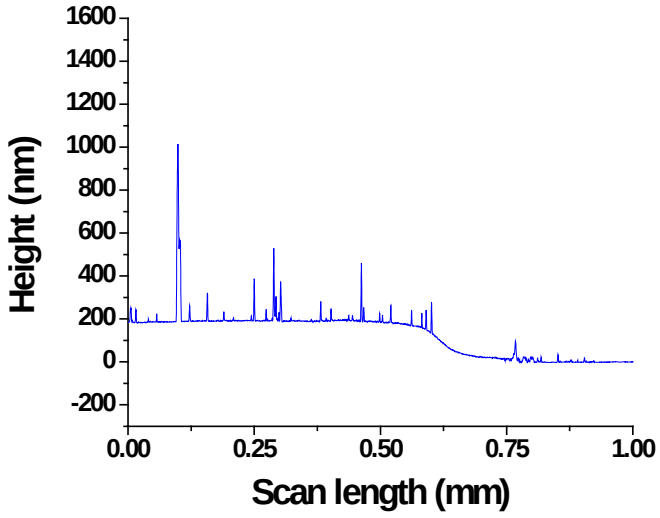

(b)

Figure 3.10 LCCO-Si C thin film step height equals 190 nm using (a) optical and (b) contact profiling.

In Figure 3.11, a typical scanning electron microscope (SEM) image of LCCO thin film grown on silicon substrate is presented. An intrinsic problem of PLD technique, particulate deposits are observed on the surface. It was found that the amount of particulates deposited on the surface is related to the value of laser fluence. However,

laser fluence cannot be lowered to a certain level to ensure ablation of the target. The lowest value of laser fluence, which is less than 1.35 Jcm^{-2}, was used for three LCCO- Si A, B and C samples. All measurements reported in this work; surface roughness, nanoindentation and nanoscratch were performed on a smooth and flat surface avoiding these deposits on the surface.

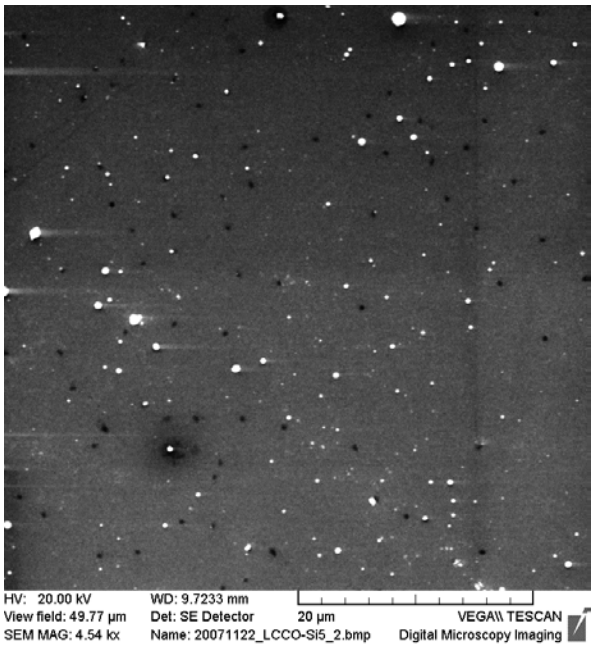

Figure 3.11 Typical scanning electron microscope image of LCCO thin film grown on Si substrate. Particulate deposits are formed on the surface as an intrinsic characteristic of PLC technique. All the roughness and mechanical property measurements were done avoiding these deposits.

The surface morphology was investigated using a multimode atomic force microscope (AFM) for three LCCO-Si A, B and C films prepared using PLD and bulk LCCO which has crystallographic orientation along c-axis. The obtained images of (a) LCCO-Si A, (b) LCCO-Si B, (c) LCCO-Si C and (d) Si substrate with a scan size of 2×2

μm^2 and (e) LCCO-bulk with a scan size of 5×5 μm^2 are shown in Figure 3.12. It appears that granular growth is taking place at the first 3000 to 5000 deposition pulses losing the grain boundaries at 7000 pulses. The continuous but granular LCCO films in Figure 3.12 (b) and (c) implicate that the first laser pulses aid the nucleation of islands or atomic layer and islands. The thickest film LCCO-Si A exhibits the lowest RMS roughness of 3.56 nm while LCCO-Si B and C show 10.16 nm and 5.58 nm, respectively. The RMS roughness of Si substrate used for three samples is 0.30 nm. LCCO-bulk specimen has lower RMS roughness than other thin film samples, which is equal to 1.70 nm although scratch marks are observed, likely due to the lapping process.

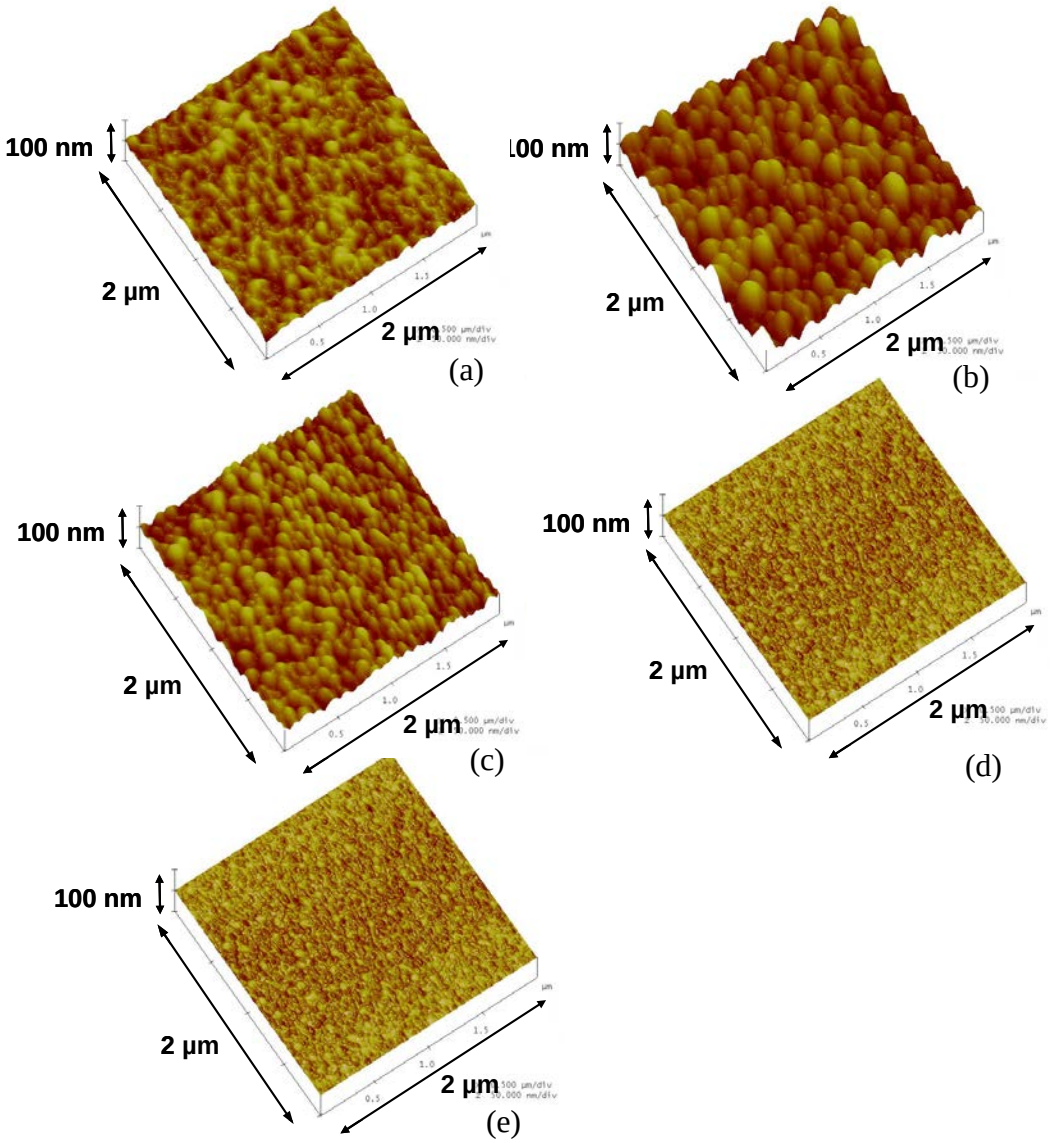

Figure 3.12 AFM images of (a) LCCO-Si A thin film after 7000 deposition pulses, (b) LCCO-Si B grown using 5000 pulses, (c) LCCO-Si C prepared after 3000 pulses, (d) Si substrate and (e) LCCO-bulk. The RMS roughness values for LCCO-Si A, B, C, Si substrate and LCCO-bulk are 3.56, 10.16, 5.58, 0.3 and 1.7 nm, respectively.

3.3.3 Nanoindentation and Nanoscratch Measurements

Figure 3.13 shows load-displacement curves for LCCO-Si A thin film measured with the cube corner and Berkovich tips with partial-unloading indent profile.

Figure 3.14 and Figure 3.15 shows the resultant averaged values of 5 nanoindentation experiments for LCCO films, bulk LCCO and Si substrate where hardness and elastic modulus are plotted as a function of contact depth, h_c. The error bar in the plot represents ± one standard deviation. The solid lines in Figure 3.15 represent curve fitted results with 2nd order polynomial equation to aid data visualization.

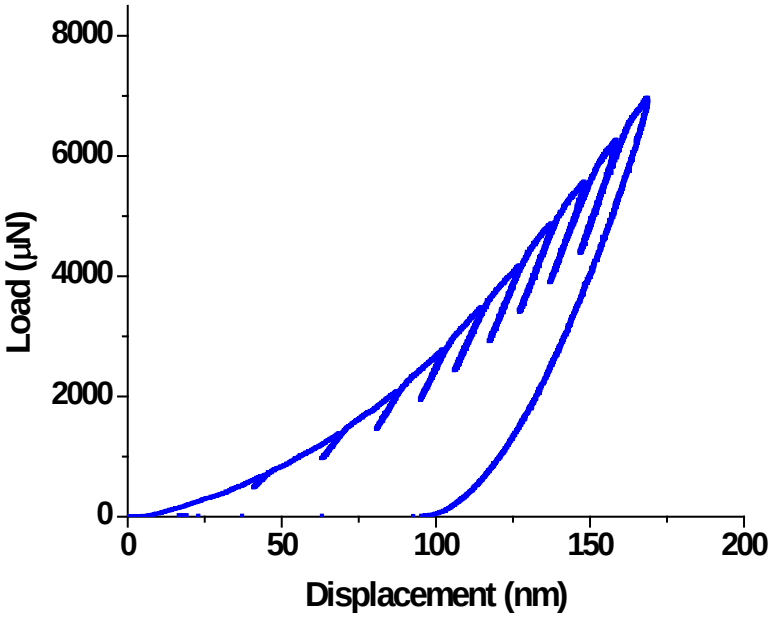

(a)

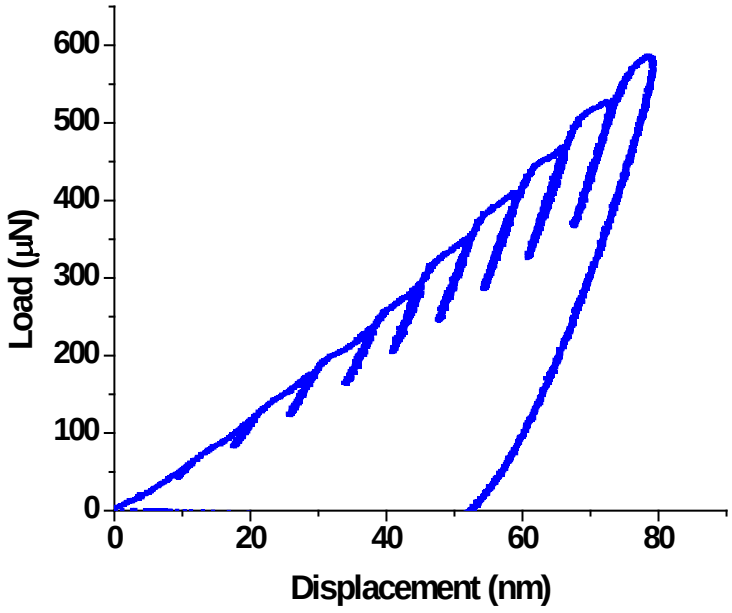

(b)

Figure 3.13 Load-displacement curves for LCCO-Si A thin film with partial-unloading indent profiles measured with (a) cube corner tip and (b) Berkovich tip.

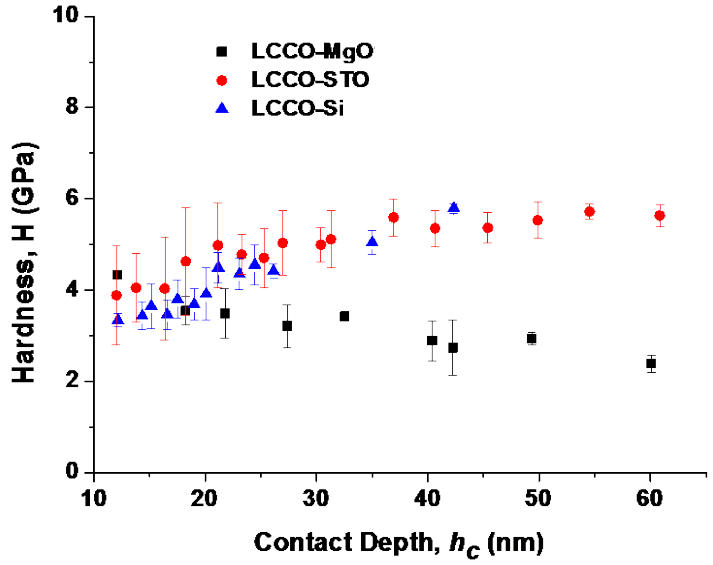

(a)

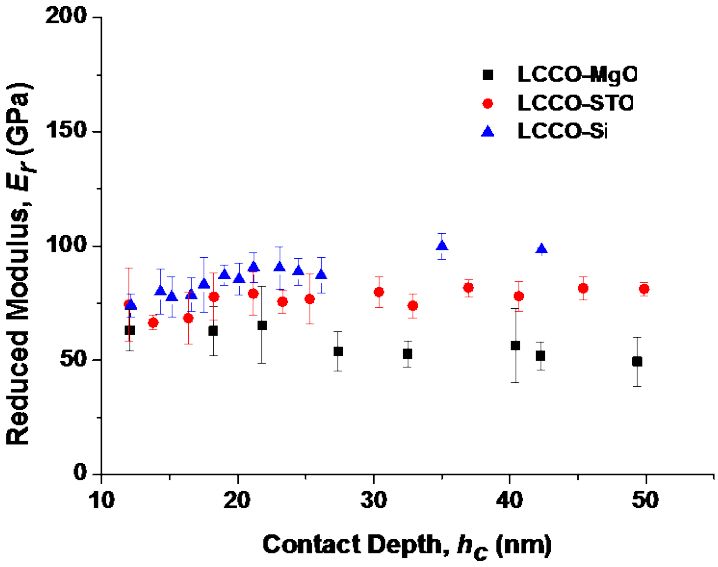

(b)

Figure 3.14 Plots of (a) reduced modulus and (b) hardness versus contact depth for LCCO-MgO, LCCO-STO and LCCO-Si films.

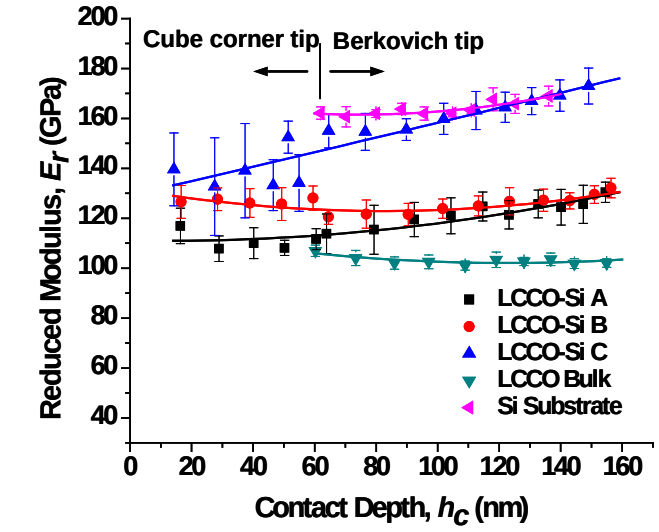

(a)

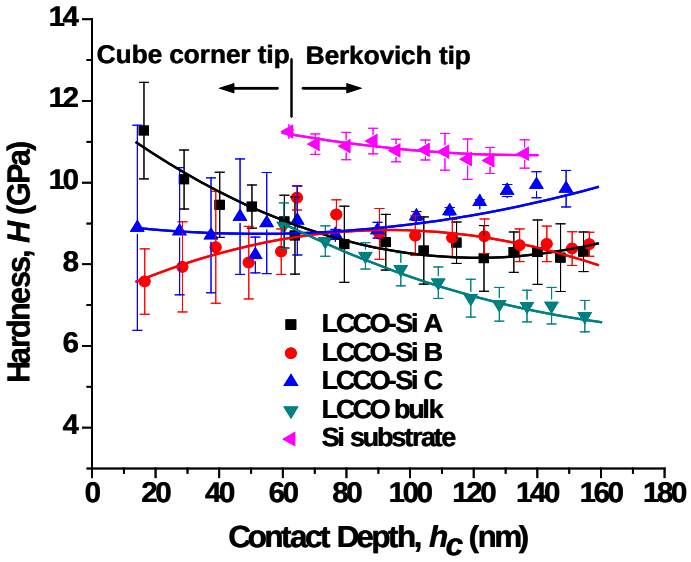

(b)

Figure 3.15 Plots of (a) reduced modulus and (b) hardness versus contact depth measured with cube corner and Berkovich tips. Overlapped solid lines represent curve fitting lines generated with 2nd order polynomial equation.

The overall trends of the obtained data show that the reduced modulus increases with increasing contact depth and asymptotically approach that of Si substrate (E_r=163 GPa). In the case of hardness, the highest hardness (11.3 GPa) was obtained from LCCO-Si A at the lowest contact depth of 16.4 nm and starts to decrease. LCCO-Si B and C have the highest hardness at a certain contact depth (LCCO-Si B: H=9.6 GPa at h_c=64.5 nm and LCCO-Si C: H=9.9 GPa at h_c=147 nm). LCCO films deposited on Si substrate appear to be softer than the substrate, so in case of LCCO-Si C which is the thinnest film (190 nm) among which plotted in Figure 3.15, hardness values quickly approach that of substrate (H=10.8 GPa) under a given Max. contact depth of ~150 nm as seen from Figure 3.15 (b). Considering the so called 10 % rule, or Buckle's rule (Buckle, 1965), the true hardness of the sample should be obtained at indentation depths less than 10 % of the film thickness to avoid substrate effects. Averaged reduced modulus values of five measurements for three samples of LCCO-A, B and C measured at indentation depths less than 10 % of film thickness were found to be in the range of 105.3 GPa-139.6 GPa. Hardness values measured at indentation depths less than 10 % of the film thickness were in the range of 7.6-11.3 GPa. For comparison purposes, additional nanoindenation tests were conducted with the bulk LCCO, and plotted together with the thin film samples in Figure 3.15. When compared with the other samples, bulk LCCO material which has crystallographic orientation along c-axis has averaged values of reduced modulus, and hardness has 102.4 and 7.6 GPa, respectively. It can be assessed that LCCO is anisotropic material which has different nanomechanical properties in different crystallographic

directions.

Figure 3.16 shows averaged hardness and reduced modulus values of 5 measurements on LCCO-Si A sample at various temperatures of 50, 100, 150, 200 and 250 °C at 100 nm contact depth. Error bars represent standard deviation of 5 measurements. As seen in Figure 3.16, the standard deviation is pretty large compared with the results performed at room temperature (shown in Figure 3.15). This is because even with the closed-loop temperature control, thermal drift of 1.3 nm/s was detected during measurements. However, the overall trends in Figure 3.16 show that LCCO-Si A sample has pretty stable behavior with respect to the change of temperature up to 250 °C.

The average measured coefficients of friction are presented in Figure 3.17. Figure 3.17 (a) shows the average friction coefficient measured under 100, 200, 300, 400, and 500 μN applied normal load. LCCO-Si A shows the lowest friction coefficient among the three tested samples, which is around 0.15 independent of the applied normal load. The friction coefficient of LCCO-Si B increases starting from 0.22 at 100 μN normal load and reaches to 0.27 at 500 μN normal load. LCCO-Si C shows small decrease with the increased normal load varying from 0.3 to 0.27.

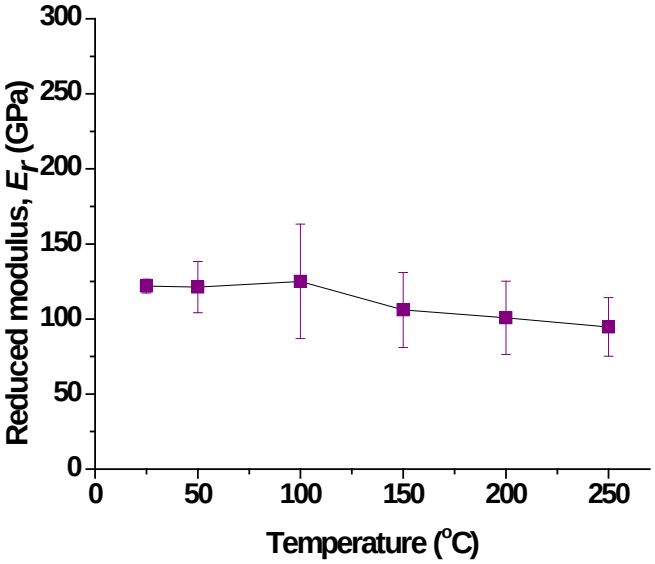

(a)

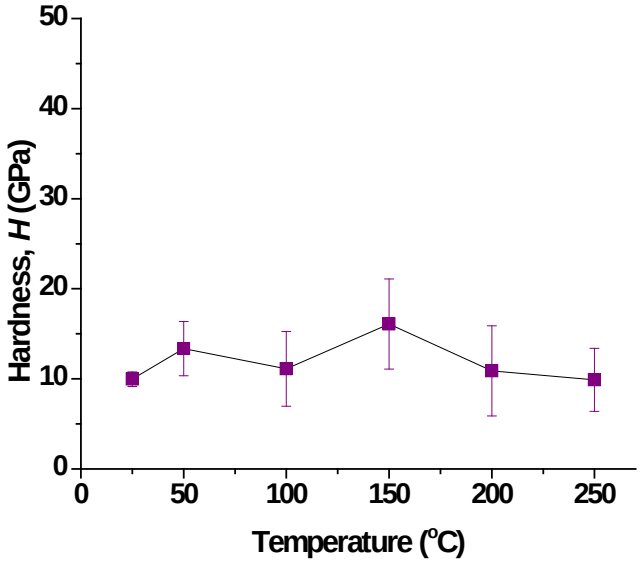

(b)

Figure 3.16 Plots of (a) reduced modulus and (b) hardness measured at elevated temperatures of 50, 100, 150, 200 and 250 °C with Berkovich tip at 100 nm contact depth.

Figure 3.17 (b) shows the results of the friction coefficient measurements under various sliding velocities from 0.33 to 1.65 μm/s. LCCO-Si A sample has approximately constant friction coefficient of 0.27 over all sliding velocities. The friction coefficient of LCCO-Si B and C drops suddenly after 0.66 μm/s sliding velocity and maintains a value of ~0.1.

Figure 3.17 (c) shows the friction coefficient variation with the number of passes. Multiple pass tests show that the friction coefficient of LCCO Si A and B is stable against repeated scratches. The friction coefficient of LCCO-Si C increases and reaches around 0.19 after a sudden drop at 5 cycles.

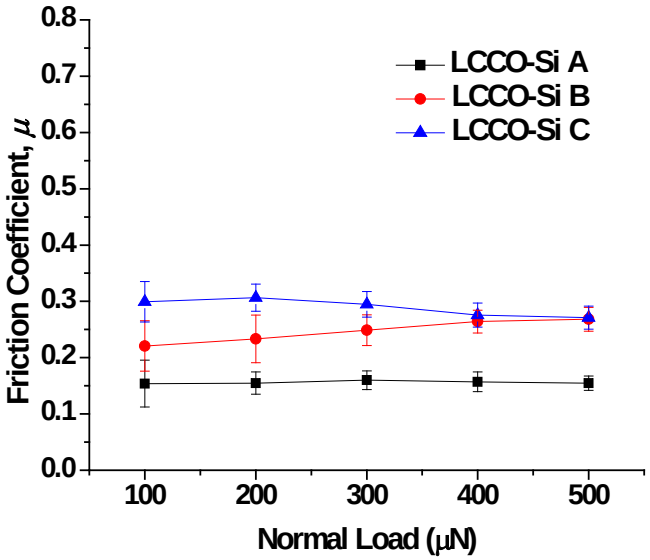

(a)

Figure 3.17 (cont. on next page)

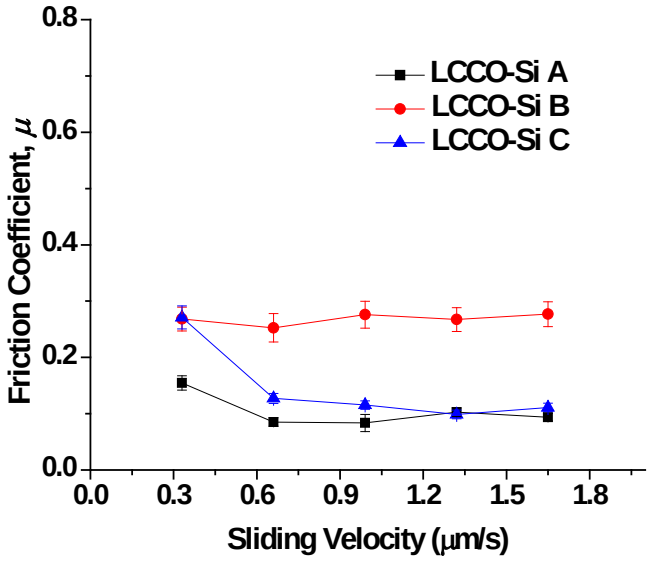

(b)

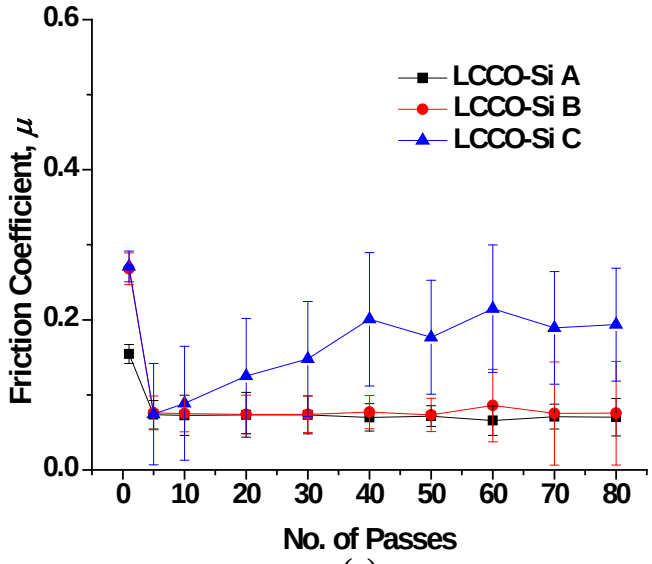

(c)

Figure 3.17 Plots of friction coefficients measured at various (a) applied normal load with fixed sliding velocity of 0.33 μm/s, (b) sliding velocity with fixed normal load of 500 μN and (c) number of passes under 500 μN normal load and 0.33 μm/s sliding velocity for LCCO thin films.

Figure 3.18 shows AFM images obtained from scratched surfaces of LCCO-Si C with various normal loads of 100 μN - 500 μN. In the case of LCCO-Si A (Figure 3.17) and B, there were no observable residual tracks at a given normal load. This reflects the fact that the surface deforms elastically during the scratch experiment. In the case of LCCO-Si C, wear tracks become deeper as the normal loads are increased. For example, measured wear depths at 200 μN and 500 μN normal loads for LCCO-Si C are 7.5 nm and 10.16 nm, respectively. However, no observable delamination or cracks are found on the surface.

Representative values of thickness, hardness, reduced modulus and friction coefficient of LCCO thin films obtained in this work are listed in Table 3.2.

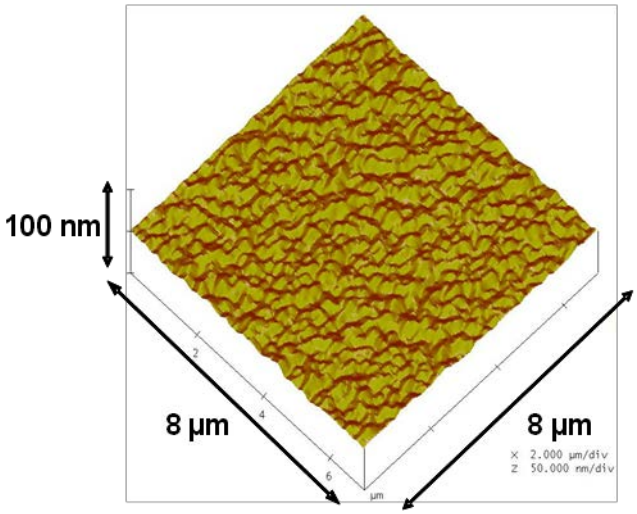

(a)

Figure 3.18 (cont. on next page)

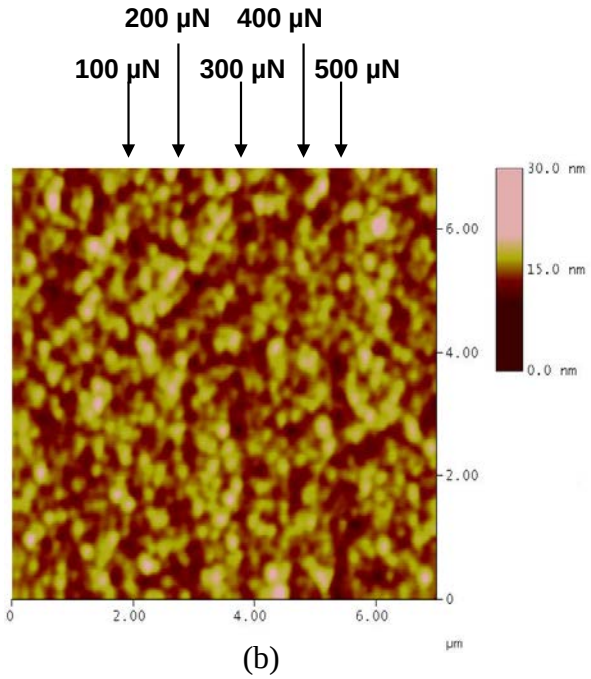

(b)

Figure 3.18 AFM (a) isomeric view and (b) top view images of scratch tracks at various loads from 100 µN to 500 µN with 0.33 µm/s sliding velocity for LCCO-Si A.

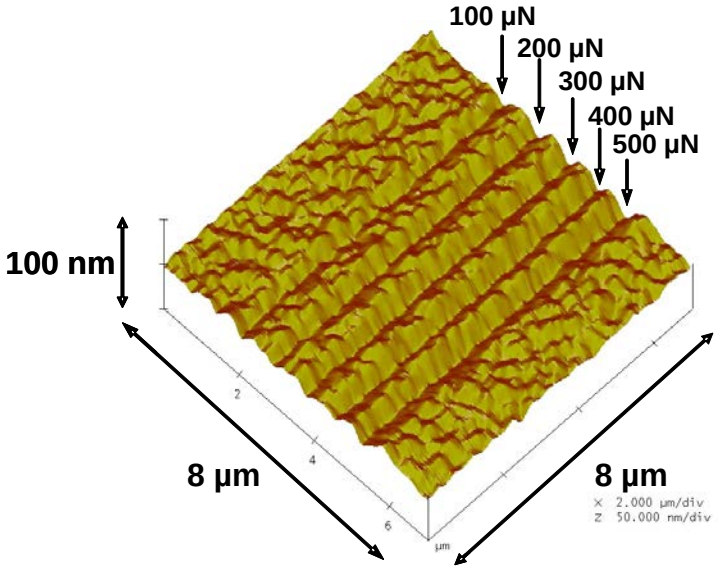

(a)

Figure 3.19 (cont. on next page)

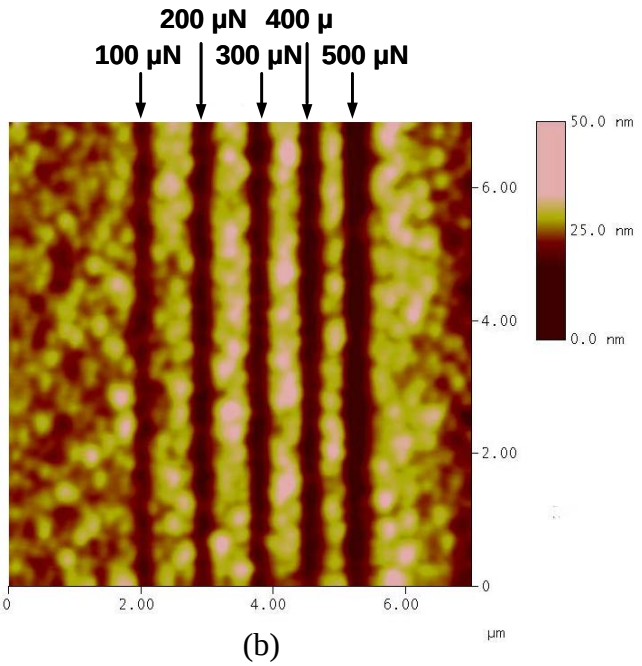

(b)

Figure 3.19 AFM (a) isomeric view and (b) top view images of scratch tracks at various loads from 100 µN to 500 µN with 0.33 µm/s sliding velocity for LCCO-Si C.

Table 3.2 Nanomechanical properties obtained from step height measurement, AFM, nanoindentation and nanoscratch experiments for LCCO thin films

Sample Name	**Thickness (nm)**	**RMS Roughness (nm)**	E_r **(GPa)**	H **(GPa)**	**Friction Coefficient**
LCCO-MgO	447	13	62.8	3.5	0.25
LCCO-STO	427	2.5	81.5	5.4	0.1
LCCO-Si	37	2.3	87.2	3.7	0.12
LCCO-Si A	579	3.56	117	11.3	0.15
LCCO-Si B	378	10.16	127.6	8.4	0.26
LCCO-Si C	190	5.58	139.6	8.9	0.27

- The friction coefficients are obtained at 100 µN normal load and 0.33 µm/s sliding velocity
- E_r and H are the highest values obtained at the indentation depth less than 10 % of the film thickness except LCCO-Si (measured at contact depth of 19 nm).

3.4 Summary

The nanomechanical properties such as hardness, modulus of elasticity, and friction coefficient of stoichiometric LCCO thin films grown on Si substrate using the PLD technique in oxygen environment were investigated using nanoindentation and nanoscratch techniques. X-Ray diffraction analysis revealed b-axis texturing in all films. The thickness of the films varied from 37 nm to 579 nm and was controlled by the number of ablation pulses and the laser fluence applied in each deposition. The smoothest film was LCCO-Si with RMS values of 2.3 nm. The hardest (H=11.3 GPa) film was LCCO-Si A prepared using 7000 pulses. The lowest friction coefficient of ~0.1 was obtained from LCCO-STO under 0.33 μm/s sliding velocity.

Finally, we can conclude that LCCO materials can be attractive candidates as a nanothermal layer to substitute currently widely used DLC in a sense that these materials meet the demands that require sufficient thermal conductivity, Young's modulus, hardness and wear resistance, all of which are the critical components in MEMS and hard disks.

4. Effect of Roughness on the Contact of Microscale Thin-films: Experimental Study and Comparison with Existing Models

4.1. Introduction

The contact behavior of two rough surfaces is of great interest in the field of tribology. A pioneering model of elastic contact between rough surfaces was developed by Greenwood-Williamson for elastic rough surfaces (GW model) (Greenwood et al., 1966). It models the rough surface as a statistical distribution of asperities with various heights. This model was a breakthrough since the complex problem of random nature of rough surfaces was reasonably captured with such simplicity. This model was further extended by other researchers, e.g., Chang et al. (CEB model) (Chang et al., 1987), and Kogut and Etsion (KE model) (Kogut et al., 2002) to include plasticity. Chang et al. (CEB model) extends GW model to plastic regime and takes into account the plastic deformation of contacting asperities using an analytical approach. KE model solved the hemispherical contact problem using the finite element method and obtained contact constitutive laws for the relevant regime of deformation (elastic, elastically contained plastic and fully plastic); this was later extended to rough surface contact similar to the GW model. However, all these models assumed that the interactions between asperities were insignificant. It is assumed that the asperities are far apart, thus the contact of a single asperity does not affect the contact behavior of adjacent asperities. But, in reality the contact of one asperity will cause a deformation around it such that it would result in shifting the original base position of the adjacent asperities. Pullen and Williamson

(Pullen et al., 1972) first observed the effect that an asperity contact shifts the positions of adjacent asperities.

Eid and Adams (Eid et al., 2007) indicated the importance of the effect of asperity interaction by studying an elastic-perfectly plastic finite element model of two hemispheres in contact with a rigid flat. Many researchers have attempted to include the effect of asperity interactions in rough surface contact models (Ju et al., 1992; Zhao et al., 2001; Iida et al., 2003, Ciavarella et al., 2006; Yeo et al., 2010). Ju et al. (Ju et al., 1992) used Boussinesq's elastic force-displacement integral equation to account for the asperity interaction. Zhao and Chang (Zhao et al. 2001) presented an elastic perfectly plastic micro-contact model of rough surfaces including asperity interactions by using Saint-Venant's principle in conjunction with Love's formula. Iida et al. (Iida et al., 2003) accounted for asperity interactions by calculating the contact-induced displacement of adjacent asperity positions using a Green's function-based solution to capture the deformation profile. Ciavarella et al. (Ciavarella et al., 2008) formulated an improved version of the GW model with the inclusion of interaction between asperities (CGP model). They treated the contact pressure distributed uniformly over an apparent contact area and the resulting deformation occurred based on Timoshenko and Goodier equations (Timoshenko et al., 1951) (See appendix C. for further details).

Furthermore, today's applications such as magnetic storage hard disk drives and MEMS have thin coating layers as an effective means to provide reliable contact performance. Especially, a diamond-like carbon overcoat (DLC) on magnetic storage

disks should protect the important magnetic layer underneath it against contact-induced stresses of head slider. The thickness of the DLC should be tightly controlled to a few nanometers so that the spacing between the magnetic layer and the head is kept at a minimum to achieve high density of magnetic storage. Rough surface contact behavior for such layered systems was proposed by Yeo et al. (Yeo et al., 2010) including asperity interaction effects. They extended a single asperity model of stiffer asperity sitting on a compliant substrate to a discrete Gaussian distribution of asperities representing a realistic rough surface and observed a fairly good comparison with experimental observations. All the modeling approaches described above provide a method to determine the contact of rough surfaces.

However, there is limited experimental data to correlate with the above models due to complexity in experimentation at such small scales (Yoder et al., 1998; Goerke et al., 2008; Shi et al., 2005; Berasategui et al., 2003; Asif et al., 2001).

As a direct method of measuring contact stiffness, the nanoindentation technique can be used. Li et al. carried out nanoindentation experiments (Li et al., 2000). They measured the contact stiffness of homogeneous materials like fused silica and PTFE, and showed that the contact stiffness increased with increasing depth. Although they successfully characterized the contact stiffness of homogeneous materials, they did not consider the effect of roughness and substrate because a sharp tip penetrated the surface as the contact depth was increased. Furthermore, an exact analysis of a commonly used triangular-based pyramidal indenter like Berkovich tip requires numerical computations

(King, 1987). Gao (Gao et al., 1993) modeled the contact behavior of flat-ended triangular tip and confirmed that the contact stiffness associated with the nanoindenter can be measured insensitive to the cross-sectional shape of the punch. When using the flat-ended punch, contact stiffness can be directly obtained from the initial slope of the load-displacement curve during unloading since the contact area remains nearly constant.

Another method measuring contact stiffness was used by Shi et al. (Shi et al., 2005; Shi et al., 2008), where a dynamic stiffness tester is utilized based on the resonant frequency method originally suggested by Serpe (Serpe, 1999). They extracted some parameters, which are related to the contact stiffness and contact damping, and obtained contact stiffness and contact damping through the known dynamic system model. They measured contact stiffness for both spherical contacts and flat rough surfaces in contact and found that contact stiffness was overpredicted when compared with existing contact models without asperity interaction. Yeo et al. proposed a contact model accounting for both the effect of hard coating on the asperity and asperity interactions and will be compared with the experiments. However, when analyzing the experimental results for flat rough surfaces in contact, a certain nominal area of contact was assumed because the actual slider used in the experiments had a certain amount of curvature on the surface (Shi et al., 2008).

In this work, both a nanoindentation tester integrated with a flat tip and a dynamic stiffness tester were utilized to measure the contact stiffness of well controlled “truly” flat layered surfaces. The measured contact stiffness results obtained from the two different

testers representing the contact stiffness of the corresponding rough surface were compared with the existing rough surface contact models.

4.2. Experimental Setup

4.2.1 Dynamic Contact Stiffness Tester

A dynamic contact stiffness tester was developed to conduct the experiments as shown in Figure 4.1. The samples to be tested are mounted on the specimen mount as shown in Figure 4.1 (a) and sapphire glass is attached on the other upper sample mount as a counter contacting surface to the specimen. These two mounts are tightly connected to masses and continuously connected to tube springs. The contact load between the two specimens is controlled by using a micrometer. The actual applied contact load is measured by strain gauges attached to the lower tube spring. A small impacting rod located on top of the tester is used to exert the impact force on the top side of the upper mass. The motion of the system is measured with the accelerometer attached on the top surface of the lower mass.

The resonance frequency at the interface is determined from the structural dynamics of the tester. The simplified system dynamic model of the tester is shown in Figure 4.2. and the system dynamic equations of motion have the following form.

$$m_1\ddot{x}_1 - \zeta_c(\dot{x}_2 - \dot{x}_1) + k_c(x_1 - x_2) + k_1 x_1 = m_1 g \quad (4.1)$$

$$m_2\ddot{x}_2 + \zeta_c(\dot{x}_2 - \dot{x}_1) - k_c(x_1 - x_2) + k_2 x_2 = m_2 g \quad (4.2)$$

where m_1 and m_2 are masses of sample mounts and masses, k_1 and k_2 are spring constants of the tube springs, k_c is the contact stiffness at the interface, and ζ_c is the

damping constant at the interface.

The system dynamic equations of motion in Eq. (4.1) and (4.2) become the algebraic eigenvalue problem. The determinant of the coefficient of algebraic eigenvalue problem becomes

$$\begin{vmatrix} -m_1\omega^2 + j\zeta_c\omega + k_c + k_1 & -j\zeta_c\omega - k_c \\ -j\zeta_c\omega - k_c & -m_2\omega^2 + j\zeta_c\omega + k_c + k_2 \end{vmatrix} = 0 \tag{4.3}$$

Solving for the contact stiffness of the characteristic equations, its value is given by

$$k_c = \frac{m_1 m_2 \omega^4 - (m_1 k_2 + m_2 k_1)\omega^2 + k_1 k_2}{(m_1 + m_2)\omega^2 - (k_1 + k_2)} - j\zeta_c\omega \tag{4.4}$$

The equation for contact stiffness, Eq. (4.4), contains an imaginary part, which means that the contact stiffness is affected by the presence of damping. But, the imaginary part is ignored in calculating the contact stiffness since the effect of damping is small and only the real part in Eq. (4.4) is taken to obtain the contact stiffness. In typical tests, two resonance frequencies can be obtained from the acceleration signal. The system resonance frequency will be constant independent of the contact load, while the contact resonance frequency will shift as the contact load increases (Shi et al., 2005).

Initially, a specially-built dynamic stiffness tester was developed by Shi (Shi, 2005) for the measurements of contact stiffness and contact damping in the load range of 100 mN~1000 mN. Afterward, several modifications were made to measure the contact stiffness and contact damping for magnetic storage head disk interface samples. In order

to perform these experiments, focusing on the light load range less than 100 mN, the tester was modified further to have higher sensitivity than the previous version by reducing the spring constants of the two tube springs and masses in the tester. The current version of the dynamic stiffness tester has two tube springs made of stainless steel with wall thickness of 0.15 mm. The length and diameter of the tube springs are 32 and 19 mm, respectively. The spring sensitivity estimated by ANSYS is 5.29 μm/N. The amount of mass in the system was designed to have the system resonant frequency several hundreds of hertz lower than the contact resonance. The optimized total weight of the sample mount and mass was 48 mg.

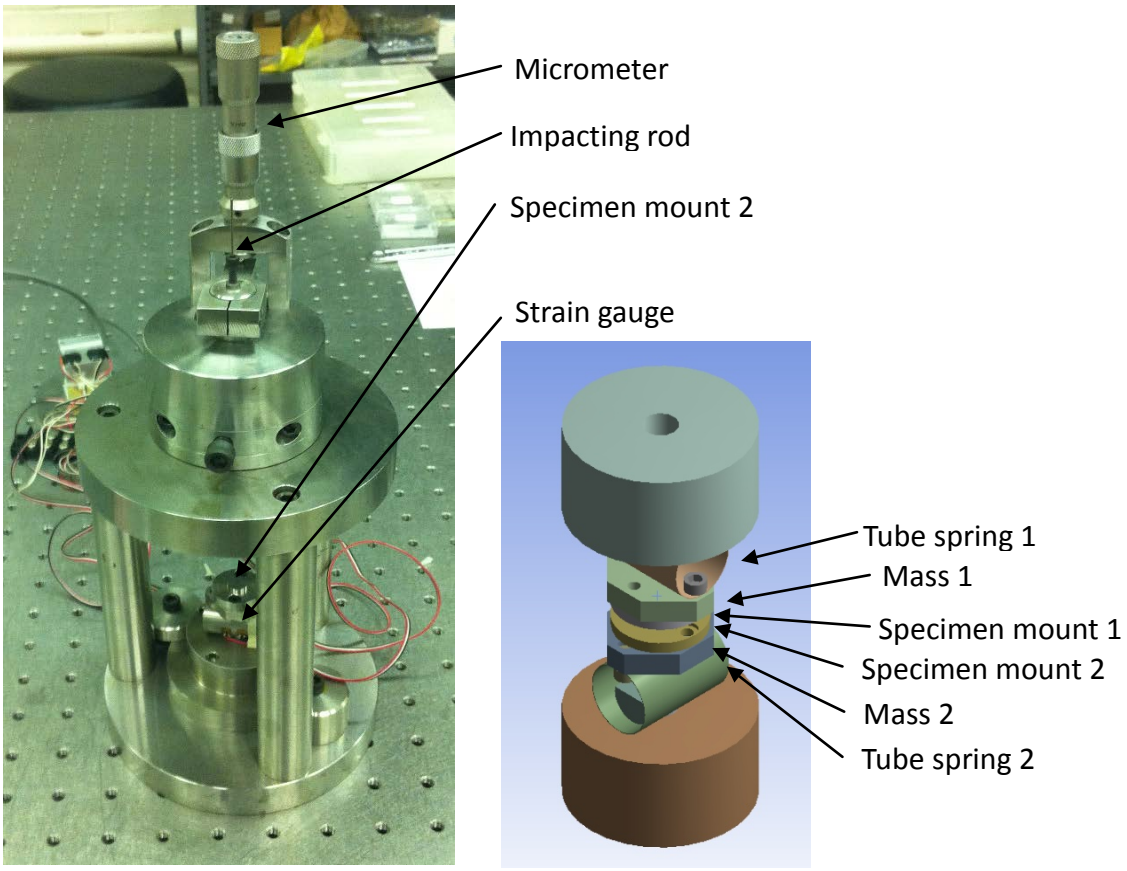

(a) (b)

Figure 4.1 Dynamic contact stiffness tester: (a) actual view of complete tester (b) solid model of tube springs and masses.

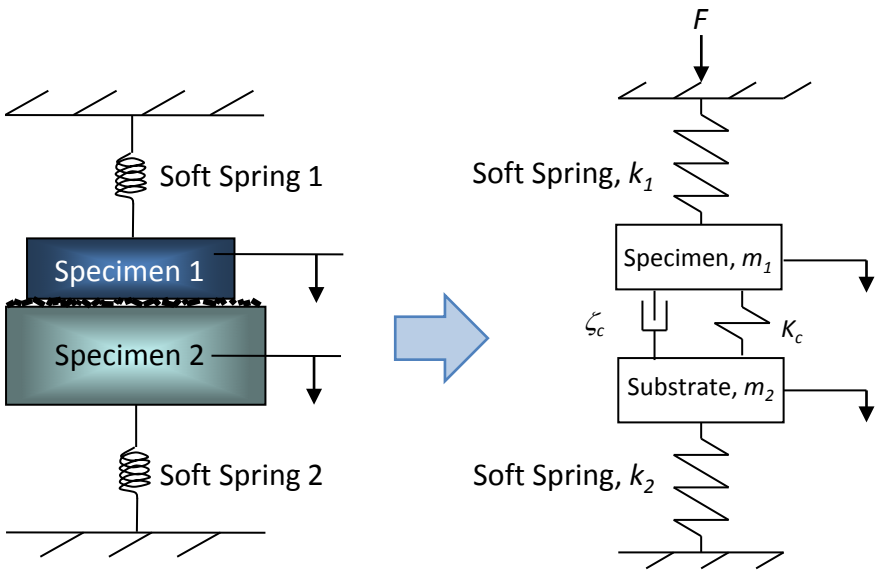

Figure 4.2 System dynamic model of dynamic stiffness tester.

4.2.2 Contact Stiffness Measurement Using the Nanoindentation Tester

The experiments of the flat punch tip indenting the samples were performed using a commercially available nanoindenting instrument (Triboscope TS 75, Hysitron). The instrument has a three-plate capacitive load-displacement transducer with a force resolution of 100 nN and displacement resolution of 0.2 nm. The transducer assembly with an electrostatic force actuator is attached to a multi-mode AFM to perform the measurements. The specimen itself is mounted on a piezo scanner.

A flat tip used in this work was microfabricated using a focused ion beam (FIB) (FEI DB235). Figure 4.3 shows a SEM image of the flattened tip used for the experiments. The flat region has a triangular shape and a total nominal area of 21.21 μm^2 with a root-mean-square roughness (R_q) of 3.44 nm. A flat tip with such a large nominal

area was used such that the area encompasses a rough surface asperity distribution. On the other hand, a conventional sharp tip has a much smaller contact area and cannot be used to examine roughness effect. Also higher contact loads can be used for larger nominal areas.

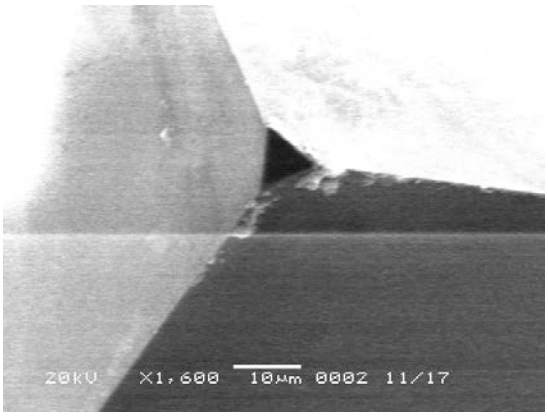

Figure 4.3 SEM image of flattened diamond indenter tip fabricated with focused ion beam.

4.2.3 Sample Preparation

Five different samples were prepared to examine the effect of roughness as well as the effect of the presence of thin-films. They were:

1. Two thin-film samples with 4 nm thick DLC layer on an Aluminum Oxide-Titanium Carbide (Al2O3-TiC or AlTiC in short) substrate with different roughness: Samples 1 and 2.

2. Two samples made of AlTiC with different roughness: Samples 3 and 4.

3. One multilayer sample with 20 nm Titanium (Ti) layer deposited on a 200 nm thick

layer of Gold (Au). The Au layer is deposited on a Silicon (Si) substrate, with a 20 nm Ti present as an adhesion layer: Sample 5.

Table 4.1 List of specimens and tip used in the experiments with roughness parameters, critical interference and plasticity indices.

Sample	Name	R_q (nm)	R (μm)	η (μm^2)	E_1 (GPa)	E_2 (GPa)	ω_c (nm)	ψ
1	Smooth DLC on AlTiC	0.74	1.47	41.88	139.6	390	24.3	0.36
2	Rough DLC on AlTiC	3.45	0.72	25.27	139.6	390	22.88	0.45
3	Smooth AlTiC	0.46	0.63	141.7	390		2.56	1.14
4	Rough AlTiC	3.43	0.66	25.19	390		2.66	1.31
5	Ti/Au	1.68	0.29	54.55	116	77.2	0.13	5.29
	Tip	3.44	1.5	10	925			

R_q: root-mean-square roughness of asperity heights, R: average radius of asperities, η: areal density of asperities, E_1: elastic modulus of top layer, E_2: elastic modulus of substrate, ω_c: critical interference ($=(\pi KH/(2E))^2 R$) and ψ: plasticity index ($=(2E/(\pi KH))(R_q/R)^{1/2}$) where K is the maximum contact pressure factor (Tabor, 1951; Chang et al., 1987).

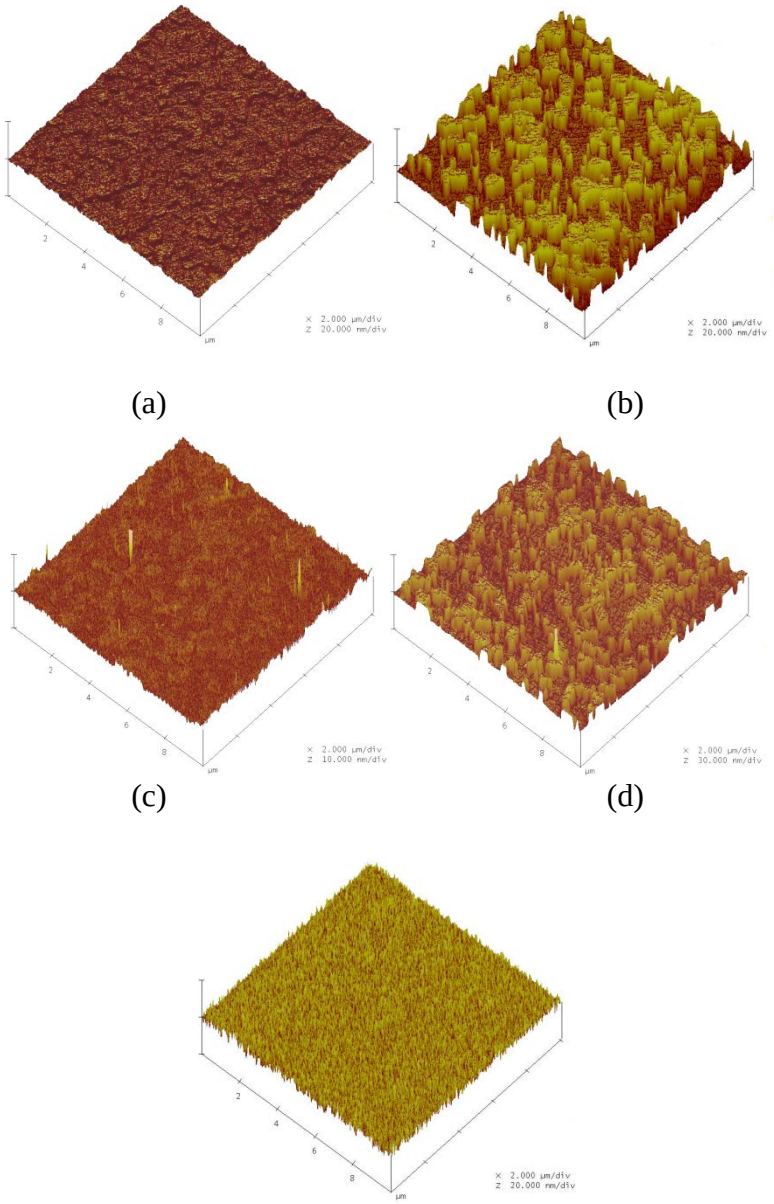

Figure 4.4 AFM images of the samples (a) smooth DLC on AlTiC (R_q=0.735 nm) (b) rough DLC on AlTiC (R_q=3.45 nm) (c) smooth AlTiC (R_q=0.46 nm) (d) rough AlTiC (R_q=3.43 nm) (e) Ti on Au (R_q=1.68 nm).

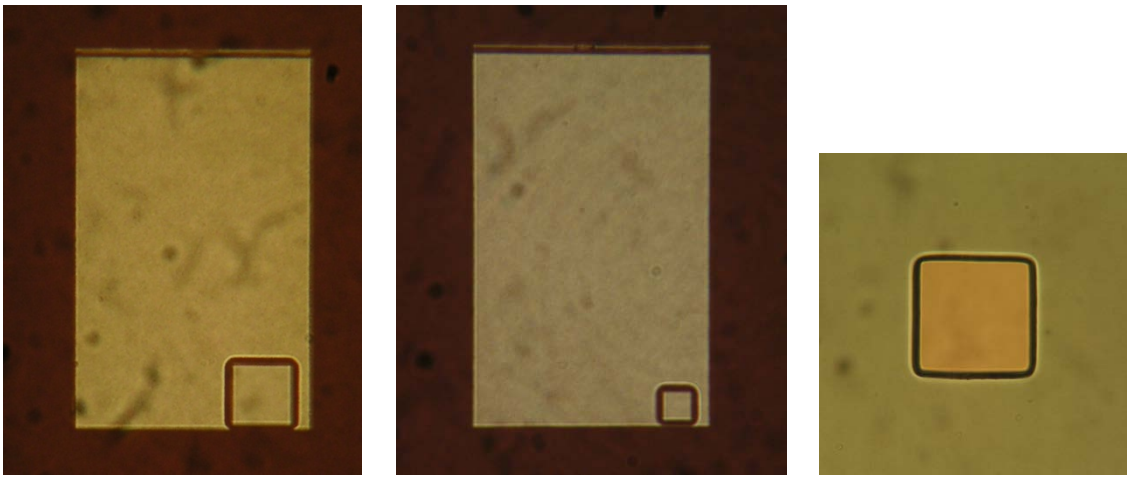

(a) (b) (c)

Figure 4.5 Optical microscopic images of the samples used in the experiment (a) for sample 1 to 5 with a nominal pedestal area of 40,000 μm^2 and (b) for sample 1 to 5 with a pedestal area of 10,000 μm^2, and (c) for sample 5 with a nominal pedestal area of 40,000 μm^2.

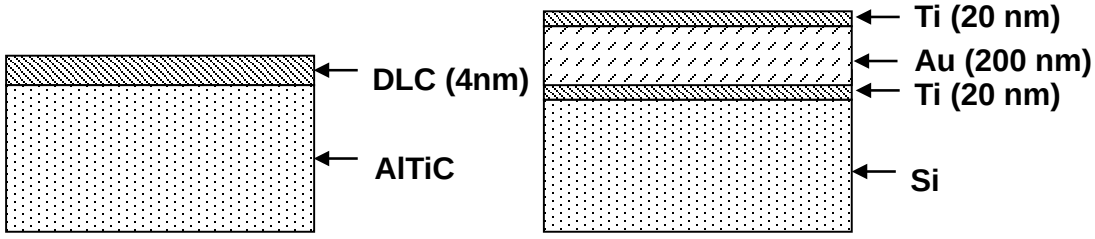

(a) (b)

Figure 4.6 Schematic of cross-section of thin-layered film. (a) 4 nm thick DLC is deposited on AlTiC substrate for sample 1 and 2 and (b) a harder 20 nm thick Ti is deposited on a softer 200 nm Au layer for sample 5.

The surface topographies of the samples measured using an AFM with a scan size of 10×10 μm^2 are shown in Figure 4.4 and optical microscopic images of the samples

used in the experiment are shown in Figure 4.5. To avoid scale dependency issues, the current scan size was chosen such that it represented a typical nominal area of contact in magnetic storage applications. Appropriate digital filtering techniques (Suh et al., 2006) were applied to the digitized data imported from AFM to obtain surface roughness parameters including rms roughness (R_q), average radius of curvature (R) and areal density of asperities (η) are listed in Table 4.1. The elastic moduli of DLC and AlTiC are taken as 139.6 GPa and 390 GPa, respectively as tabulated in Zhao et al. and Yeo et al. (Zhao et el., 2001; Yeo et al., 2008). A multilayer sample with a stiffer Ti layer on a thicker and compliant Au layer was prepared to examine a case with a stiffer layer on compliant substrate. However, since Au cannot be used as a substrate, it is determined that it should be deposited on a Si substrate. Nevertheless, at sufficiently small contact loads, the 200 nm thick Au layer can be treated as an effective substrate. A schematic showing the cross-section of the thin-layered films is shown in Figure 4.5. The elastic modulus of the Ti layer is 116 GPa and Au is 77.2 GPa. Detailed material properties and roughness parameters including critical interference (ω_c) and plasticity index (ψ) are also listed in Table 4.1.

4.3. Contact Stiffness Measurement Procedure

4.3.1 Contact Stiffness Measurement with Dynamic Contact Stiffness Tester

A typical experiment begins with the calibration of the strain gauges (MG, CEA06-062UW-350; resistance=350±0.3%) attached on the side of the lower tube spring as shown in Figure 4.1 (a). Since the contact stiffness is directly related with the load

applied, careful calibration of the strain gauges is required. Strain gauges are calibrated by putting dead weight on the bottom specimen mount and strain gauge voltage is recorded. A typical calibration result is shown in Figure 4.7. The calibration result of the strain gauge shows good linearity within the load range of interest especially less than 100 mN with a sensitivity of 0.56 mV/mN.

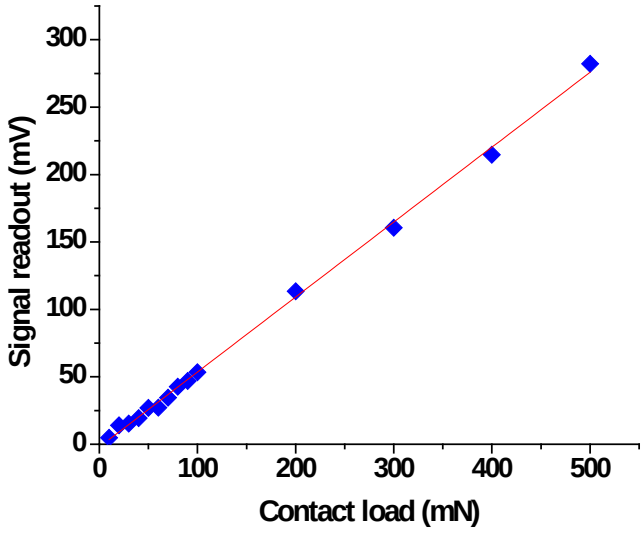

Figure 4.7 Calibration result of strain gauge measured up to a normal load of 500 mN.

After finishing the calibration of the strain gauge, the sample to be tested is attached on the bottom sample mount and sapphire glass, which is stiffer than the sample that is attached on the upper sample mount. Then the upper specimen mount, which is connected with the upper mass is lowered using the micrometer. The vertical displacement of the upper sample is controlled with the micrometer attached on the top mass and the severity of contact, or contact load is determined by the strain gauge readout

using the calibrated data obtained in the previous step. Once the two surfaces come to contact with the desired contact load, an impact is exerted on the top surface of the upper mass by dropping an impacting rod, which has a diameter of 0.8 mm and a weight of 2 mN. Finally, the motion of the system is measured with an accelerometer attached on the top surface of bottom mass.

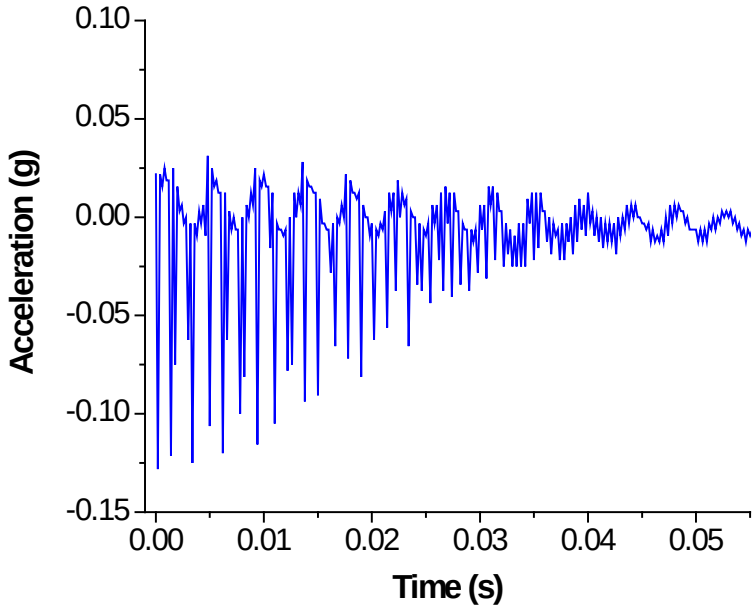

Figure 4.8 Typical accelerometer signal.

Figure 4.8 shows a typical accelerometer signal obtained from the contact stiffness measurement using the dynamic stiffness tester. Using Fast Fourier Transform (FFT) analysis, the time domain data shown in Figure 4.8 is converted into frequency domain data.

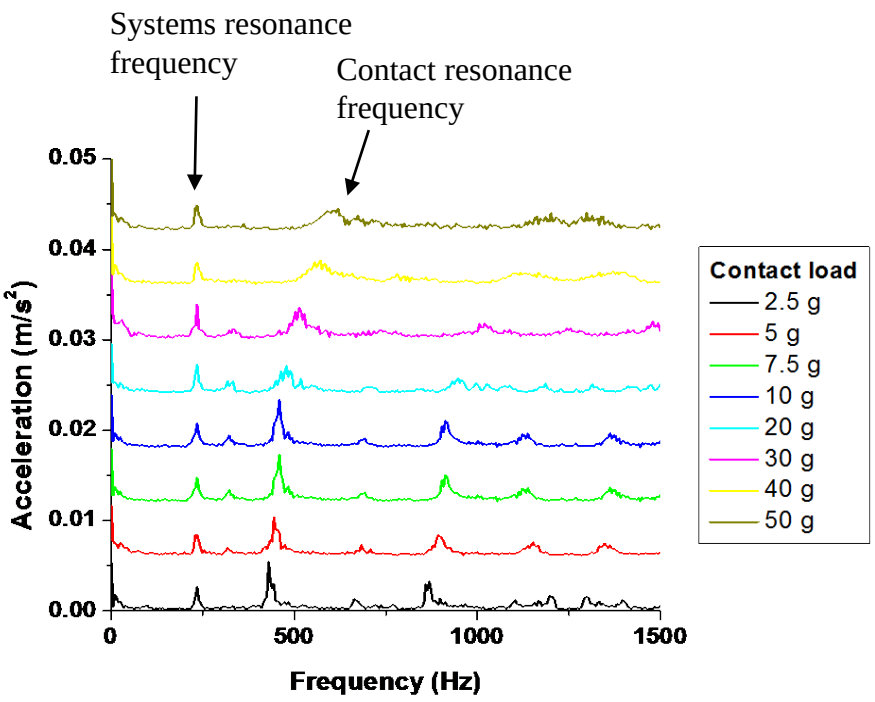

Figure 4.9 Single-shot of frequency spectra for flat rough surfaces with eight different contact loads.

Figure 4.9 shows single-shot frequency spectra for flat rough surfaces with eight different contact loads. The contact resonance frequency increases as the contact load increases. On the other hand, the system resonance frequency measured at 234 Hz is lower than the contact resonance frequency and independent to the change of contact load, as expected. The contact resonance frequencies for different samples at different contact loads are extracted following the procedure described above, and then the contact stiffness values are finally obtained using Eq. (4.4).

4.3.2 Contact Stiffness Measurement with Nanoindentation Tester

The flat tip attached to the nanoindenter is pressed into contact with the surface of the test material and then withdrawn until the contact force becomes zero. Figure 4.10 shows a typical load-displacement curve collected as the flat tip is engaged and disengaged from the specimen surface. Figure 4.11 (a)-(d) are obtained from sample 1, which has smooth DLC on AlTiC at various maximum contact forces, i.e., 1, 3, 5 and 7 mN, respectively. When examining Figure. 4.11 (a), it can be clearly observed that the loading and unloading curves are slightly different. This indicates that plastic deformation had occurred during the loading stage. There is a slight tilt of the flat punch, which causes one of its sharp edges to initially contact the sample at lower loads. As the load increases, with the help of compliant structure of the transducer, the initial tilt can be compensated and results in the surface aligning with the tip. Once the sample is aligned, we do not observe this plastic deformation effect as we progressively increase to the highest maximum contact force, as can be seen in Figure 4.11 (b)-(d). Note that this initial plastically deformed region will be extremely small as it happens at very low loads and is concentrated in a small region under one sharp edge only. Hence, we ensure that most of the asperities compressed under the whole tip will be deformed elastically.

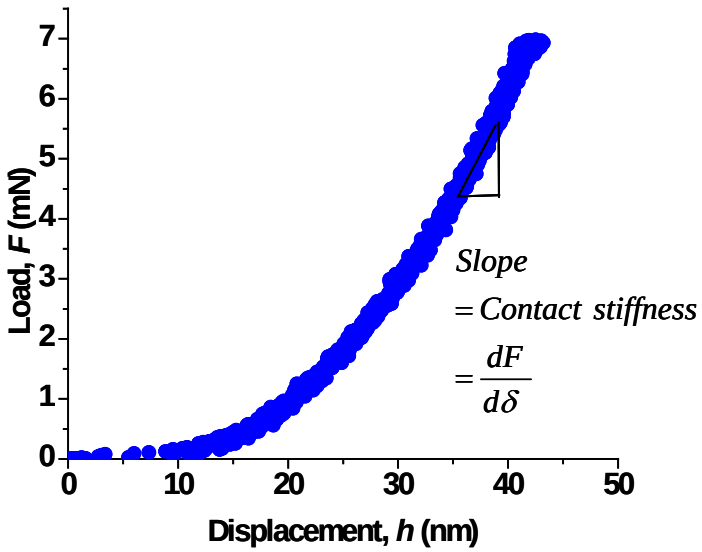

Figure 4.10 Typical load-displacement curve of flat punch indentation.

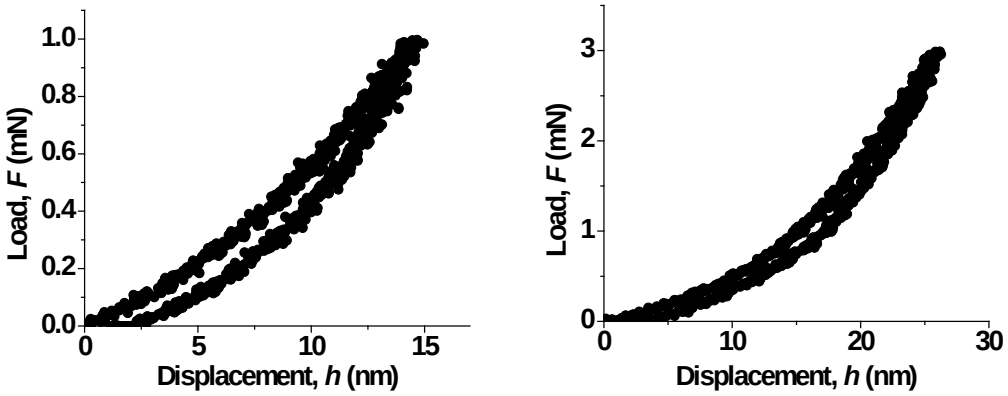

(a) (b)

Figure 4.11 (cont. on next page)

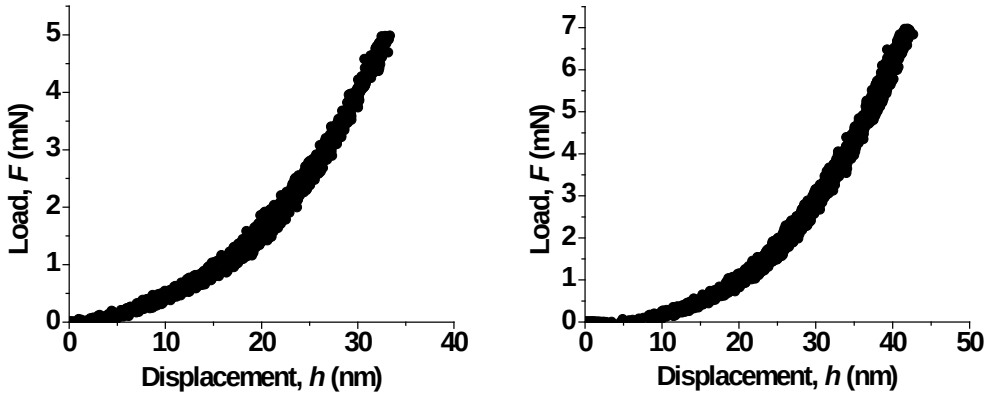

(c) (d)

Figure 4.11 Typical load-displacement curves of the flat punch indentation for sample 1 (smooth DLC on AlTiC) obtained at (a) 1 mN, (b) 3 mN, (c) 5 mN and (d) 7 mN maximum contact forces.

The contact stiffness, K_c, is defined as the increase in load per unit displacement increase. This measurement provides the contact stiffness of the combined deformation of the coating layer and the bulk substrate inclusive of the effect of roughness. It can be obtained both by the loading and unloading portion of the data. In order to avoid any initial tilt related stress concentration effects during loading, only the unloading portion of the load-unload data is used to determine K_c.

This work focuses on measurements representing elastic contact stiffness of the rough surface. Theoretically, the contact stiffness can be directly extracted from the unloading curve of single load-unload data measured with the highest maximum force. However, instead of obtaining the contact stiffness from a single unload curve, different experiments were performed by increasing the maximum contact force progressively and

the contact stiffness was obtained from each of the load-unload curves by linearly curve-fitting the top 10 % of the unloading data. Because at high loads, the sharp edges of the punch will result in stress concentration, K_c calculated from a single unload curve for lower depths will be affected by deformation of the material due to stress concentration. So, from the unloading portion of each load-displacement curve, the contact stiffness was obtained for a constant contact area using the following equation.

$$K_c = dF/dh \tag{4.5}$$

where F is the applied normal force and h is the tip displacement.

4.4. Results

4.4.1 Contact Stiffness Measurement Results with Dynamic Contact Stiffness Tester

The measured contact stiffness values, K_c, ranging from 5 mN to 500 mN for six different samples and analytical results predicted by the CEB model (in the case of sample 1) are shown in Figure 4.12. Each data point represents the average value of five experimental measurements.

Examining the experimental data, the contact stiffness values are non-linearly increasing and are directly related to the contact area. As the contact area becomes smaller (sample 1, A_n=10,000 μm^2), the contact stiffness decreases compared with the case where the nominal area has a larger nominal contact area (sample 1, A_n=40,000 μm^2) as suggested by Ono et al. (Ono et al., 1999), for example. However, when comparing with the experimental results, in the case of sample 1, with the existing theoretical contact

stiffness values analyzed with the CEB model, there exist several orders of magnitude differences. Shi et al. (Shi et al., 2008) found that contact stiffness models over-predicted the contact stiffness of actual interfaces by as much as an order of magnitude. However, two orders of magnitude difference is even harder to explain. One of the possible factors for these differences, could be micro slip at the interface during the impact (Spence, 1975). But, as a main factor, it is assumed that these differences mainly originate from the misalignment between the two surfaces (in other words the actual nominal contact area is significantly smaller that the flat area). Although, to ensure "perfect" alignment between the two surfaces, two goniometers were installed to cancel the initial tilt between the two surfaces, it seems that that the actual nominal area of contact does not match with the nominal contact area of the two samples during experiments. In Shi's case (Shi et al., 2005), he used the sample which had a normal contact area of 1.824 mm^2. On the other hand, the samples used in this experiment had specifically fabricated smaller contact areas of 0.01 and 0.04 mm^2. It is very hard to cancel the initial tilt between the two surfaces as the size of the sample becomes smaller. This can be explained considering the experimental procedure. Two samples attached on the upper and bottom sample mounts separately may involve some initial misalignment. To cancel this initial misalignment, a small adjustment was made before the two surfaces were brought to actual contact using two goniometers (based on visual inspection through the microscope installed beside the samples). The actual amount of length to be adjusted at the four corners of the squared sample becomes more sensitive as the sample becomes smaller. For example, if there is a

2 μm gap at the opposite side of the contacting edge, this gives an initial tilt of 1.15° for a 100×100 μm^2 sample. However, this angular misalignment reduces to 0.11° for a 1×1 mm^2 sample. Therefore, any small misalignment between two small samples would result in different contact stiffness values for the contact area. It seems that contact stiffness values obtained in these experiments are not dominated by the roughness of the top surface and the material properties of the substrate but by the contact condition/geometry. From Shi's previous results, it was expected that measured contact stiffness values were one order of magnitude lower than theoretical predictions. However, experimental results in Figure 4.12 show that contact stiffness values are in the order of 10^5 N/m which is still one order of magnitude lower than predicted. It is estimated that the actual contact was made at the small portion of the sample with a contact area of around 400 μm^2 in the case of sample which has a nominal contact area of 40,000 μm^2. This means that the contact only occurs at 1 % of the sample area.

Thus, further analysis on the samples used in the experiment were performed based on the experimental results using the nanoindentation tester associated with the flat-end indenter.

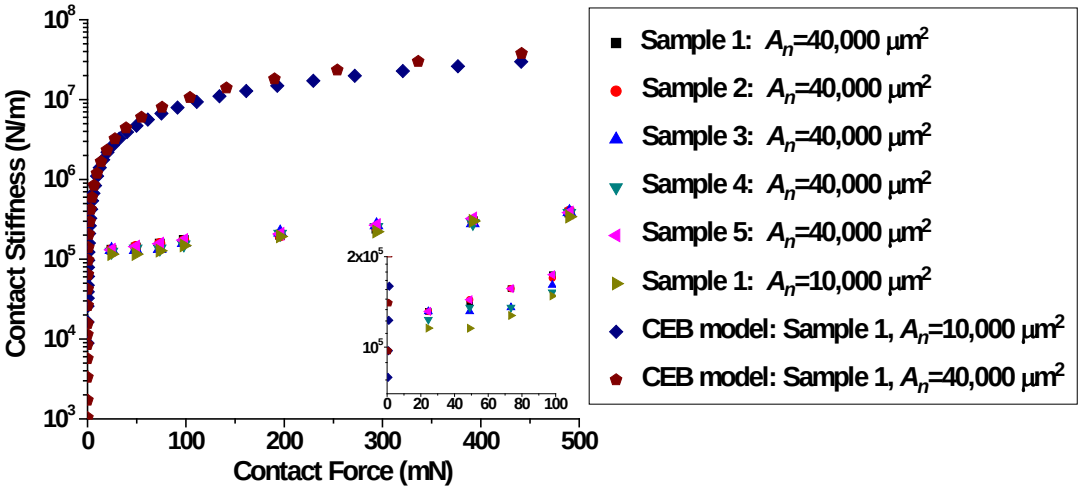

Figure 4.12 The measured contact stiffness values using the dynamic stiffness tester with a comparison of CEB contact models. The inset shows a zoomed-in plot up to 100 mN contact force.

4.4.2 Contact Stiffness Measurement Results with Nanoindentation Tester

Figure 4.13 shows the measured contact stiffness, K_c, with respect to contact force ranging from 1 mN to 8 mN for each specimen. Each data point represents the average value of five experimental measurements. These experimental results are compared with the existing rough surfaces contact models of GW, CEB, CGP and Yeo et al. using the top thin-film material properties. Since the GW, CEB and CGP models treat the rough surface made of a homogeneous material, these models were implemented by only considering the top thin-film layer for layered materials. Yeo et al.'s model provides a framework where a stiff thin-film layer is present on a compliant substrate. Thus, Yeo et al. model is used to compare with experiment results only for sample 5 where a stiffer thin film presents on a harder substrate. For cases where a compliant thin-film is present

on a stiff substrate, homogeneous material-based models should work fairly well at light contact loads.

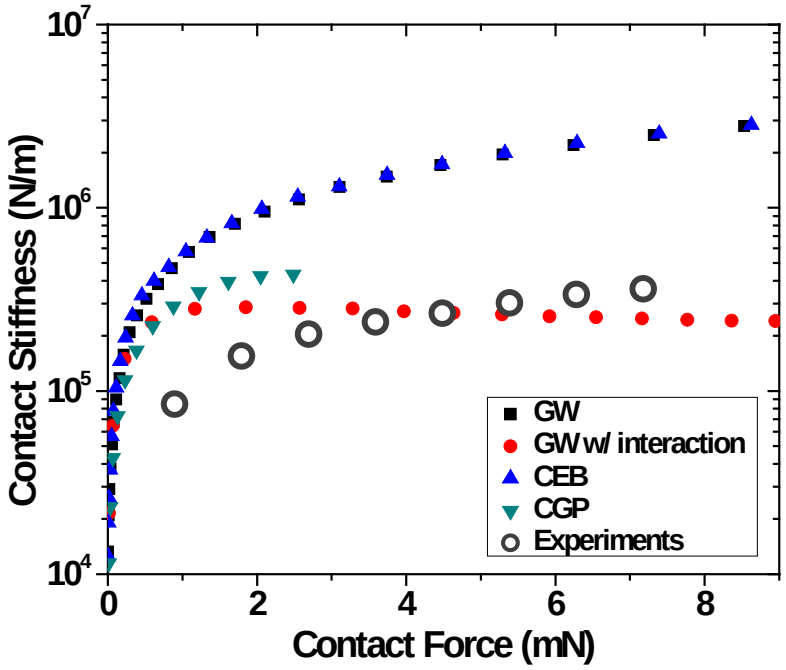

(a)

Figure 4.13 (cont. on next page)

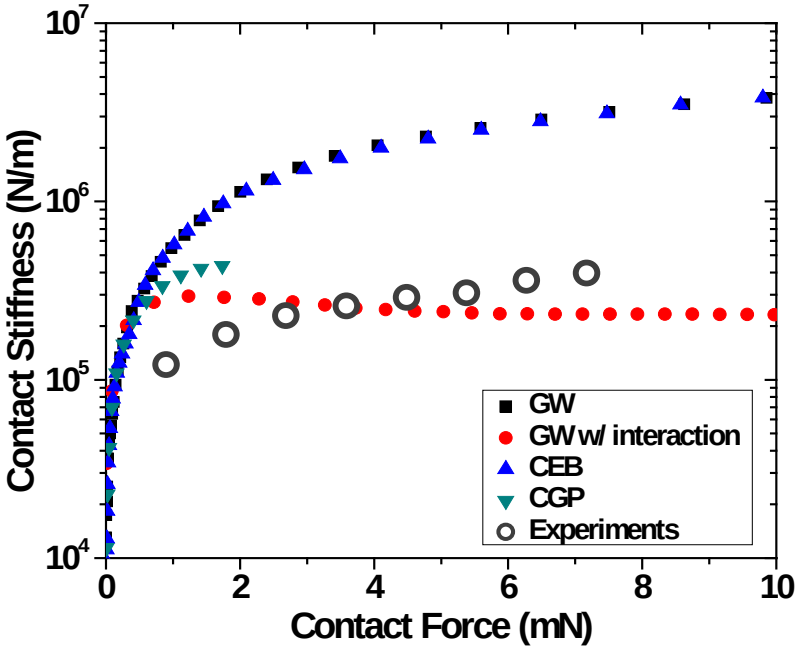

(b)

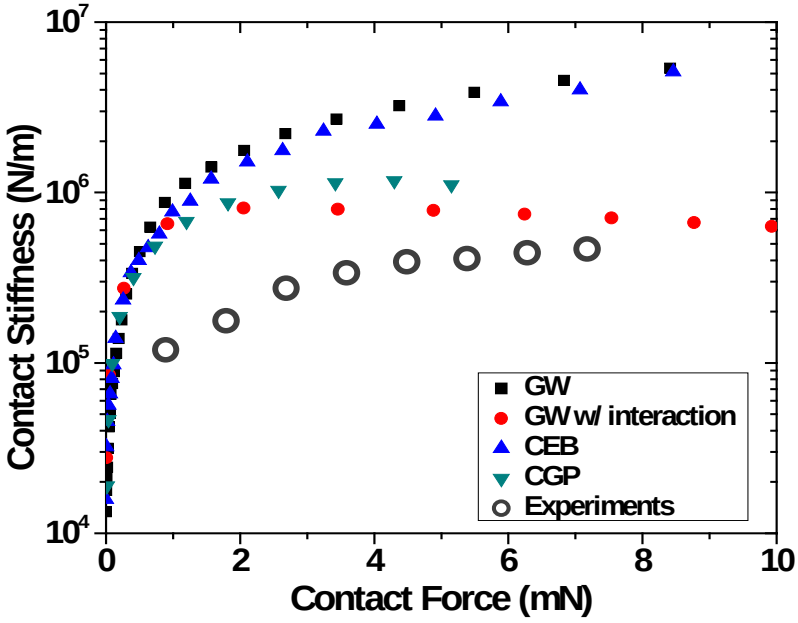

(c)

Figure 4.13 (cont. on next page)

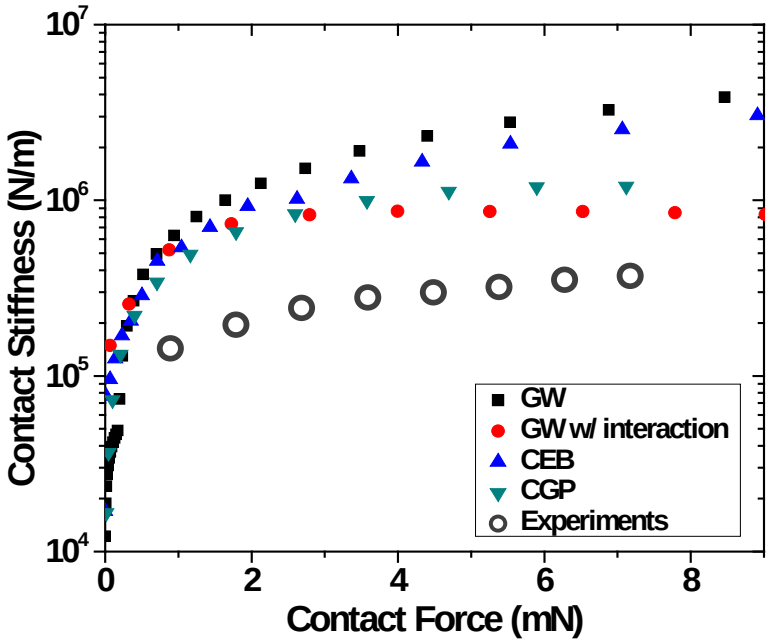

(d)

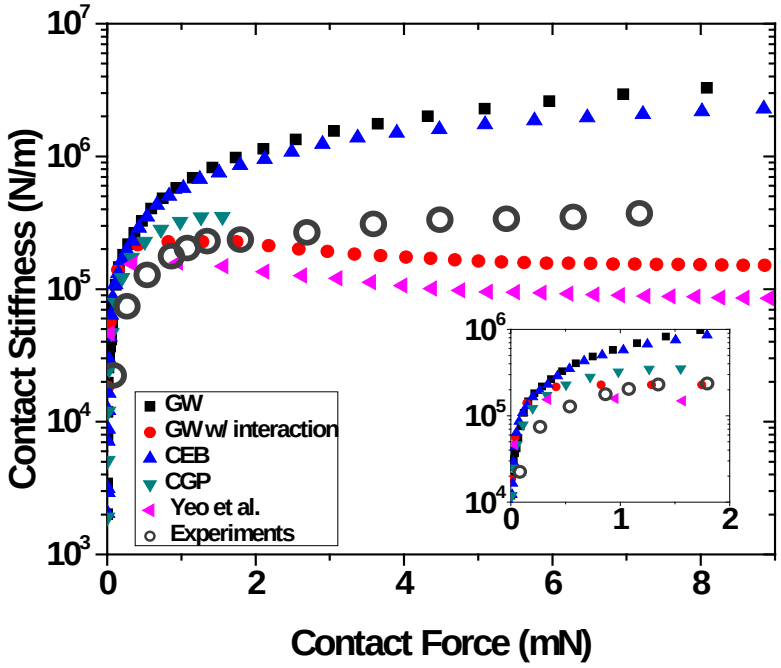

(e)

Figure 4.13 (cont. on next page)

Figure 4.13 Measured contact stiffness values vs. contact force and comparison with various contact models (a) sample 1: smooth softer layer on harder substrate, DLC on AlTiC (b) sample 2: rough softer layer on harder substrate, DLC on AlTiC (c) sample 3: smooth AlTiC (d) sample 4: rough AlTiC (e) sample 5: harder layer on softer substrate: Ti/Au.

Fig. 4.13 (a) shows the contact stiffness for sample 1 which has a compliant DLC layer present on a stiffer AlTiC substrate. The experimentally measured contact stiffness is about one order of magnitude lower than that predicted by GW and CEB models, which do not consider asperity interaction. Note that CEB model is an extension of the GW model where plastic asperity deformation is also considered. However, in this case both GW and CEB models predict the same K_c, which indicates that there is no plastic deformation occurring in the asperities. This is also confirmed with the plasticity index parameter provided by Tabor (Tabor, 1951) for these cases (shown in Table 1) indicating that indeed asperities deform predominantly elastically. To account for asperity interaction, bulk deformation of the substrate is taken into account as Iida and Ono did (Iida et al., 2003). The bulk deformation of the substrate can be obtained by the Green function for a semi-infinite elastic body. Another method getting the bulk deformation of the substrate can be determined from the solution of Hertzian pressure on a circular region of an elastic half-space (Johnson, 1985). The results obtained by the two methods are identical. In this study, the substrate deformation outside of the contact region is obtained using the Hertzian solution. When we compare the results to the of GW model with the inclusion of asperity interaction, we can see that the contact stiffness values over the whole load range are in fairly good agreement with the experiments. This shows that

asperity interaction effects are very critical. However, at light contact loads, the measured contact stiffness is somewhat lower than the one predicted by the GW with asperity interaction model. It is postulated that some of differences at the light contact force come from the initial misalignment described above, which results in slightly lower nominal contact area at light loads. According to Iida and Ono (Iida et al., 2003), the contact stiffness is proportional to the nominal contact area, thus as the initial nominal area is lower due to slight tilt, the contact stiffness from the experiments is also lower. As the tip approaches the surface, the initial minor misalignment will be relieved as the contact load is increased. At higher contact loads (above 3 mN), the measured contact stiffness values are higher than the GW model with asperity interaction, but still within the range of agreement. Note that asperity distribution-based rough surface contact models are only idealized representations of the realistic surfaces where assumptions were made to simplify the models. However, the experimental measurements clearly indicate that for extremely smooth surface contacts, asperity interaction effect is critical as can be verified from the good agreement with contact models accounting for asperity interaction. The predicted contact stiffness is extremely high when asperity interaction is not accounted as can be seen from the GW and CEB models.

Figure 4.13 (b) shows the measured contact stiffness for sample 2 which has the same thin-film structure as sample 1 but with higher roughness. The overall trend is very similar to the result of sample 1. As expected, the contact stiffness is lower than that of sample 1. A rougher surface will have a lower contact stiffness since the real area of

contact will be lower for a given interference (or displacement). This shows that the contact stiffness measurements could clearly capture the effect of roughness, even at such extremely fine scales. The experimental results are compared to the contact models in a similar fashion to the sample 1 results, namely that the GW model with asperity interaction is close to the experiments.

Figure 4.13 (c) shows the contact stiffness results for the homogeneous AlTiC material. Similar to the observations made in the earlier cases (samples 1 and 2), the contact stiffness measurements are orders of magnitude lower than the contact models which do not consider asperity interaction effects. The results are closer to the GW model with the asperity interaction effect included. The measurements have lower contact stiffness than that predicted by the GW model with asperity interactions. This can be accounted by the fact that some asperities in this sample undergo plastic deformation at a given contact force as can also be observed from the plasticity index parameter in Table 4.1. When asperity plastic deformation is involved in contact, CEB model can be used to model the contact behavior. There is a slight difference in the contact stiffness values analyzed with GW and CEB model indicating that this specimen undergoes plastic deformation at a given contact force range, i.e., 1 mN - 8 mN. This trend consistently continues as the contact force increases. This explains why the experimental measurements are lower than the GW with asperity interaction model. For a better comparison with the experiments, a rough surface contact model which accounts for plastic deformation as well as asperity interaction is needed.

Similarly, Figure 4.13 (d) shows the measured contact stiffness for sample 3, which is similar to sample 2 but with a higher roughness. In this case, we observe that the K_c difference between the GW with interaction and experiments is slightly higher than in the case of sample 3. This is because, as the roughness increases, the plasticity index also increases (Table 4.1). Thus, more number of asperities deform plastically. This causes the larger discrepancy between the elastic contact-based GW model with asperity interaction and the measurements. As noted above, an elastic/plastic model with asperity interaction is needed.

Figure 4.13 (e) shows the contact stiffness measurement results for sample 5, which was prepared to represent a case with a stiff top layer on a compliant substrate, i.e., (20 nm thick Ti on 200 nm thick Au). In this case contrary to the earlier cases, the experimental results show higher contact stiffness values than those of the GW with asperity interaction model after applying 2 mN contact force. In reality, the current sample is a multilayer sample with a structure of Ti (20 nm)-Au (200 nm)-Ti (20 nm) on a silicon substrate (elastic modulus ~ 100 GPa). Rough surface contact models dealing with multilayer materials do not exist yet. GW with asperity interaction model is applied by considering only the top Ti layer. Hence, we see the discrepancy in the results. Yeo et al. model considers the effect of a single hard layer on a compliant substrate and the effect of substrate under a stiff layer is properly captured. The contact stiffness predicted by Yeo et al. model is even lower than that of GW with interaction. This is because the substrate material used in analyzing the Yeo et al. model is Au which is very compliant

(elastic modulus of 77.2 GPa). At higher contact loads, the substrate effect actually comes from Si, which is stiffer than Au. The inset in Figure 4.13 (e) shows a comparison at lower contact loads. At extremely low loads < 1 mN, we observe the tilt related effects as discussed earlier. As load increases, the GW with interaction and Yeo et al. models compare favorably to the experiments. But beyond 2.5 mN, Si substrate dominates the contact, resulting in higher K_c measurements. For a better comparison with Yeo et al. model, a sample with a stiff and thin layer on a compliant substrate is needed. Due to sample preparation issues, only a multilayer sample could be used, but at sufficiently smaller loads, the 200 nm Au layer acts as a substrate.

The contact of extremely smooth surfaces was studied and compared to rough surface contact models. Better comparison was obtained by accounting for asperity interaction on the rough surface models. Hence, in order to analyze the contact in such cases, we need to include the asperity interaction effects. A rougher surface will result in reduced contact stiffness due to the decrease in the real contact area as has been shown from the experimental observations here. Note that for general engineering steel surfaces (rms roughness values in the 100 -1000 nm), it was shown that the contact stiffness is dominated by the roughness, and is several orders of magnitude lower than the stiffness due to the material properties (modulus) (Shi, 2005).

4.5. Summary

A difficult but needed experimental investigation was carried out using two different testers, namely, a dynamic stiffness tester and a nanoindentation tester with

nominally flat surfaces to explore the contact of extremely smooth layered surfaces used in micromechanical applications. The experimental results have been compared with several existing contact models. It was found that the contact stiffness values obtained from the dynamic stiffness tester are significantly affected by the contact condition due to the initial tilt between the two surfaces. The nanoindentation tester used with a flat-ended indenter properly captured the effect of roughness of the top surface and different material properties of the substrate. The main findings of the experiments are as follows.

1. Some differences were observed at the light contact load range because of the initial misalignment. On the basis of the conducted experiments, it was found that a better comparison was obtained by accounting for asperity interactions on the rough surface models. Hence, in order to analyze the contact in these cases, we do need to include the asperity interaction effects.

2. The contact stiffness results for a thin film material which has compliant material on a stiffer substrate are closer to those of the GW model with asperity interaction effect in the elastic regime. When some asperities in the sample undergo plastic deformation, discrepancy was observed. For a better comparison, a contact model which accounts for plastic deformation of asperity as well as asperity interaction is needed.

3. The contact stiffness results for a thin film material with a stiff top on a compliant substrate show that the Yeo et al. model agrees with the contact stiffness values obtained experimentally at extremely low loads (<1 mN). But beyond 2.5 mN, the measured contact stiffness values are closer to those of the GW with asperity interaction

model. It is suspected that this discrepancy is due to the multilayered sample used in the experiment. At lighter load, Yeo et al. model which only deals with the case where a stiff layer on a softer substrate is valid. However, at higher load, the contact behavior is more dominant by the substrate and in that case, the GW model with asperity interaction would be expected to be more appropriate.

5. Wear Modeling and Analysis of Head Overcoat on Protruded Pole Tip due to Contact with Thermal Asperities

5.1. Introduction

Due to high areal density demands in hard disk drives, the gap between head and disk surface needs to further decrease. In order to achieve high density recording up to 1 Tb/in^2, the spacing between head and disk should be maintained with 3.5 nm flying height (Gui, 2003). Direct ways of lowering the flying height of the slider were suggested by many researchers such as contact recording (Hamilton et al., 1992; Ono et al., 1999) and pseudo-contact recording (Hanchi et al., 1999). However, a direct way of lowering the flying height of the slider can cause large vibrations of the slider induced by the strong intermolecular adhesive force at the head/disk interface (HDI) and may increase the possibility of a catastrophic failure of the slider due to the contact with disk (Lee et al., 2004).

Yeack-Scranton et al. (Yeack-Scranton et al., 1990) proposed a new design of the slider, which can raise the recording head instead of lowering the flying height of the whole slider by using piezoelectrics. Suk (Suk et al., 2005) came up with a more advanced type of a slider, which can lower the flying clearance of the head above the media surface during read-write operation by writing the current induced pole tip protrusion (PTP). PTP technology has attracted significant attention since it decreased the gap between the disk and the head, and thus increased the areal density in hard disk drives. However, reduced flying height of the protruded pole tip can cause highly

localized wear due to contact with disk asperity or contaminant particles on the disk, result in thermal asperity (TA) (Li et al., 2006; Gong et al., 2005; Gupta et al., 2000). Wear at the pole tip is a factor which could lead to the degradation in recording performance (Hara et al., 2009).

Diamond-like carbon (DLC) films have been widely used as protective overcoats on magnetic media and magnetic head sliders in hard disk drives (Sourty et al., 2003; Tan et al., 2009) due to their superior properties such as high hardness and low friction (Zhou et al., 2000; Suzuki et al., 2003). Vijay et al. investigated the wear behavior of DLC coatings on magnetic recording sliders during contact start stop testing for DLC films of 9.2 nm or greater (Vijay et al., 2000). However, in order to achieve the areal density of 1 Tb/in^2, a protective layer of 2 nm or thinner is required (Ferrari et al., 2004) and Vijay et al.'s approaching method measuring wear and hardness of carbon overcoat for DLC films thinner than 2 nm would be a challenging task as they reported (Vijay et al., 2000). Song et al. (Song et al., 2006) measured the wear of the pole tip using atomic force microscopy (AFM) after identifying the location and shape of the wear with focused ion beam (FIB). They found that the wear amount was related with the maximum heater power which controls the height of the pole tip, but could not obtain consistent results with different thicknesses of DLC due to the oxidation of the pole tip.

Hence, for a better insight of the wear process between a pole tip and asperity, we need to develop a wear model for two hemispherical asperities accounting for various interferences, radius of asperity, and Young's modulus. The first analytical approach of

the stresses at the contact for two elastic spheres was done by Hertz (Johnson, 1985). Chang et al. extended Hertz's work to plastic regime beyond the elastic limit for the range of moderate contacts (Chang et al., 1987). Kogut and Etsion focused more on the evolution of elastic-plastic contact of a deformable hemisphere and a rigid flat, and found that there were three distinct stages from fully elastic to fully plastic (Kogut et al., 2002). In their works, contact analysis was done under normal contact loading rather than sliding contact conditions. Faulker and Arnell developed a three-dimensional finite element model accounting for the sliding interaction of two, elasto-plastic hemispherical asperities describing the normal and shear forces, and predicted the overall friction coefficient for rough surfaces (Faulkner et al., 2000). Podra and Andersson (PA model) attempted to simulate the wear using FEM for sphere on plane configuration. The pressure distributions were obtained by FEM and the wear depth was calculated by modifying Archard's wear equation (Podra et al., 1999). Shankar and Mayuram applied the PA model for two contacting asperities and developed the PA model further to determine the total volume of material displaced from the asperity (Shankar et al., 2008). However, both the PA and SM models depend on the wear coefficient determined experimentally to get the wear depth after the contact. A new approach was proposed by Salib et al. (Salib et al., 2009) which did not rely on an empirical wear coefficient for the tangential contact between the rigid flat and the sphere. They took the slip interfaces intersecting the sphere, and selected one among the slip interface which showed the largest maximum shear strain value within the plastic zone at sliding inception. They

considered the volume calculated above the selected slip planes and defined it as the 'potential wear' particle because actual removal of the material did not occur.

The common definition of wear defined by OECD (Williams, 2005) is 'the progressive loss of material from the operation surface of a body occurring as a result of relative motion at its surface'. However, potential wear can be directly extended to include the volume deformed plastically, because wear debris generated is directly proportional to the plastically deformed volume or the deformation of a soft material by harder asperities. This is since wear measurements are performed on displaced material which in some cases it does not include loose debris (Rigney, 1988).

In this work, we investigated the sliding contact behavior of two asperities describing the pole tip of the slider and an asperity on the disk. Contact analyses were done for various sliding intercepting conditions using FEA. The wear behavior of the pole tip was predicted by obtaining the plastically deformed zone and the deformed shape from FEA.

5.2. Finite Element Modeling

The commercial engineering software, ABAQUS, is used to analyze the sliding contact of the pole tip and asperity. The FEA model used in this study is shown in Figure 5.1. The curved area is heavily meshed and represents the protruded pole tip of the head having 0.72 μm radius and 6.98 nm height. The top of the pole tip is modeled to have fully bonded carbon overcoat (COC) (elastic modulus, E_{coc}=250 GPa, yield strength, $\sigma_{y,coc}$=8 GPa and Poisson's ratio=0.24) which has a thickness of 2 nm. The substrate

represents the write pole of the head which is typically made of NiFe (elastic modulus, E_{NiFe}=100-250 GPa, yield strength, $\sigma_{y,NiFe}$=1.7 GPa and Poisson's ratio=0.3). The material properties used in this study are summarized in Table 5.1. The top part depicted as a solid curved line in Figure 5.1 is the asperity residing on the disk surface with a radius of 1-2.5 μm and assumed to be an analytical rigid body. Sliding inception occurs as the top rigid body moves from the left side of the pole tip and finishes the sliding event on the right hand side of the pole tip with given constant interference between 0.5-4.0 nm. Friction coefficient is assumed to have a value of 0.1-0.5 during sliding contact between the two asperities. The model is constructed with 4-node bilinear plane strain quadrilateral elements and densely meshed with elements near the top notch of bottom asperity (pole tip) with approximately 0.5×0.5 nm^2 element where the sliding interception occurs. The density of elements becomes coarser as the point of interest moves away. The material used in the model is assumed to behave as an elastic-perfectly plastic and follows the von Mises yield criterion. The boundary conditions forcing the movement in all directions are assigned to the bottom line.

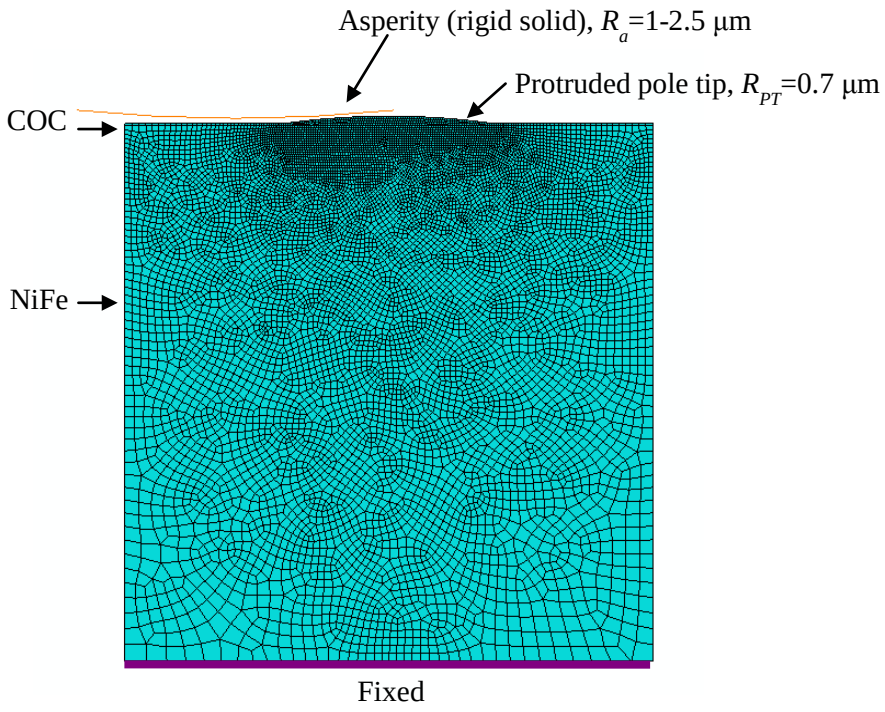

Figure 5.1 Finite element model used for sliding contact analysis of two asperities.

Table 5.1 Material properties used in the finite element model

Properties	**Elastic modulus, E (GPa)**	**Yield strength, Y_o (GPa)**	**Possion's ratio, ν**
Asperity on disk (upper asperity)	rigid solid	rigid solid	rigid solid
COC of Protruded pole tip (lower asperity)	250	8	0.24
NiFe of Protruded pole tip (lower asperity)	100-250	1.7	0.3

To validate the constructed finite element model, the results under normal loading condition are compared with Hertzian analytical results. The top COC layer is removed

for this analysis because Hertzian theory is not suitable for the layered system. Figure 5.2 shows a plot of the Hertzian contact pressure, P_{Hertz}, normalized by the effective elastic modulus, E^* versus the normalized interference distance, δ, normalized by the contact radius, $a_{contact}$. As it can be seen in Figure 5.2, both results are in good agreement in the elastic regime. Above the normalized normal approach of 0.061 (the onset of yield), FEA results start to deviate from Hertzian contact results because Hertzian theory does not account for the plastic behavior. Since FEA results show a close match with the analytical results, it could be concluded that very good agreement has been achieved between the finite element model and the analytical solutions.

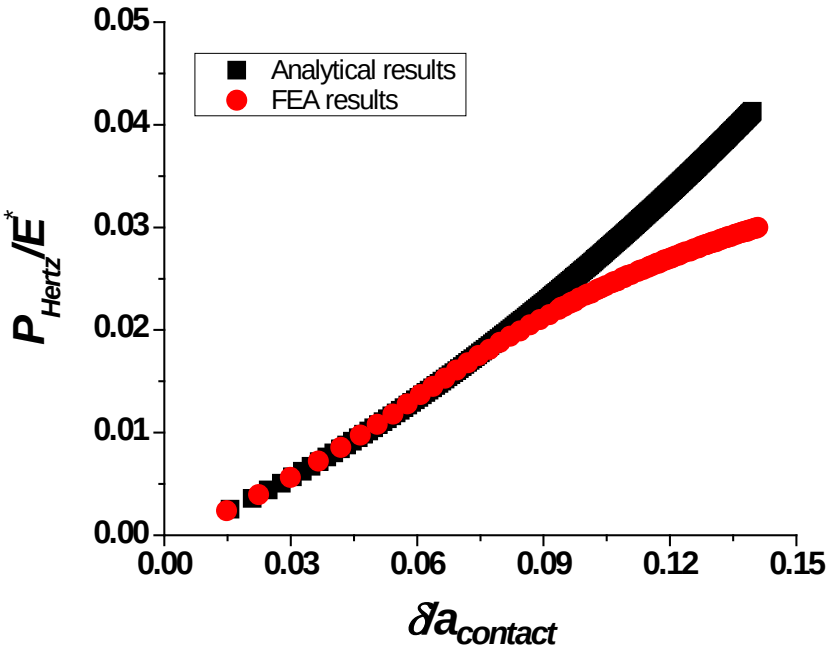

Figure 5.2 Comparison of finite element and analytical results for the normalized mean contact pressure versus normalized interference distance.

5.3. Quantifying Wear from FEA

Estimating the wear behavior of the protruded pole tip is the main purpose of this work. In order to understand the sliding contact behavior of two asperities between the pole tip and asperity, a computational approach has been utilized. FEA is often used as a tool in the analysis of contact behavior, providing contact force, contact stress, pressure, contact area, and so on. Although Slack and Sadeghi (Slack et al., 2010) used a finite element model to investigate the spall formation, application of FEA for the analysis of wear is very limited to simulate the actual removal of the material because FEA is based on continuum mechanics.

In this study, as one of the methods predicting wear behavior of the protruded pole tip was based on FEA simulations, obtaining the pressure distribution within the protruded pole tip during sliding was attempted. From this, we then get the wear depth following the concept suggested by Podra et al. (Podra et al, 1999). Podra et al. proposed the wear simulation approach by determining the pressure between a pin and a disc with linear wear law and Euler integration scheme. Shankar et al. (Shankar, 2008) applied the concept proposed by Podra et al. to the case of sliding interaction between two hemispherical asperities. For calculating the wear depth of the asperity, the simple Archard's wear law is applied. The model is written in the form

$$V = \frac{kP}{H} S \tag{5.1}$$

where V is the wear volume, k is a proportional constant providing agreement between

theory and experiment, H is the hardness of softer material, P is the normal contact load and S is the sliding distance. As the load and sliding distance vary over the sliding contact between two asperities, the wear model could be described by the differential equation as follows.

$$dV = dhdA = \frac{kpdA\Delta S}{H} \tag{5.2}$$

where h is the wear depth, p is the normal contact pressure, A is the contact area. By eliminating infinitesimal contact area and replacing k/H with K_w, Eq. (5.2) can be formulated as

$$dh = K_w p\Delta S \tag{5.3}$$

where K_w is the wear coefficient. Then finally the wear model can be formulated in the following form assuming dh/ΔS is the wear rate.

$$\frac{dh}{\Delta S} = K_w p \tag{5.4}$$

The mean contact pressure, p, in Eq. (5.4) is determined from the maximum contact pressure obtained from interaction simulation between two asperities using Hertzian relationship. By multiplying a wear coefficient of 0.2×10^{-10} experimentally calculated by Machcha et al. (Machcha et al., 1996) from a drag test of a contact recording slider, the wear rate which can be related to the wear volume is obtained.

Another way to get the wear behavior of the protruded pole tip from FEA was attempted relying on the concept of wear mechanism suggested by Rabinowicz (Colaco,

2009) and Archard (Archard, 1953).

The common definition of wear is the loss of material at the interface as a result of relative motion of two contacting surfaces. The definition of wear also includes the damage due to material displacement on a given body without generation of wear particles (Rigney, 1988; Bhushan, 2002). The mechanisms for material removal can be explained by adhesive wear model. Adhesive wear occurs in the contact area by plastic deformation when two mating asperities come to form a junction. The actual removal of material takes place when a fragment is pulled off at the junction. Removed material may be transferred to the counter surface or come off in the form of a particle. The mechanism for material displacement during the wear process can be explained with abrasive wear. Abrasive wear is used for the situation where a hard asperity sliding against a softer surface results in the formation of a groove. However, it is hard to distinguish these two cases because material displacement can be caused by adhesive wear and abrasive wear, and both two cases may induce material removal in the form of plowing and cutting.

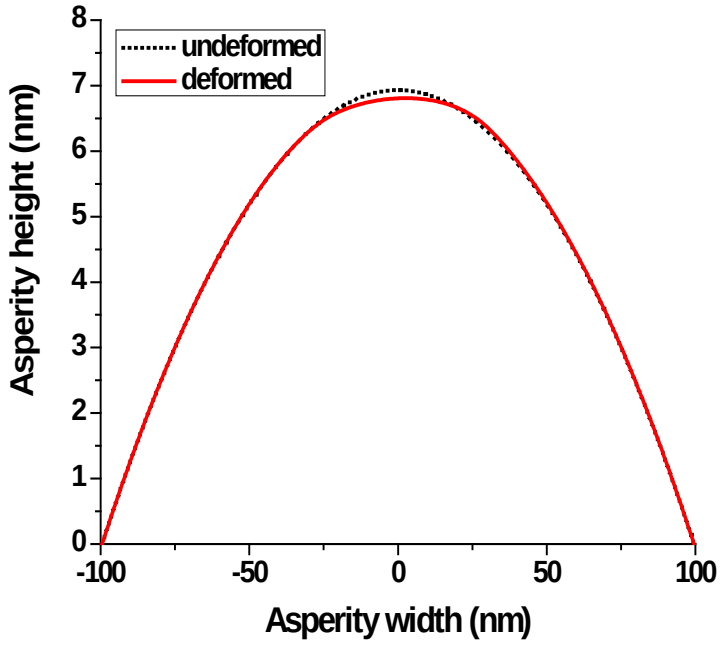

Figure 5.3 Typical shape of asperity. The undeformed shape is shown with dotted line and the deformed shape of the pole tip after sliding interception with a rigid asperity on a disk is shown with solid line.

Identifying the type of wear is not the main task in investigating the wear behavior of the pole tip. The more important question is how the wear behavior of the pole tip can be quantified. One of the factors characterizing the wear, the volume of the material displaced is measured as a form of adhesive wear which can be directly obtained from the FEA results. Another important factor in characterizing wear behavior is the plastic zone and can be quantified from FEA. According to Archard, adhesive wear or material removal is initiated from contact the area formed by plastic deformation. He assumed that a wear particle would be hemispherical having the same radius as the

contact area. Sun et al. (Sun et al., 1995) studied the plastic deformation of the layered system and found that failure of the coating system was mainly caused by the plastic flow of the substrate under the coating.

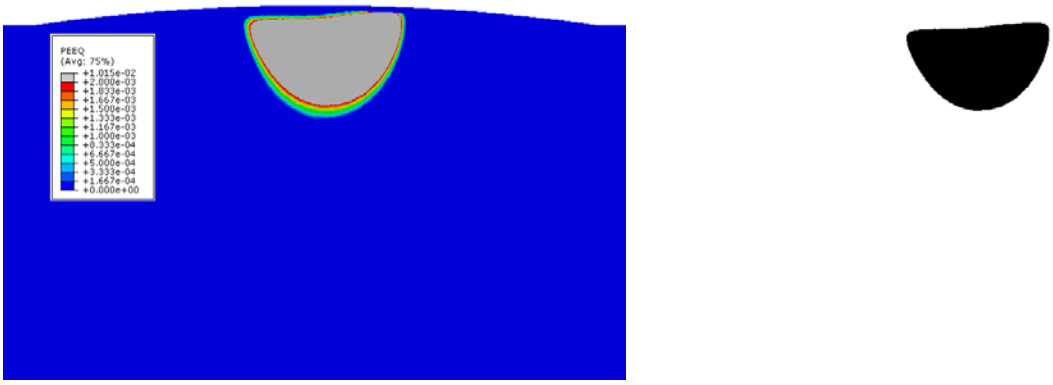

(a) (b)

Figure 5.4 Typical PEEQ contour of the pole tip showing plastically deformed area. The area shown in gray color in (a) plastically yielded from sliding contact with a disk asperity. The net area shown in (b) of plastically deformed zone is extracted from (a).

Accordingly, it is imperative to analyze the deformed shape and plastic zone induced by sliding interception so as to have a better understating of wear behavior of the protruded pole tip. To do so, a rigorous parametric study has been carried out using a two-dimensional finite element model simulating sliding contact between two asperities. The area of material displaced and the plastically deformed area is calculated separately in two ways. Figure 5.3 shows the typical shape of the pole tip (solid line) after sliding contact with the asperity on the disk. The area of material displaced is determined by subtracting the deformed shape (solid line) from the undeformed shape (dotted line). To

obtain the plastically deformed area, the equivalent plastic strain (PEEQ) contour is used. When a plastic strain exceeds the offset yield strain (0.2%), it is defined that the material is plastically deformed. Figure 5.4 (a) shows a typical PEEQ contour of the protruded pole tip obtained once the sliding interception with the asperity on disk is finished. The plastically deformed area is shown in gray color. Using image analysis, the shape of the plastically deformed area (gray color) is extracted from the PEEQ contour as shown in Figure 5.4 (b). The number of pixels in the region is counted using an image processing technique (using Matlab). The exact area is calculated by multiplying the actual area of each pixel with the number of pixels obtained from image processing.

Various aspects of sliding interaction between pole tip and asperity are analyzed by obtaining the deformed area and plastically deformed area of the pole tip using the image processing technique and summarized in the results.

5.4. Results and Discussion

5.4.1 Sliding Contact Behavior between Protruded Pole Tip and Thermal Asperity

The sliding contact behavior between the pole tip and the thermal asperity is analyzed after the first encounter and before the wear rate is obtained. A parametric study has been performed for various parameters affecting the sliding contact such as different levels of interference and friction coefficient values.

Figure 5.5 shows a plot of the normal and shear forces acting on the top surface of the upper asperity with change of interference values (R_{TA}=1.5 μm, E_{NiFe}=200 GPa and

μ=0.1). The overall trend of the 5 curves shows a similar behavior with the change of interference. As the sliding distance increases, both the shear force and normal forces increase after the initial contact. After reaching the maximum, the normal force steadily decreases to zero, and the shear force goes down below zero and then comes back to zero. The degree of maximum shear and normal forces are directly related with the severity of interference, as expected. The maximum normal force occurs slightly before the maximum pole height, i.e., a sliding distance of 150 nm. This is because the material displaced is free to move laterally and this observation is in good agreement with the findings of Faulkner et al. (Faulkner et al., 2000).

As the friction coefficient increases at the interface, the shear force grows rapidly and eventually reaches a higher maximum shear force while the normal force does not change, as shown in Figure 5.6.

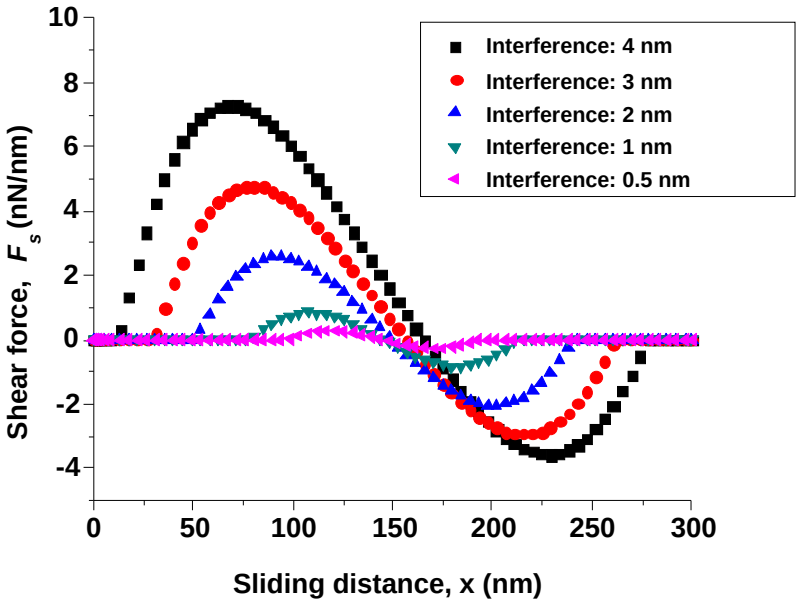

(a)

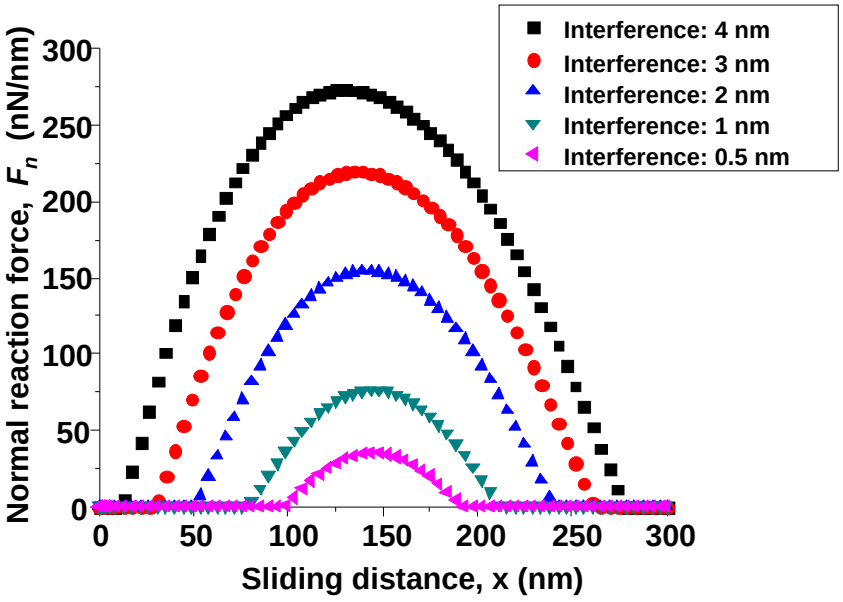

(b)

Figure 5.5 (a) Shear force and (b) normal reaction force plotted as a function of sliding distance of the upper asperity (thermal asperity) for various interferences from 0.5 to 4 nm.

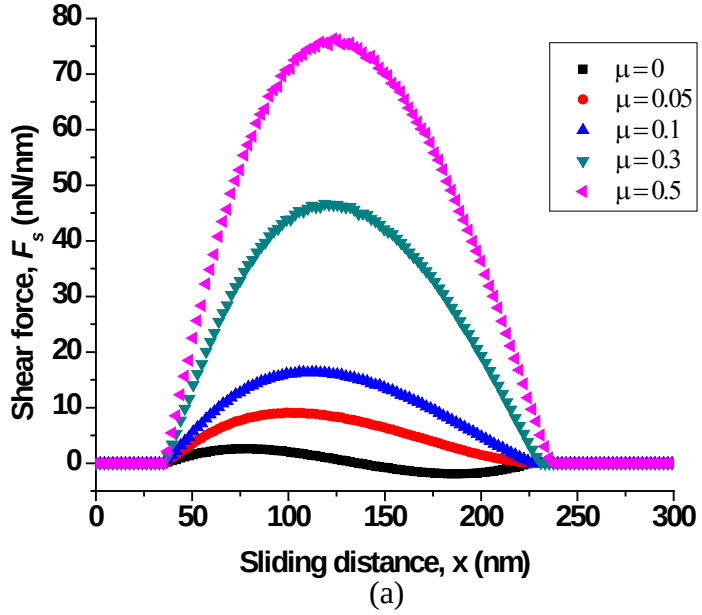

(a)

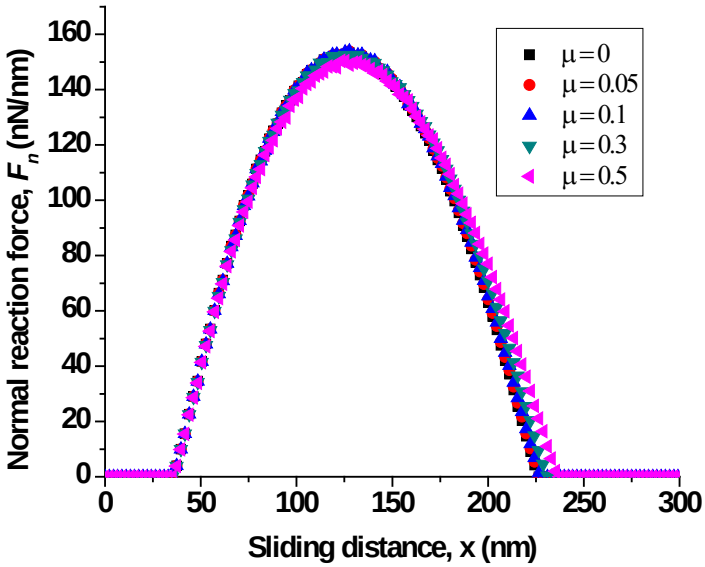

(b)

Figure 5.6 (a) Shear force and (b) normal reaction force plotted as a function of sliding distance of the upper asperity (thermal asperity) for various friction coefficient values from 0.0 to 0.5.

5.4.2 Wear Rate of Protruded Pole Tip

Obtaining the wear rate at the protruded pole tip starts by getting the maximum contact pressure, p_0, at the interface as shown in Figure 5.7 (a). The mean contact pressure, p_m, is calculated using the Hertzian equation ($p_m=(\pi/4)\times p_0$). The mean contact pressure is plotted as a function of sliding distance for various contact interferences with a thermal asperity radius of 1.5 μm, a Young's modulus of the substrate of 200 GPa and a friction coefficient of 0.1. The mean contact pressure starts to increase after the initial contact, and reaches to the maximum point right before the center of the two asperities lines up vertically, i.e., at the sliding distance of 150 nm for the light contact less than 1 nm. For severe contact of more than 2 nm, the mean contact pressure increases to a certain point and decreases before it reaches a maximum interference and then increases again with further sliding distance. Then it falls suddenly but the mean contact pressure is not reduced to zero after finishing sliding because there is residual stress remaining in the pole tip. The reason why the maximum mean pressure does not occur at the maximum interference/overlap can be explained by the shear force analysis discussed earlier. The material displaced in front of the thermal asperity (upper asperity in the FEA model) works as a constraint in the direction of sliding so that the maximum mean contact pressure does not occur when the two axis of the two asperities are lined up.

The wear rate is calculated using Eq. (5.4) from the mean contact pressure distribution and assuming a wear coefficient of 0.2×10^{-10} (which was experimentally obtained by Machcha et al. (Machcha et al., 1996)), and plotted in Figure 5.7 (b). The

progressive increase is observed from the wear depth plot as expected because the wear depth is obtained by integrating the incremental changes assuming that a linear wear law (Archard model) is valid. If the wear depth curves are analyzed further, it can be seen that the wear depth curves have stiffer slopes before the two asperities cross over, and become flatten. This means that wear mainly occurs in the front side of the asperity during sliding contact. The actual amount of wear depth with 4 nm interference is 10 nm, which is unrealistically high. The wear depth shown in Figure 5.7 (b) relies on the wear coefficient taken from Machcha et al.'s work which results in high wear depth. To obtain a lower wear value, one needs to use a reliable wear coefficient value describing the wear behavior between the protruded pole tip and thermal asperity.

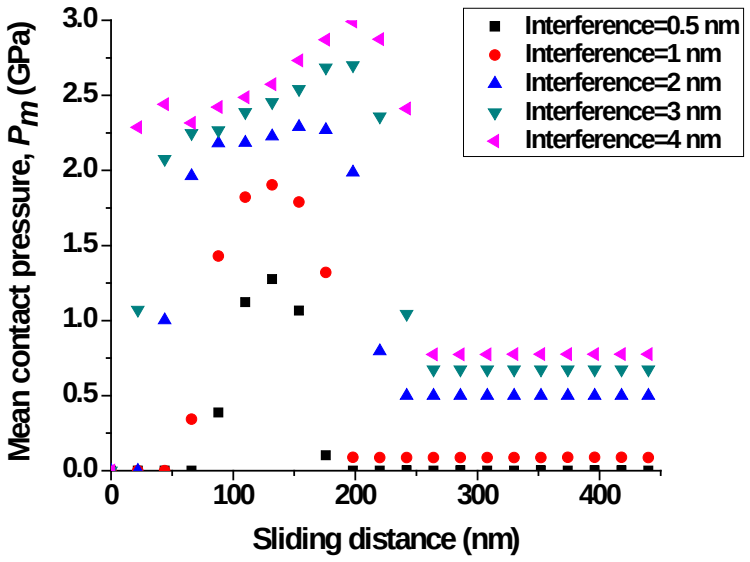

(a)

Figure 5.7 (cont. on next page)

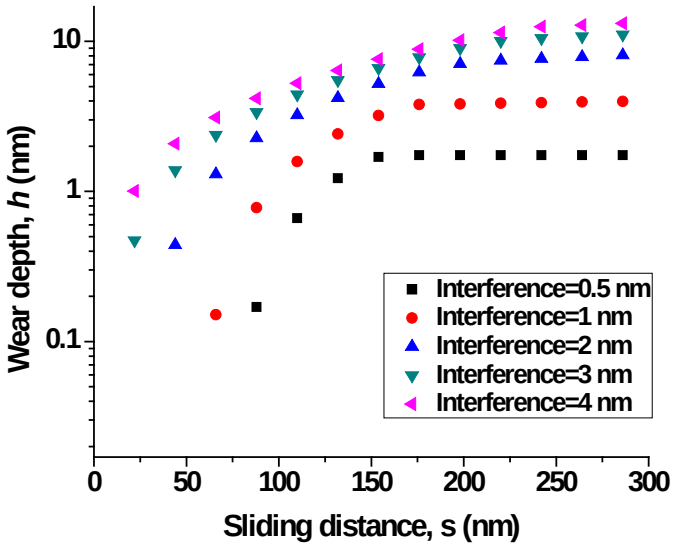

(b)

Figure 5.7 (a) mean contact pressure and (b) wear depth plotted as a function of sliding distance of the upper asperity (thermal asperity) for various interference values.

5.4.3 Wear Area of Yielded Substrate and Deformed Asperity

Figure 5.8 shows typical PEEQ contours obtained from a normal and sliding contact event. The maximum displacement given in this analysis is 1.54 nm. The dimensionless normal load obtained between the protruded pole tip (R_{PT}=1.5 μm) and asperity (R_a=1.5 μm) for 1.54 nm displacement is 2 (Eq. (5.6)).

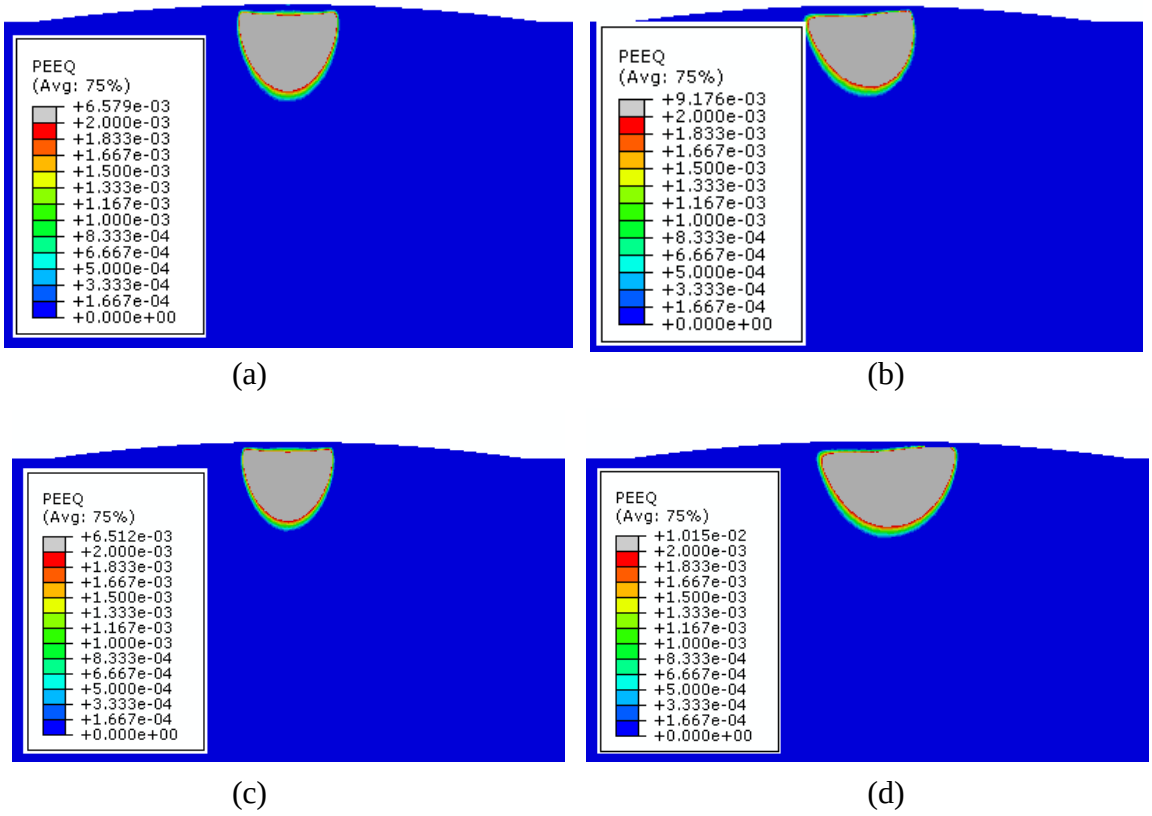

Figure 5.8 PEEQ contour plots of the protruded pole tip under normal contact condition ((a) and (c)) and sliding contact condition ((b) and (d)). The protruded pole tip is uncoated for (a) and (b), and coated with a 2 nm thick COC for (c) and (d).

The plastically deformed area which exceeds 0.2% strain is represented in gray color. Figures 5.8 (a) and (b) are obtained with a homogeneous NiFe and (c) and (d) from a layered system coated with a 2 nm COC. As seen in Figure 5.8, the plastically deformed area depends on the contact condition (normal or sliding) and the existence of the coating layer. When we compare Figure 5.8 (a) and (c), it is obvious that the substrate deforms less when it is protected with COC. For the same interference, the substrate of the layered system (Figure 5.8 (d)) deforms much more, which results in a larger

deformed area than homogeneous material (Figure 5.8 (b)) with sliding contact. When we analyzed the stress field for the two cases (normal and sliding), we were able to find that when the material underwent sliding contact, the stress field was developed at a larger area than in the normal contact case which results in a larger deformed area. This trend is maintained for the layered system, with a larger deformed area is produced for the layered system. This is due to the fact that when there is a stiffer material on a softer substrate, the substrate reaches the onset of yielding faster than in the case of homogeneous material because the highly distributed stress field along the coating layer is released through the fully bonded substrate which results in larger plastic deformation. A detailed description of the stress field is not the main scope of this work, so the plastically deformed area along with the area of material displaced of the layered system developed from sliding contact is normalized with the critical normal load obtained from the homogeneous material to clearly compare the difference of the two different modes of contact behavior.

After conducting a series of simulations for various interference values (0.5, 0.6, 0.7, 0.8, 0.9 and1 nm) between the two asperities, and different radii of asperity values (1, 1.5, 2 and 2.5 μm) and elastic moduli (100, 150, 200 and 250 GPa) with friction coefficient of 0.1, the area of material displaced and plastically deformed area were obtained. Then, the deformed area of asperity and plastically deformed area in the substrate obtained from various cases were normalized by the area of semicircle of the protruded pole tip in a similar manner as Salib et al. (Salib et al., 2008). The

dimensionless wear area is expressed in the following form.

$$V^* = \frac{V_w}{V_c} \tag{5.5}$$

where V_w is the wear area and V_c ($=\pi R_{PT}^2/2$) is the area of the semicircle of the protruded pole tip.

The numerically calculated dimensionless wear area for the deformed asperity, V_a^* and plastically deformed area, V_s^* are plotted separately in Figure 5.10 as a function of dimensionless normal load. The dimensionless normal load is calculated by dividing the maximum force applied during sliding contact (obtained directly from FEA) with the critical normal load. The critical normal load for cylindrical Hertzian contact is given by Green (Green, 2005). As a result, we have the dimensionless normal load in the following form:

$$P^* = \frac{P}{L_c} = \frac{\pi R (CY_o)^2}{E'} \tag{5.6}$$

where P is the normal load applied, R is the combined radius of the two asperities, E' is the combined modulus of elasticity of the two asperities, Y_o is the yield strength of the pole tip, and L_c is the critical normal load at plastic yield inception under full stick contact condition. It is derived from the maximum contact pressure equation for two cylinders with the aid of a curve fitted parabolic equation. C is a function of the Poisson's ratio expressed in the following form (Green, 2005).

$$C=1.164+2.975\nu-2.906\nu^2 \quad (\nu>0.1938) \tag{5.7}$$

The dimensionless wear area of the deformed asperity and plastically deformed area are not dependent on the change of radius of asperities with a constant value of elastic modulus (250 GPa in this case) of the substrate but directly proportional to the contact load (which changes with a given interference between two asperities as shown in Figure 5.9).

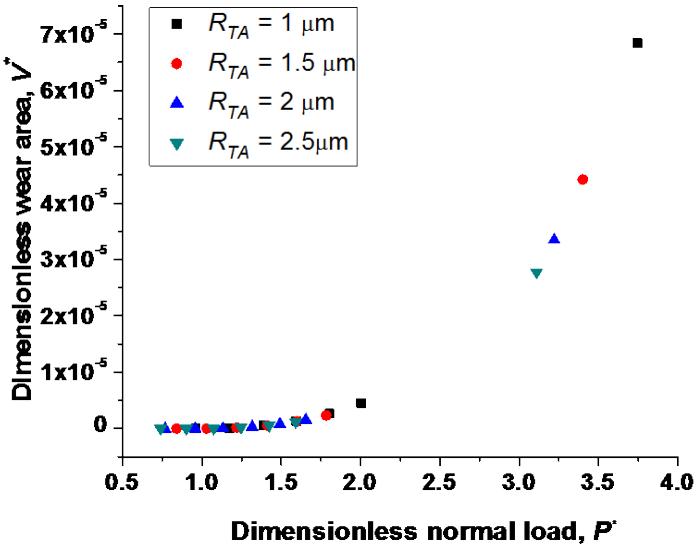

(a)

Figure 5.9 (cont. on next page)

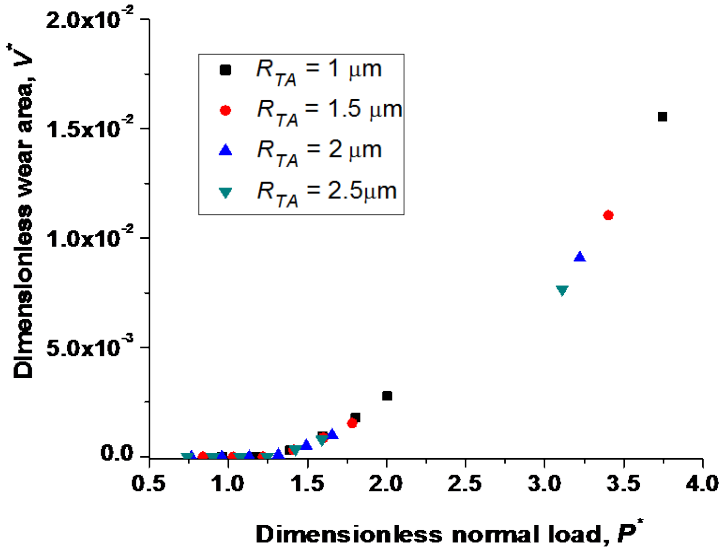

(b)

Figure 5.9 Dimensionless (a) deformed area and (b) substrate plastically deformed area (potential wear area) for different sphere radii with a constant elastic modulus of 250 GPa for the substrate.

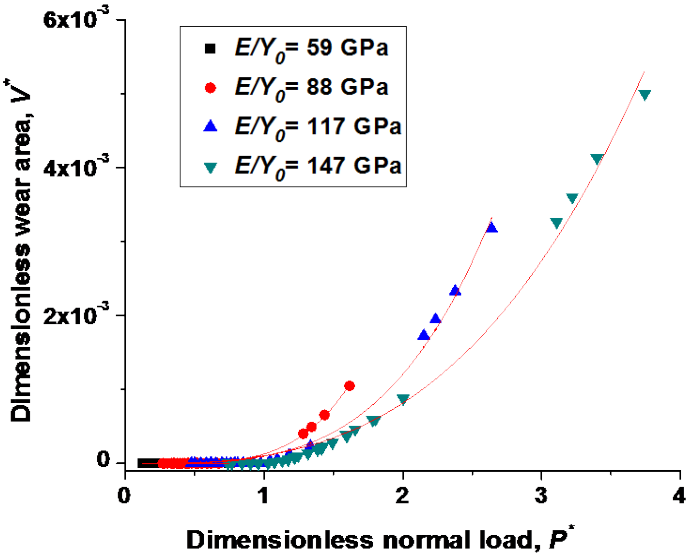

(a)

Figure 5.10 (cont. on next page)

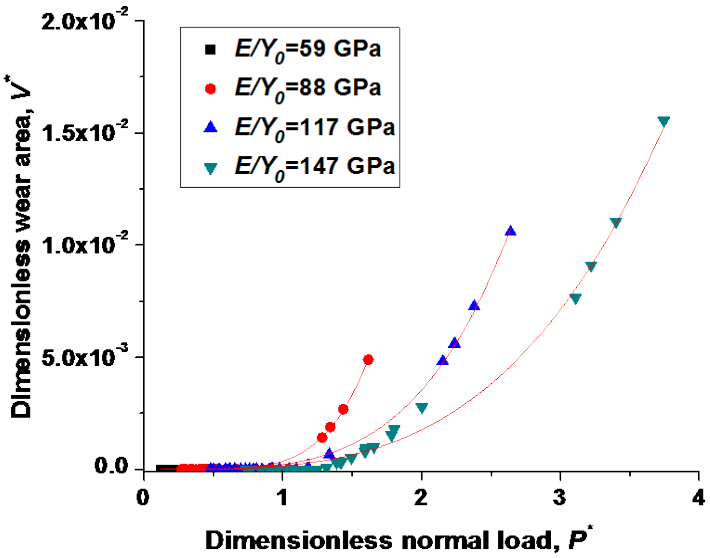

(b)

Figure 5.10 Dimensionless (a) deformed area and (b) substrate yielded area (potential wear area) versus dimensionless normal load, P^*, for different values of E/Y_0.

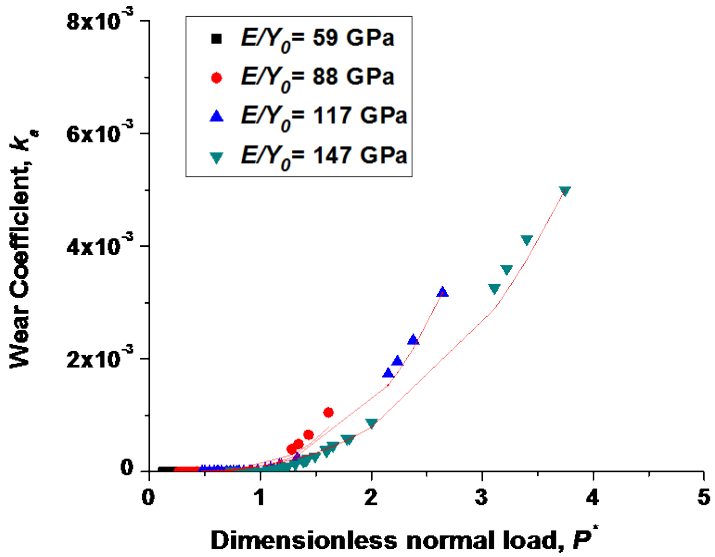

(a)

Figure 5.11 (cont. on next page)

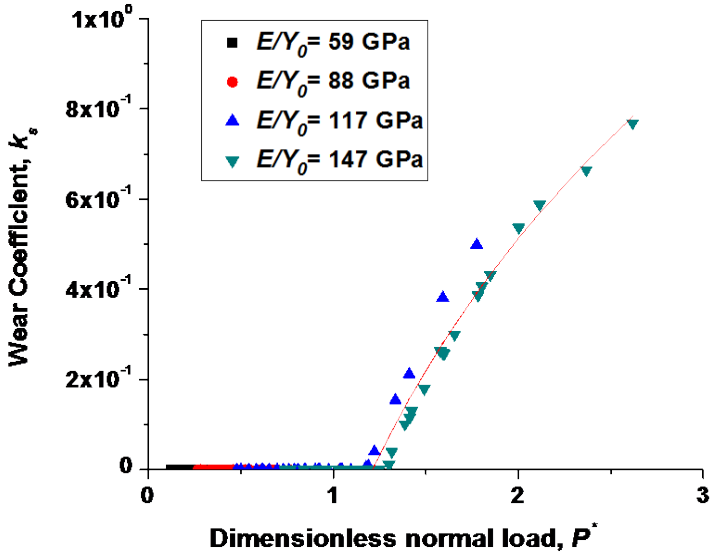

(b)

Figure 5.11 Wear coefficient of (a) deformed area and (b) substrate yielded area (potential wear area) versus dimensionless normal load, P^*, for different values of E/Y_0

Further investigation was carried out with different elastic moduli of the substrate (100, 150 and 200 GPa) and the results are plotted in Figure 5.11 together with the result represented in Figure 5.10. It was found that the wear behavior of both asperity and substrate were directly related with the change of elastic modulus. It seems that a stiffer substrate is beneficial at a given applied load as the deformed area of asperity and plastically deformed areas of substrate become smaller with increased elastic modulus of the substrate, and the initiation of plastic deformation is delayed up to 1.25 of dimensionless normal load when the elastic modulus of substrate increases up to 250 GPa (E/Y_o=147). However, this result can be interpreted differently for analyzing the sliding

contact of the protruded pole tip in hard disk drives. In most applications, the severity of contact is determined by the normal contact force between two contacting bodies. In consideration of normal operating conditions of a flying slider of a hard disk drive, the severity of sliding contact asperity is determined by the height of the asperity on the disk which changes the degree of interference. It is observed that the highest value of red dots in Figure 5.11 (a) represents the case when the substrate has an elastic modulus of 150 GPa at 1 nm interference. In this case it shows a dimensionless wear area of 1.05×10^{-3} while the highest value of green inverted triangle represents the case when the elastic modulus of the substrate is 250 GPa, and it shows a larger dimensionless wear area (5.0×10^{-3}) at the same interference (1 nm). From the above analysis, it can be deduced that a stiffer substrate is not preferable for a hard disk application to prevent wear against the sliding contact between the protruded pole tip and asperity. This does not necessarily mean that a softer substrate is always preferable for any contact behavior. From the analysis of normal contact behavior of a disk in hard disk drives done by Yu et al. (Yu et al., 2008), a stiffer disk is beneficial to reduce the damage from impact induced contact.

The wear behavior shown in Figure 5.11 is curve-fitted with the following empirical function, suggested by Salib et al. (Salib et al., 2008).

$$V^* = \frac{V_w}{V_s} = \gamma (P^*)^{\lambda} \tag{5.8}$$

where λ and γ are a function of E/Y_0, and expressed in the following form:

$$\lambda_a = 1.945\times10^{-4}\exp(-2.428\times10^{-3}(\frac{E}{Y_0}))^2 \tag{5.9}$$

$$\gamma_a = 101.3\left(\frac{E}{Y_0}\right)^{-0.7024} \tag{5.10}$$

$$\lambda_s = 1.716\times10^{-4}\exp\left(-1.545\times10^{-3}\left(\frac{E}{Y_0}\right)\right)^2 \tag{5.11}$$

$$\gamma_s = 261.2\left(\frac{E}{Y_0}\right)^{-0.8728} \tag{5.12}$$

where subscripts, *a* and *s* in λ and γ denote asperity and substrate, respectively.

Next, a simple wear model accounting for sliding contact behavior is attempted based on Archard and Rabinowicz models. Archard (Archard, 1953) proposed a well-known equation for adhesive wear in the following form.

$$V = k_{ab}\frac{P}{H}s \tag{5.13}$$

where V is the wear volume worn away, k_{ab} is the abrasive wear coefficient depending on material properties, P is the normal load, H is the hardness of the worn surface material and s is the sliding distance. Rabinowicz (Colaco, 2009) derived the following quantitative expression for abrasive wear μm

$$V = \frac{\pi P}{\tan\theta H}s \tag{5.14}$$

where $\tan\theta$ is the attack angle of the abrasive material. Except the term $\pi/\tan\theta$ in Eq. (5.14), Eq. (5.13) and (5.14) are identical. Therefore, the equations for abrasive wear and adhesive wear can be rewritten in a simplest form.

$$V = k\frac{P}{H}s \tag{5.15}$$

where k is the wear coefficient.

By inserting the dimensionless normal load expressed in Eq. (5.6) to Eq. (5.15), the dimensionless wear area for a two dimensional model accounting for sliding contact can be obtained in a similar manner as Salib et al. (Salib, 2008) did for a three dimensional model. Additionally, H is replaced by $2.8Y_o$ and the distance s is replaced by the distance, d_s, obtained at the sliding inception, and we have the following Archard-type wear model

$$V^* = \frac{V_w}{V_s} = k\frac{P^* L_c}{1.4\pi R^2 Y_0} d_s \tag{5.16}$$

The wear coefficients, k_a for the deformed asperity and k_s for the plastically deformed substrate are obtained separately by equating Eq. (5.8) and Eq. (5.16) and are plotted in Figure 5.11. As can be seen from Figure 5.11, the wear coefficients obtained in this analysis are not constant. To formulate the wear coefficient, curve fitting is performed and the best curved fitted functions for wear coefficient obtained are as follows.

$$k_a = (-7.16\times10^{-7}\times(\frac{E}{Y_0}) + 2.13\times10^{-7})(P^*)^{(-0.01559\times(\frac{E}{Y0})+5.257)} \tag{5.17}$$

$$k_s = \begin{Bmatrix} -21.29(P^*)^{-0.04912} + 21.09 & @ \ P^* \geq 1.22 \\ 0 & @ \ 0 < P^* < 1.22 \end{Bmatrix} \tag{5.18}$$

It is shown in Figure 5.11 that the maximum wear coefficient values obtained from deformed asperity and plastically deformed area are 5×10^{-3} and 0.76, respectively, which are significantly larger than the typical wear coefficient of 6×10^{-6} determined

experimentally from aggressive HDI conditions (Bhushan, 2002). The theoretical wear coefficient obtained by Salib (Salib et al., 2008) is in the range of 0.062-0.088. Considering the fact that Salib's result is obtained by assuming that wear occurs along the slip interface within the plastic zone, it is reasonable that the wear coefficient obtained from plastically deformed area is larger. The wear coefficient obtained in this study assumes that wear area is equal to the material displaced and is somewhat smaller than that of Salib's result. Although two different wear coefficient values obtained in this study are larger than the actual wear coefficient obtained experimentally, it is believed that estimating the wear coefficient from sliding contact of the layered system is beneficial in predicting the wear behavior of the protruded pole tip and asperity. Such results could be used to also study the effect of the different design parameters.

5.5. Summary

A new finite element model was developed to simulate the sliding interaction between the protruded pole tip and a rigid asperity on the disk surface. The wear depth was obtained following a method suggested by Shankar where it uses a wear coefficient value obtained experimentally. The obtained value of wear depth was unrealistically high. Another approach that uses deformed area of asperity and plastically deformed area of substrate was proposed. The deformed area of the elastic-perfectly plastic asperity representing the pole tip and plastically deformed area under the asperity which could be assumed that it will generated a wear particle during the contact event was obtained. Based on the simulation results, it was found that the wear behavior of the layered system

under sling contact behavior was mainly dependent on the contact force and elastic modulus of the substrate. These results were then incorporated into an Archard-type wear model and a wear coefficient model was obtained. The wear coefficient values obtained from this study are much higher than typical experimental wear coefficient values because the wear area is estimated from the deformed area of the asperity and the plastically deformed area. These calculations are for a potential wear and do not involve actual removal of material.

6. Synthesis and Tribological Behavior of Hafnium Diboride Coatings

6.1. Introduction

Thin hard coatings are widely applied to a variety of surfaces to increase the lifetime of engineering components and to make a device more efficient by reducing or controlling friction and wear (Malzbender et al., 2002; Holmberg et al., 1994). The development of new coating materials which provide new tribological characteristics make it possible to improve the performance of lots of applications such as microelectromechanical systems (MEMS), hard disk drives, compressors, cutting tools, forming tools and so on (Chandross et al., 2005; Voevodin et al., 1997; Goglia et al., 2001; Jhi et al., 1999; Holing et al., 2005; Solzak et al., 2006; Solzak et al., 2010).

The performance of products to which the coatings are applied relies on the material properties of the coatings, which are not necessarily confined to mechanical properties. It could be chemical, thermal, electronic, magnetic or optical properties that influence the performance of these products.

Hard coatings widely used in the 1980's and 1990's are usually based on nitrides and carbides of the transition metal elements such as TiN or CrN. In recent years, metastable phases like $Al_xTi_{1-x}N$ and $Al_xCr_{1-x}N$ have gained large success replacing the simple nitrides (Mitterer, 2008). However, the high demands on hard coatings still require advanced tribological coatings, e.g., engine components operating under hot corrosive conditions and aerospace applications which operate under near vacuum

conditions.

More recently, it has been found that a metallic-ceramic material, hafnium diboride (HfB_2), offers attractive properties for microelectronic and hard coating applications. It has a melting temperature of 3250 °C, a bulk hardness of 29 GPa and a bulk resistivity of 15 μΩcm (Castaing et al., 1972; Kieffer et al., 1963). This attractive material has not gained much attention and not led to a widespread use in technological applications because of the difficulty in obtaining stoichiometric thin films (Mitterer, 1997).

To use hafnium diborides as tribological coatings, it should be deposited on relevant substrate as a form of thin film. Recently, Jayaraman et al. have successfully deposited high quality, stoichiometric thin films of HfB_2 by chemical vapor deposition (CVD) using a single precursor at low temperature (Jayaraman et al., 2005).

Tribological behavior of thin films coated on substrate is different from those of the bulk. It should be considered the effect of substrate which plays a role in the friction and wear performance. Chatterjee et al. have studied the nanoscale friction and nano/macroscale wear response of hafnium diboride thin films as well as the property measurements such as hardness, elastic modulus and yield strength. They found that annealed HfB_2 deposited on Si (001) has a hardness of 43 GPa and a modulus of 473 GPa. It is also found that the HfB_2 thin films show a favorably low nanofriction behavior with an averaged friction coefficient less than 0.1 and excellent wear resistance (using nanoscratch tests). From macroscale pin-on-disk tests of Chatterjee, although they didn't

directly report any wear coefficient values, they observed that the HfB_2 coating provides surprising high wear resistance. However, sudden delamination was observed from the as-deposited coating and resulted in the exposure of substrate (Chatterjee et al., 2006; Chatterjee et al., 2008; Chatterjee et al., 2010). This type of behavior is one of the most common failure mechanisms in hard coatings and plays a critical role in the performance of many tribological systems (Konca et al., 2005; Berger et al., 2002, Berger et al., 2002, Heinze, 1998). For good tribological performance, it is also required to have good adhesion and shear strength at the interface between coating layer and substrate. So, it is important to understand the role of adhesion between coating and substrate in improving and developing new hard coating materials. Many tribologists have investigated the tribological behavior of layered surfaces in contact, providing a theoretical background for analyzing the layered surfaces (Holmberg et al., 1998; Holmberg et al., 2000; Imbeni et al., 2001; Polonsky et al., 2000; Luo et al., 2000; Harris et al., 1997). However, full understanding of layered surfaces has not been done especially as it involves delamination underneath the coating layer.

In this study, nanoindentation and pin-on-disk tests were performed to characterize the material properties such as hardness, modulus and friction efficient, which affect the tribological performance of the coatings. In the next step, adhesion tests were conducted to evaluate the adhesion strength at the interface between film and substrate using a nano/microscratch testing method. Based on the measurement results, further analysis was performed using a finite element analysis to characterize the intrinsic

effect of adhesion strength at the interface.

6.2. Experimental Procedure

6.2.1 Film Deposition

HfB_2 thin films were grown on various substrates by CVD from a single precursor, $Hf(BH_4)_4$. Two different materials, single crystal Si (100) and 304 stainless steel, were chosen as substrates. A detailed description of the HfB_2 deposition used in this study is given by Jayaraman et al. (Jayaraman et al., 2005) and is under further development by A. Cloud and J. Abelson. All substrates were cleaned in an ultrasonic bath for 10 min (in acetone), another 10 min in isopropyl alcohol, rinsed with de-ionized water and then blown dry with nitrogen before loading in the chamber. The base pressure of the chamber was 3×10^{-6} Torr. The precursor, hafnium borohydride, $Hf(BH_4)_4$, was chilled to 4 °C. At this temperature, the typical pressure of the precursor was ~162 mTorr in the delivery line and an average pressure of 0.075 mTorr in the chamber. The typical size of the substrates made of silicon were 1.5×2.5 cm^2 and a steel substrate made of 304 stainless steel had a diameter of 3 cm. Various HfB_2 films were grown on each substrate with various substrate temperatures ranging from 250 to 400 °C. After depositing HfB_2 films on a silicon substrate, half of the sample was typically kept as an “as-deposited” sample and the other half was then annealed in a tube furnace to 700 °C for 1 hour under a reduced atmosphere to prevent oxidation (forming gas, 95% Ar, 5% H2). The morphology and thickness of the films were characterized by scanning electron microscopy (SEM) and roughness of the films was measured by a tapping mode atomic

force microscope (AFM).

6.2.2 Hardness and Modulus Measurements from Nanoindentation

Nanoindentation was performed to obtain the reduced modulus and hardness values. A cube corner indenter was used instead of the widely used Berkovich indenter to extract accurate material properties at shallow indentation depth less than 50 nm. All the measurements were done using a Hysitron TS 75 Triboscope. Collected loading and unloading data from each indent was analyzed with the Oliver and Pharr method (Oliver, 1992). A detailed data processing procedure is described in Chapter 3.2.

6.2.3 Adhesion and Shear Strength Measurements from Nanoscratch

Adhesion between the coating and the substrate is one of the most important properties determining the tribological performance of a layered system. It determines the durability of devices coated with hard films since a poorly adhered film to the substrate results in delamination of the coating and the devices will then wear quite rapidly. The large number of different test methods, such as the four-point bending, peeling, nanoindentation and nanoscratch tests characterizing adhesion reflects the importance of adhesion, but none of these techniques is “perfect” (Mittal, 1976).

As one of the representative methods measuring adhesion, four-point bending is widely accepted (Dauskardt et al., 1998; Cui et al., 2005). In this test, a thin film is glued between two elastic substrates. One of the substrates has a notch made by a diamond blade. Sandwiched stack is loaded into four-point flexure to give rise to crack propagation through the substrate. The adhesion strength is determined by the strain

energy release rate associated with beam theory for four point bend configuration (Gage et al., 2005). However, this method has some limitations because the success is strongly dependent on the sample preparation process and testing procedure (Tran et al., 2011).

Another method for measuring adhesion strength of the coating at the interface is nanoindentation (Bull, 2005). The nanoindentation tester allows to measure load and displacement precisely with an initiation of a crack. By measuring the critical bucking length, interfacial fracture energy and adhesion can be obtained. However, to initiate the delamination of the coating, the nanoindentaion method relies on the formation of a large plastic zone in the substrate. When a ductile film is adhered to a hard substrate, it is impossible to introduce any delamination events. It is also hard to quantify the results when a brittle substrate experiences cracks instead of plastic deformation.

The nanoscratch method is one of the choices in measuring adhesion. A sharp diamond tip is used to initiate the delamination of the coating with the combination of tip movement moving in vertical and horizontal directions along the surface. The nanoscratch testing method is considered to be the best way measuring adhesion in a sense that the indenter tip generates stresses that exceed the interfacial strength of a well-adhering film. That means that this method can be used for measuring adhesion strength along the interface between the coating and the substrate. However, the relationship between the critical load and adhesion is not well understood because of the complicated stress distribution at the end of the tip.

Various models have been developed to determine adhesion and shear strength as

well as energy release rate at the interface from a scratch test. The applicability of these models depends on the failure mode observed. Benjamin and Weaver (Benjamin et al., 1960; Ashcroft et al., 1993) analyzed the interfacial shear strength produced at the coating-substrate interface for coating removal given by

$$\tau_c = \left(\frac{HP_c}{\pi[r^2 - (P_c / \pi H)} \right)^{1/2} \tag{6.1}$$

where τ_c is the shearing force per unit area to delaminate the coating given in terms of the substrate harness H, the critical applied load P_c and the radius of the stylus point r. This analysis is applicable when the substrate deforms plastically.

Laugier (Laugier, 1984) and Bull et al. (Bull et al., 1988) developed a model to estimate the surface energy of an interfacial crack G_c which can be determined using the Griffith energy balance approach

$$G_c = \sigma_c t / (2E_f) \tag{6.2}$$

where σ_c is the local stress, t is the film thickness and E_f is the elastic modulus of the film. These models have different expressions for σ_c. Laugier considers that

$$\sigma_c = \sigma_a + \sigma_{in} \tag{6.3}$$

with

$$\sigma_a = (2P_c / \pi d_c^2)[((4 + \upsilon_s)3\pi\mu / 8) - (1 - 2\upsilon_s)] \tag{6.4}$$

where σ_{in} is the internal stress and σ_a is the stress induced by the sliding of the spherical indenter, i.e., adhesion strength, d_c is the residual scratch track width for the critical load,

μ is the measured friction coefficient of the indenter sliding given by the nanoscratch tester, and v_s is the Poisson's ratio of the substrate (Hamilton et al., 1966).

Kriese et al. proposed a model to estimate the strain energy release rate G_c stored in the film from the scratch elastic stress distribution. The delamination due to normal and tangential forces was induced by the combination of interface shear stress, the indentation-induced stress and residual stress in the film. The obtained strain energy release rate was given by

$$G_c = \sum \left[\frac{\tau_{ij}^2}{2G} t + \frac{\sigma_{ij}^2}{2E} t \right] \tag{6.5}$$

where τ_{ij} and σ_{ij} are shear and normal stresses in the delaminated film, respectively obtained using the Boussinesq solution, G is the film's shear modulus and t is the film thickness. This model assumes that a failure occurs due to chipping in front of the indenter and the elastic strain energy stored in the coating above the chipped area, right before chipping, is released by interfacial fracture at the critical load.

In an actual test, it is observed that the failure of HfB_2 films does not occur in the way as Kriese et al. expected. Thus, it is determined that further analysis should be performed with the most relevant models suggested by Benjamin et al. and Laugier (Eq. (6.1) and (6.4)).

A nanoscratch test was performed using a TS 950 Triboscope equipped with a 3D Omniprobe manufactured by Hysitron as shown in Figure 6.1. 3D Omniprobe has a pre-stressed piezoelectric material which provides actuation of the probe in normal direction

providing much higher normal force up to 2.6 N compared with the standard capacitive transducer (Max. 12 mN). Thus, this high load transducer was used in the experiment to induce enough stress required to cause delamination of HfB_2 coating on a silicon substrate.

A cono-spherical tip shown in Figure 6.2 with a 60° included angle and 4.95 μm radius of curvature was used in the experiment. All the measurements were performed in load-controlled mode to clearly capture the discontinuity at the event of delamination in a displacement plot. A continuously increasing ramp loading profile was used for the test and the applied peak loads were varied from 90 mN to 160 mN. The traverse scratch length was 100 μm and the velocity of the tip in the horizontal direction was 1 μm/s. After the test, to investigate the delamination at the interface, scratch tracks were examined by SEM.

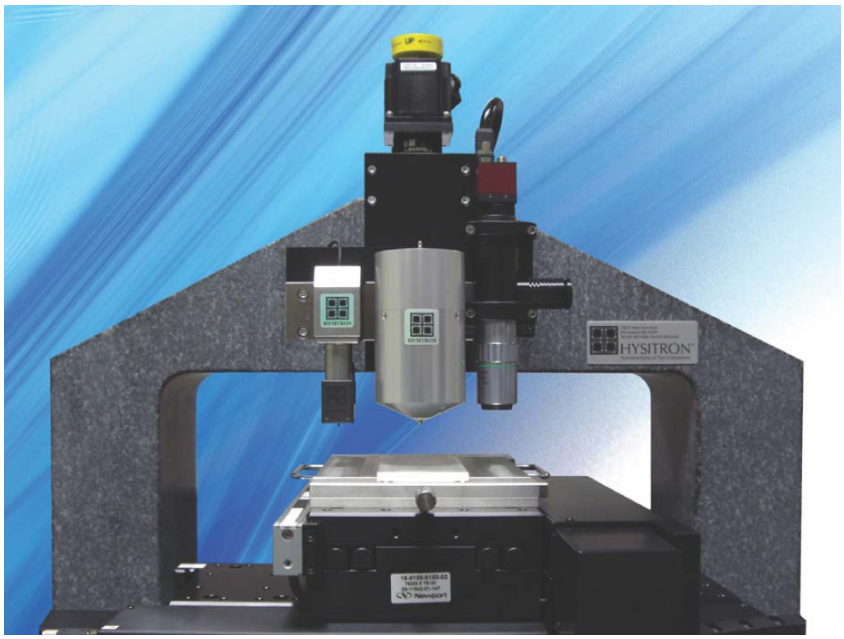

Figure 6.1 Image of Triboindenter with Omniprobe (center) used for a nanoscratch test (image taken from hysiton.com).

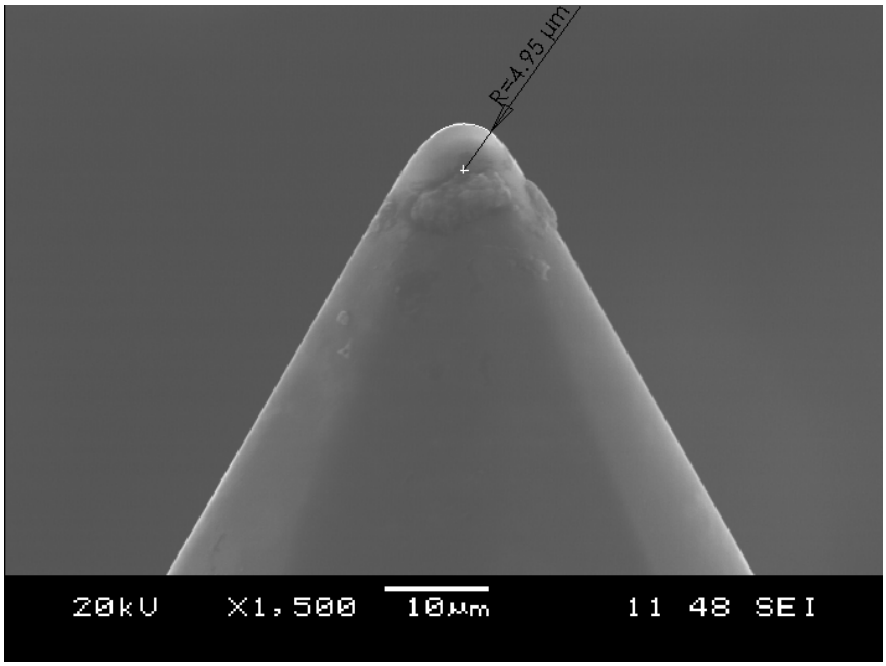

Figure 6.2 SEM image of the cono-spherical tip used for scratch.

6.2.4 Pin-on-disk Test

A conventional pin-on-disk tribometer was used to perform pure sliding wear experiments for HfB_2 films as shown in Figure 6.3. The equipment (called High Temperature Ttribometer, HTT) used in these tests provides the capability of high temperature testing up to 1000 °C wherein materials are exposed under a variety of temperature and stress conditions. However, the effect of high temperature was not investigated in these experiments, so all the tests were conducted at room temperature of 25 °C. Two as-deposited HfB_2 films (T_{sub}= 270 °C, t= ~200nm) deposited on 304 stainless steel (Fe, <0.08% C, 17.5-20% Cr, 8-11% Ni, <2% Mn, <1% Si, <0.045% P, <0.03% S) were prepared. The rms roughness values of the two substrates were 276.6 nm and 13.65 nm, respectively. The ball used in the experiments was a 9.5 mm diameter carbon steel ball with a hardness of 60 HRC and was mounted on a pin holder which applied a normal load of 3 N. The initial Hertzian contact pressure between the 304 steel and carbon steel ball was 608 MPa. The tests were performed at a sliding linear velocity of 0.11 m/s and at a track radius of 5 mm for 250 sec.

6.3. Experimental Results

6.3.1 Morphology and Thickness Characterization with SEM and AFM

Figure 6.4 shows cross-sectional SEM images of representative HfB_2 thin films grown on Si (100) substrates. The film shown in Figure 6.4 (a) was grown at a precursor pressure of 0.075 mTorr and substrate temperature of 300 °C for 7.5 min giving a thickness of 310 nm. Figure 6.4 (b) shows an annealed HfB_2 film which was annealed in

a tube furnace at 700 °C for 1 hour. HfB_2 films shown in Figure 6.4 (c) and (d) are a repeat of the aforementioned samples (Figure 6.4 (a) and (b)), but under 25% precursor pressure and 400 °C substrate temperature giving a thickness of 162 nm. Figure 6.4 (d) shows an annealed HfB_2 sample (800 °C, 1 hour) grown under 10 times higher precursor pressure than the first sample shown in Figure 6.4 (a).

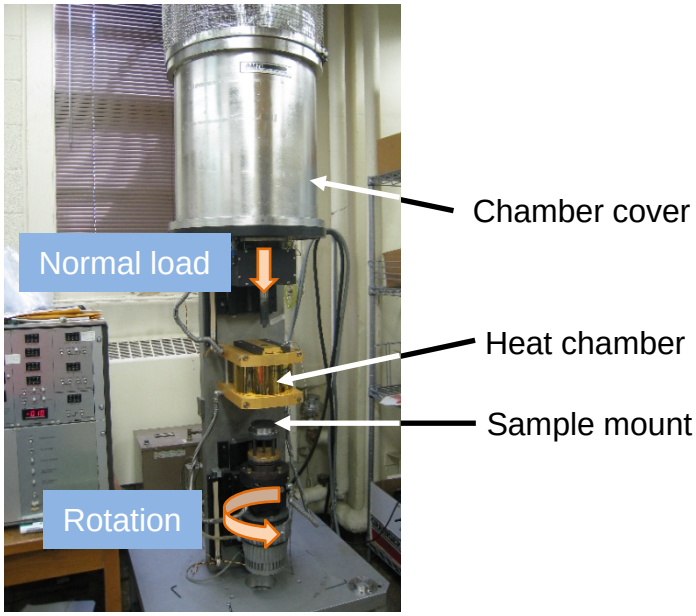

Figure 6.3 High Temperature Tribometer (HTT) capable of pin-on-disk test under conditions of up to 1000 °C.

The film microstructure is related to the substrate temperature. As the substrate temperature increases, the film becomes columnar and coarser. This was also confirmed by Jayaraman et al. (Jarayaman et al., 2005). The highest rms roughness of 11.98 nm was obtained from annealed HfB_2 film (Figure 6.5 (b)) while the as-deposited film showed a roughness of 6.13 nm (Figure 6.5 (a)). In the case of HfB_2 films grown at the temperature

of 400 °C, the roughness value decreased from 12.20 nm to 4.37 nm (Figure 6.5 (c) and (d)). The smoothest HfB_2 film was obtained when deposited at 300 °C with the precursor pressure of 0.75 mTorr as shown in the SEM image of Figure 6.4 (e). The measured roughness was 0.79 nm (Figure 6.5 (e)). Detailed deposition conditions and measured properties are summarized in Table 6.1.

Table 6.1 Deposition condition and measured properties of HfB_2 films by SEM and AFM.

	$P_{precursor}$ (mTorr)	T_{sub} (°C)	t (nm)	R_q (nm)
As-deposited HfB_2	0.075	300	310	6.13
Annealed HfB_2	0.075	300	307	11.98
As-deposited HfB_2	0.075	400	162	12.20
Annealed HfB_2	0.075	400	162	4.37
Annealed HfB_2	0.75	300	125	0.79

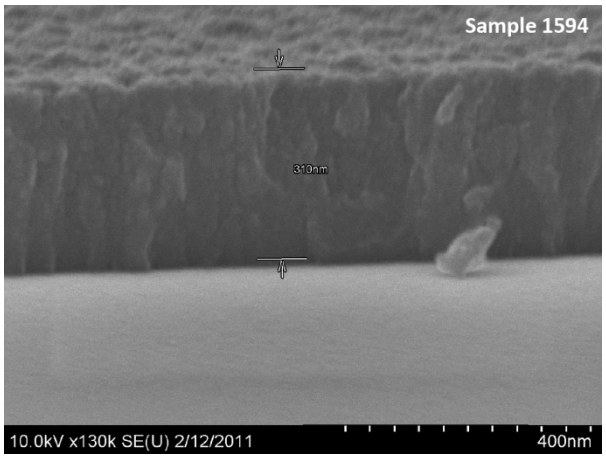

(a)

Figure 6.4 (cont. on next page)

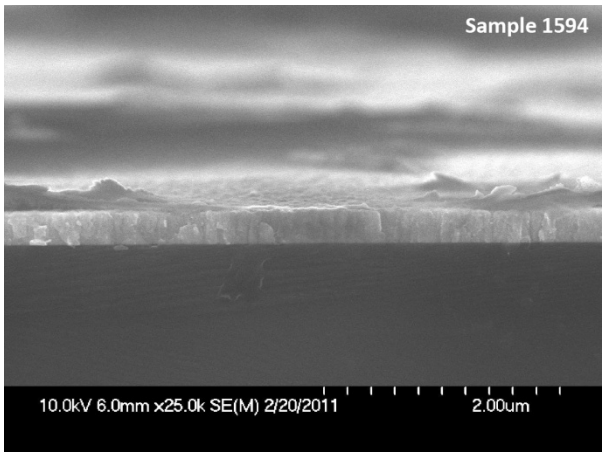

(b)

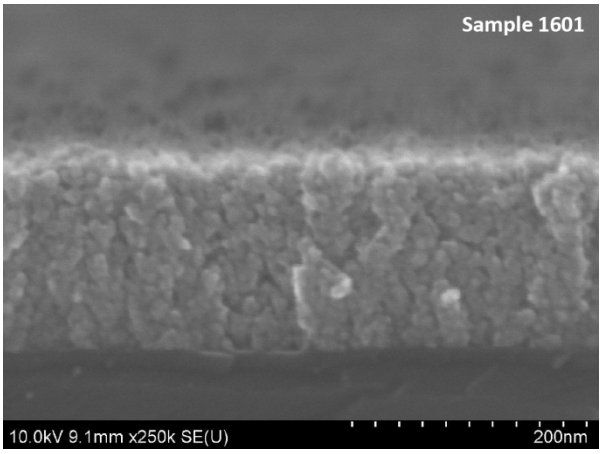

(c)

Figure 6.4 (cont. on next page)

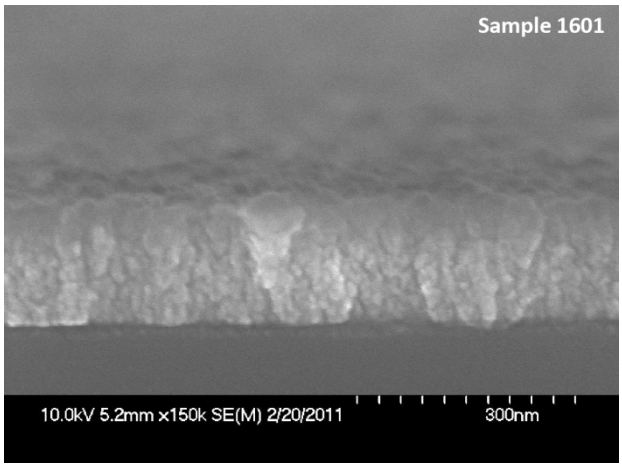

(d)

(e)

Figure 6.4 Cross-sectional SEM images of HfB_2 films: (a) as-deposited film deposited at 300 °C, (b) annealed film deposited at 300 °C, (c) as-deposited film deposited at 400 °C, (d) annealed film deposited at 400 °C and (e) annealed film deposited at 300 °C. (a)-(d) and (e) are grown under the precursor pressure of 0.075 mTorr and 0.75 mTorr, respectively (SEM images were taken by A. Cloud).

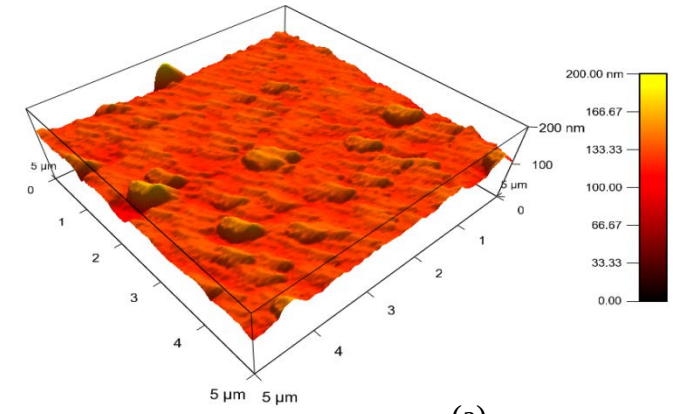

(a)

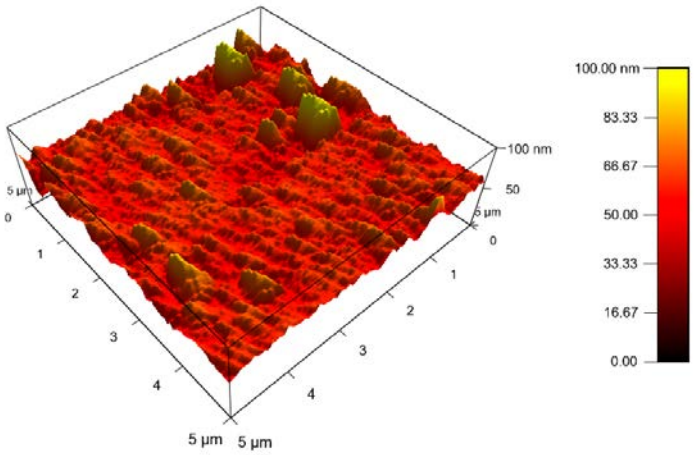

(b)

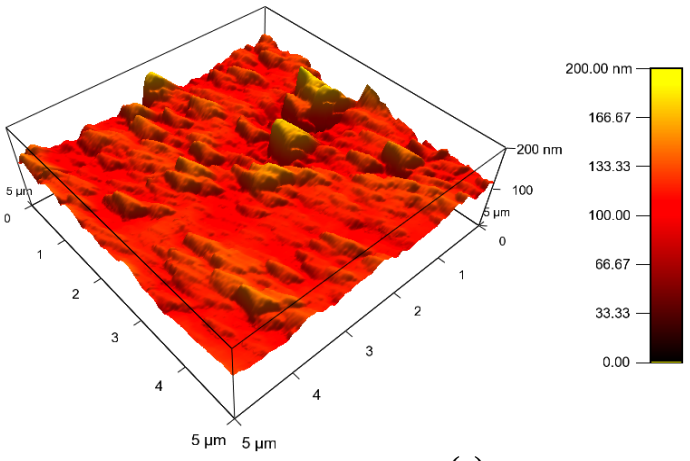

(c)

Figure 6.5 (cont. on next page)

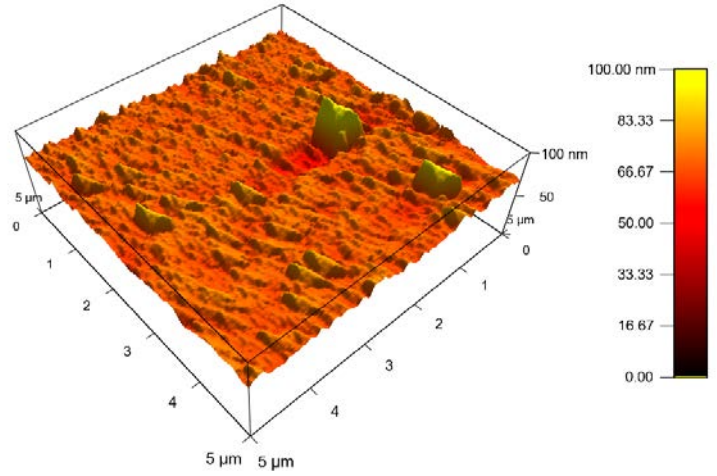

(d)

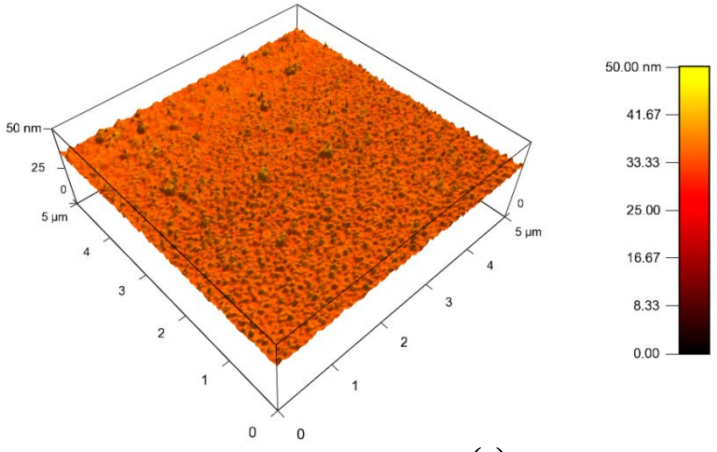

(e)

Figure 6.5 AFM images of HfB_2 films: (a) as-deposited film deposited at 300 °C, (b) annealed film deposited at 300 °C (c) as-deposited film deposited at 400 °C (d) annealed film deposited at 400 °C and (e) annealed film deposited at 300 °C. (a)-(d) and (e) are grown under the precursor pressure of 0.075 mTorr and 0.75 mTorr, respectively.

6.3.2 Hardness and Reduced Modulus of HfB_2 Films

The highest hardness and modulus were obtained from annealed HfB_2 film grown at a substrate temperature of 300 °C under precursor pressure of 0.75 mTorr. The highest

hardness value of all the films is 32.7 GPa obtained at a contact depth of 23.8 nm and the modulus obtained at the same contact depth is 225.6 GPa. The highest hardness value obtained in this work is lower than the value obtained by Chatterjee et al. (43 GPa) (Chatterjee et al., 2008) but still higher than the bulk modulus of 29 GPa. In the case of the other samples deposited at substrate temperatures of 300 °C and 400 °C under the precursor pressure of 0.075 mTorr, they showed lower hardness than the film deposited at 300 °C and 0.75 mTorr. Although there are slight changes in hardness and modulus values after annealing, the differences are very small. Hardness and modulus measurements results are shown in Figure 6.6 and the averaged values obtained below the contact depth of 30 nm are summarized in Table 6.2. As a rule of thumb, hardness values should be obtained at an indentation depth less than one tenth of the coating thickness. This rule of thumb can be used as a guideline. When there is a hard coating on a relatively soft coating, the substrate effect can be delayed. This can be verified from annealed HfB_2 film deposited at 300 °C and 0.75 mTorr. The hardness values start to decrease after a contact depth of 30 nm which is 30% of the coating thickness.

Table 6.2 Hardness and reduced modulus measurement results

	$P_{precursor}$ (mTorr)	T_{sub} (°C)	H (GPa)	E_r (GPa)
As-deposited HfB_2	0.075	300	12.4	184.7
Annealed HfB_2	0.075	300	13.0	226.0
As-deposited HfB_2	0.075	400	7.6	140.2
Annealed HfB_2	0.075	400	7.7	110.8
As-deposited HfB_2	0.075	300	22.4	219.7
Annealed HfB_2	0.75	300	32.3	227.0

6.3.3 Adhesion and Shear Strength Measurements by Scratch Testing

For the nanoscratch tests, four different HfB_2 films were prepared. Two samples were deposited at a substrate temperature of 350 °C and the other two samples were deposited at 300 °C. Two samples remained as as-deposited and the other two samples were annealed at 700 °C for 1 hour. Elastic modulus and hardness were obtained in the nanoindentation test and the obtained properties are summarized in Table 6.3.

In the scratch testing of HfB_2 films, the procedure is to move the tip across the coated surface with ramp loading profile. When there is a failure with a sudden jump in the normal direction, it is defined as a critical load. The location of failing point is also verified with an SEM image. The SEM image showing the scratch track and displacement plot for as-deposited HfB_2 deposited at 300 °C is shown in Figure 6.7. Figure 6.7 (a) shows the point where detachment of the HfB_2 coating is initiated during scratching. Figure 6.7 (b) shows the time-displacement plot obtained during the scratch. There is a discontinuity in the plot which corresponds to the onset of detachment in the

SEM image. The critical load is obtained from the normal force curve at the corresponding time determined from the normal displacement curve. In the case of as-deposited film deposited at a substrate temperature of 350 °C, the critical load obtained from the experiment was 83.5 mN and substituted in Eq. (6.1) with the other measured values of hardness (13.8 GPa) and radius of indenter tip (4.95 μm) to obtain the shear strength at the interface. The parameters in Eq. (6.4), such as residual scratch track width d_c, was measured from the SEM image and the friction coefficient μ, was obtained from Figure 6.7 (d). Poisson's ratio of 0.28 for a silicon substrate was used. By substituting the above parameters in Eq. (6.1) and Eq. (6.4), a shear strength of 4.0 GPa and an adhesion strength of 1.1 GPa for as-deposited HfB_2 film (T_s=350 °C) are obtained. Adhesion and shear strengths for the other three samples were obtained in the same manner described above and are listed in Table 6.3 as well as all the parameters used for the calculations.

Table 6.3 Measured properties from nanoscratch and nanoindentation tests for HfB_2 films.

	T_s (°C)	t (nm)	P_c (mN)	d_c (μm)	μ	H (GPa)	E_r (GPa)	σ_a (GPa)	τ_c (GPa)
As deposited HfB_2	350	227	83.5	9.3	0.13	13.8	189.1	1.1	4.0
Annealed HfB_2	350	227	104.3	5.2	0.14	16.5	190.6	2.5	4.9
As deposited HfB_2	300	200	100.6	13.0	0.13	21.5	226.1	1.1	4.5
Annealed HfB_2	300	200	70.4	11.1	0.21	36.5	244.4	3.5	3.7

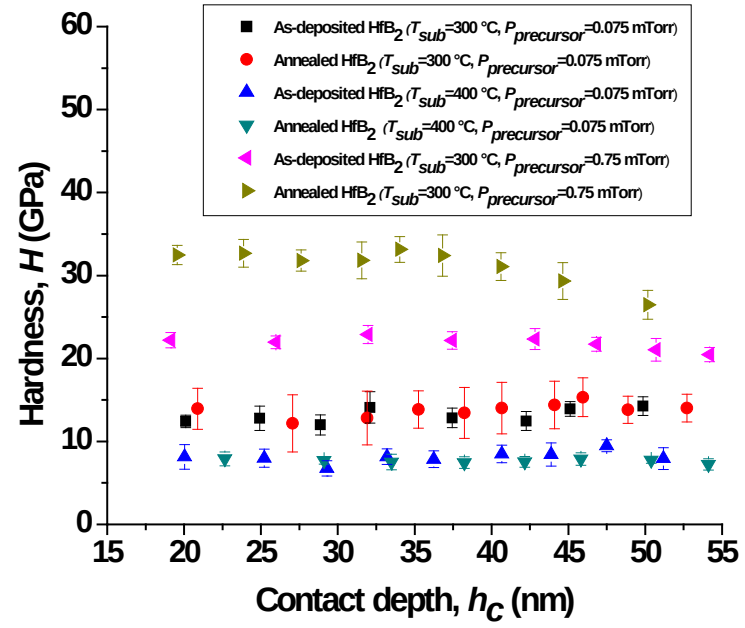

(a)

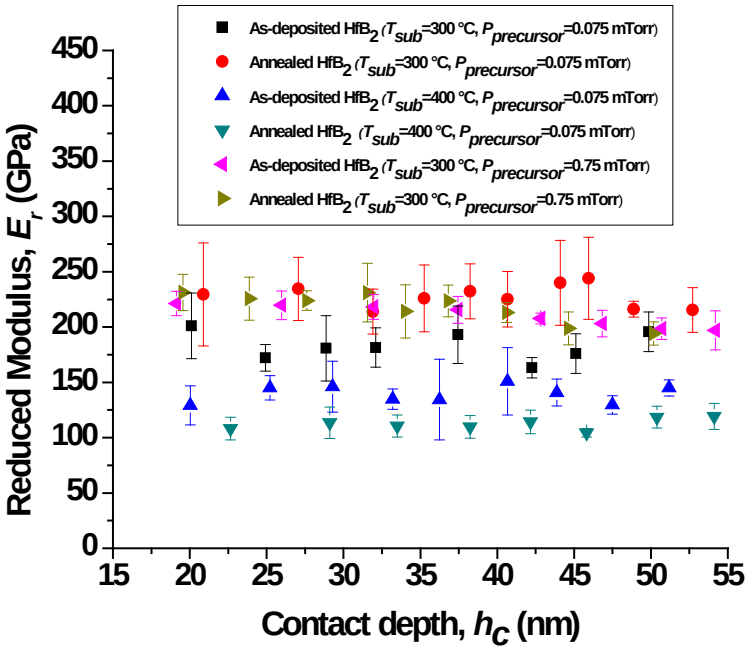

(b)

Figure 6.6 Plots of (a) hardness and (b) reduced modulus of HfB_2 films measured with cube corner tip.

It can be seen from Table 6.3, that the annealed HfB_2 film deposited at 300 °C is ranked as the best sample which exhibits the greatest adhesion strength (3.5 GPa) and two as-deposited HfB_2 films as the weakest (1.1 GPa). The annealed HfB_2 deposited at 350 °C shows the highest shear strength of 4.9 GPa while the annealed HfB_2 deposited at 300 °C shows the lowest (3.7 GPa). It appears that the annealing process contributes to increasing the adhesion and shear strengths of the coating system. This may mislead particularly in the case of annealed HfB_2 film deposited at 300 °C where the shear strength is reduced after annealing. It seems that the change of shear and adhesion strengths is related to annealing. According to Herr et al. (Herr et al., 1997), adhesion and hardness of the coating varied strongly depending on the residual stresses of the film. Sputtered HfB_2 films have intrinsic residual compressive stress up to -4 GPa depending on the bias voltage or deposition pressure. An annealing process usually leeds to a decrease of the residual stress in the HfB_2 layer and resulted in an increase of adhesion. This effect was intensified at an annealing temperature of 650 °C. In the case of Hf (B, N) coatings which were deposited with Ti-intermediate layers, their improved effect on the adhesion by the heat treatment was lost. Without performing more tests with various samples, it is hard to say whether the variation in adhesion is truly related with the annealing process or not. It is obvious that future work will be to characterize the effect of annealing process affecting the adhesion and shear strengths of HfB_2 films.

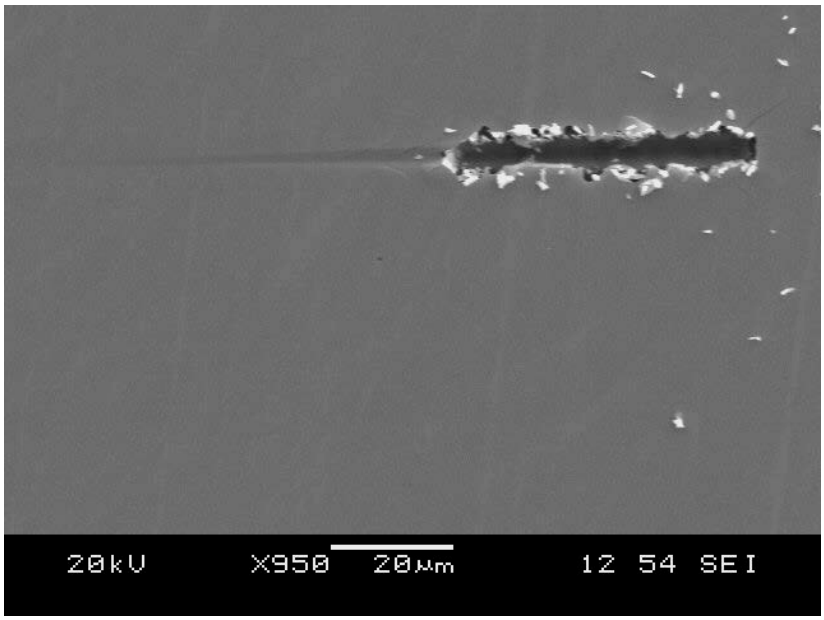

(a)

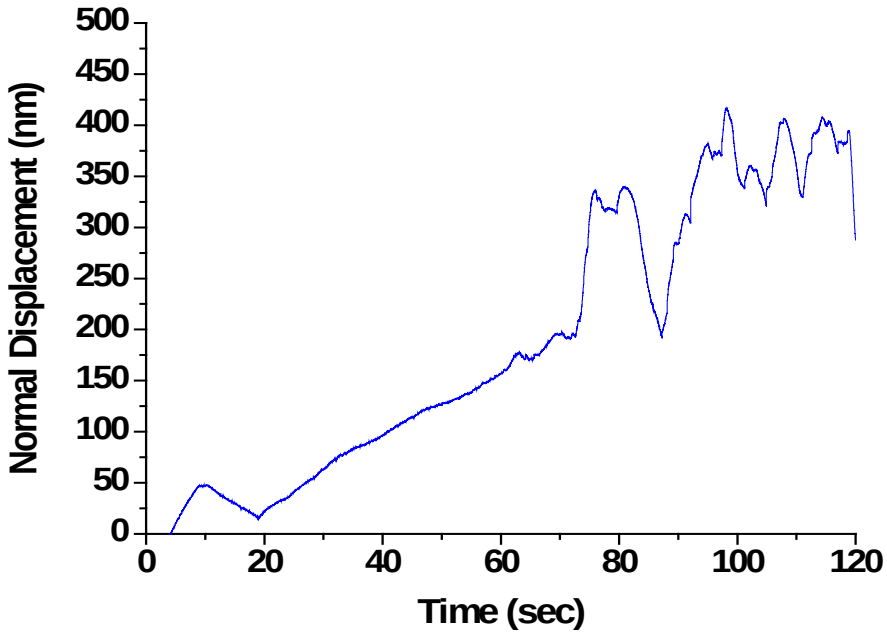

(b)

Figure 6.7 (cont. on next page)

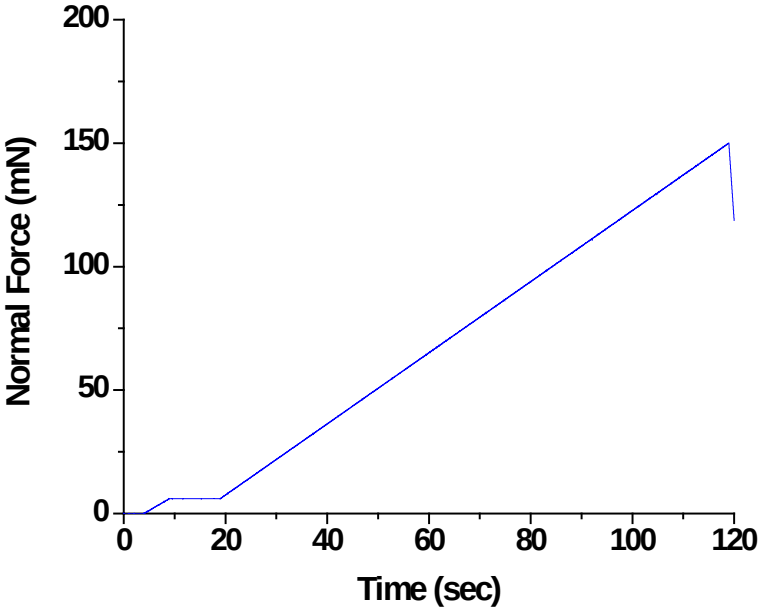

(c)

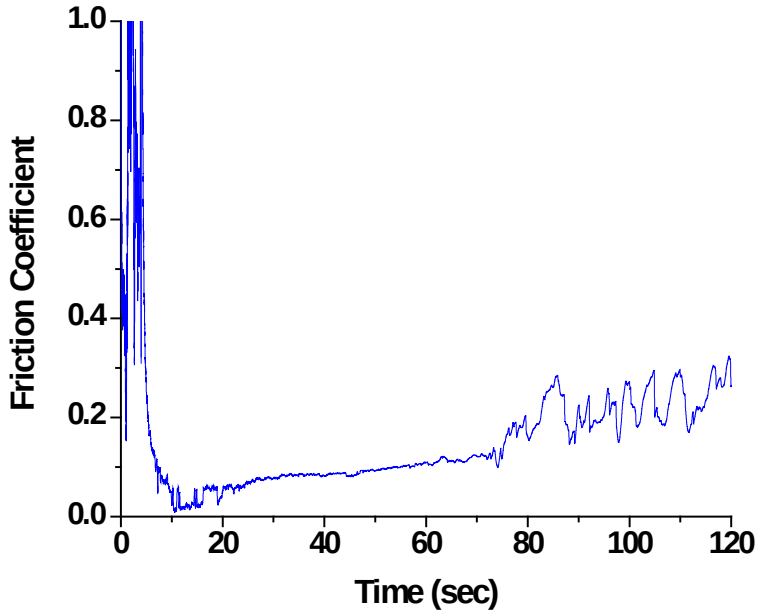

(d)

Figure 6.7 (a) SEM image of the scratch track, (b) normal displacement vs. time curve deposited at substrate temperature of 350 °C, (c) normal force vs. time curve and (d) friction coefficient vs. time curve for as-deposited HfB_2

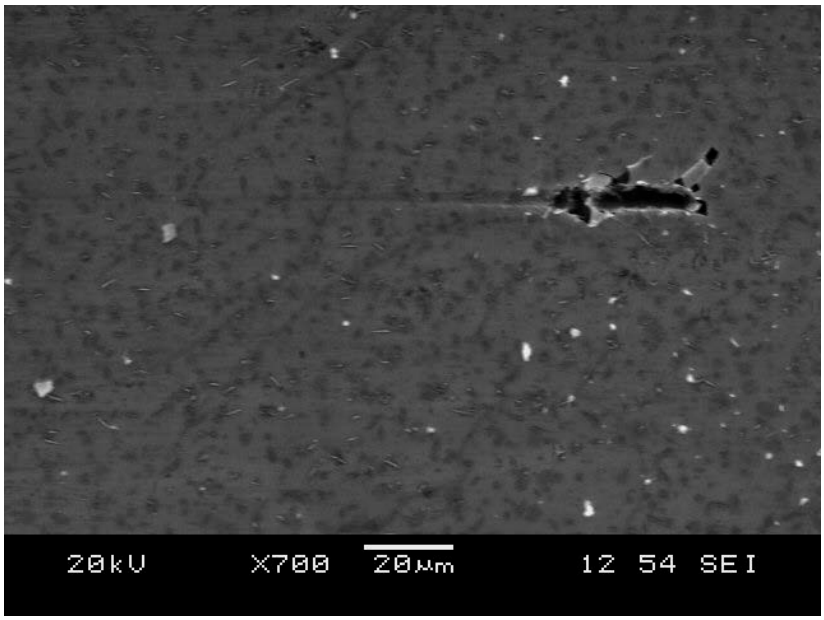

(a)

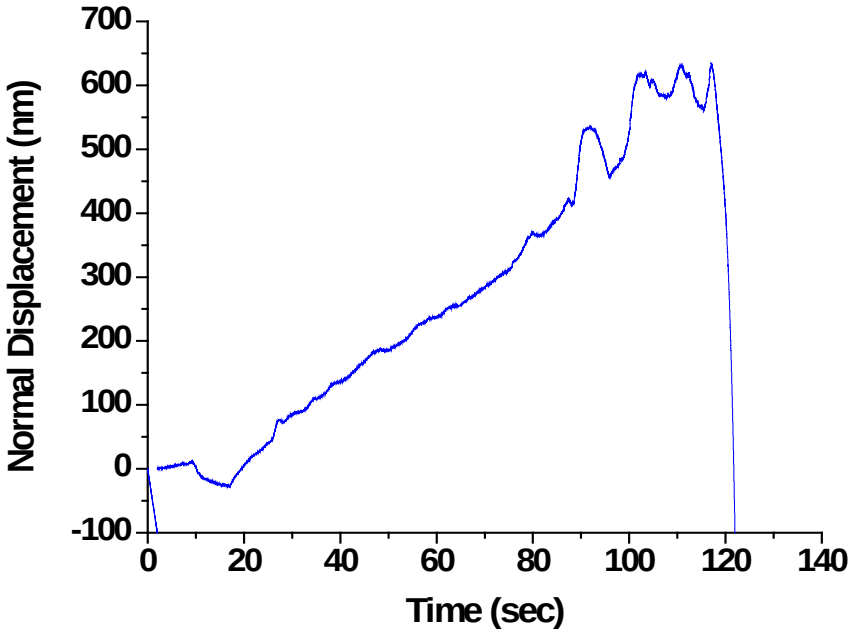

(b)

Figure 6.8 (a) SEM image of the scratch track and (b) normal displacement vs. time curve for annealed HfB_2 deposited at substrate temperature of 350 °C.

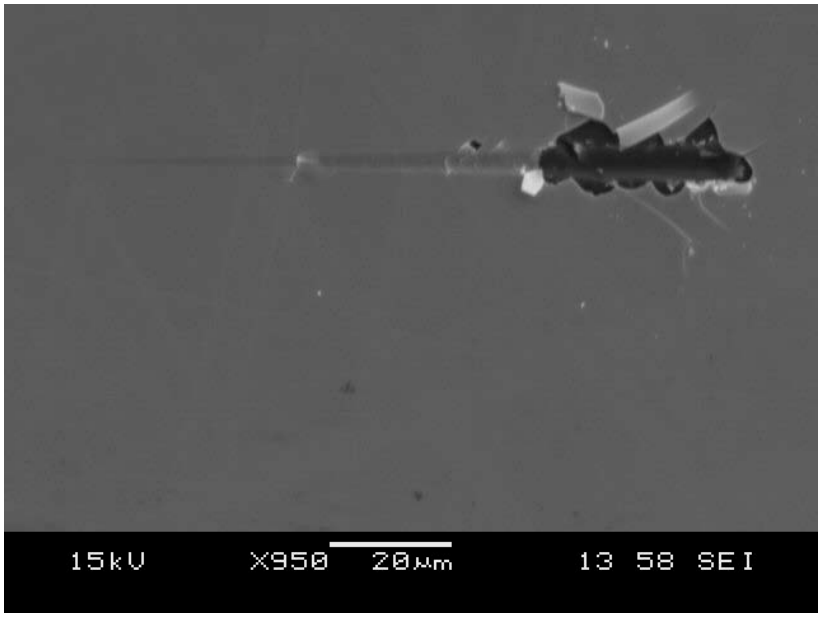

(a)

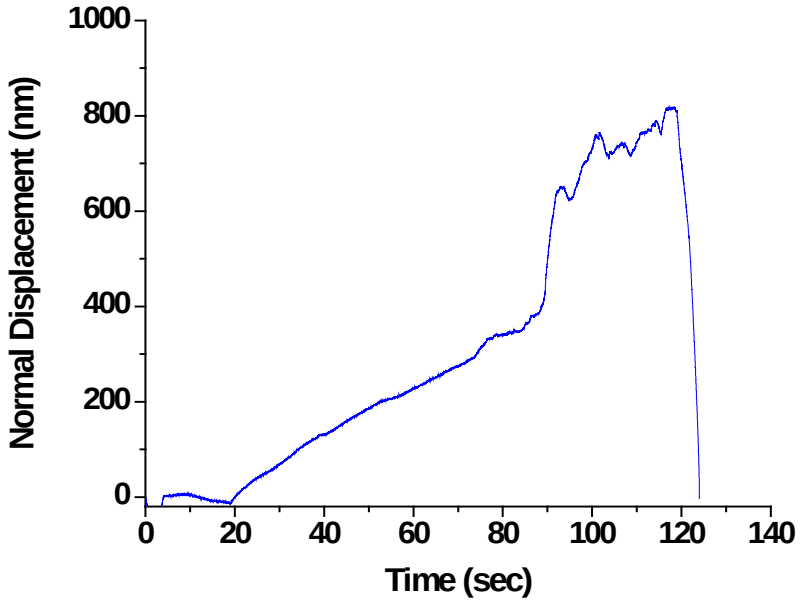

(b)

Figure 6.9 (a) SEM image of the scratch track and (b) normal displacement vs. time curve for as-deposited HfB_2 deposited at substrate temperature of 300 °C.

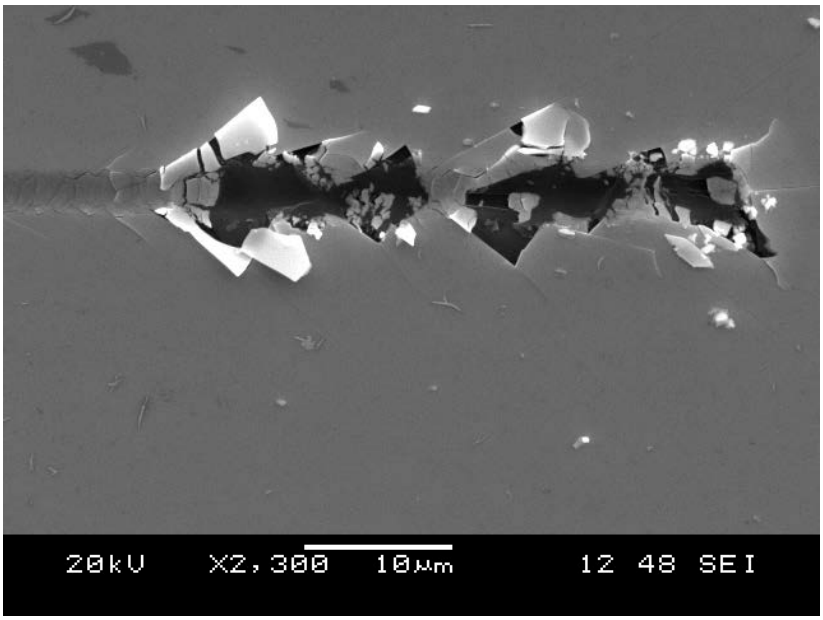

(a)

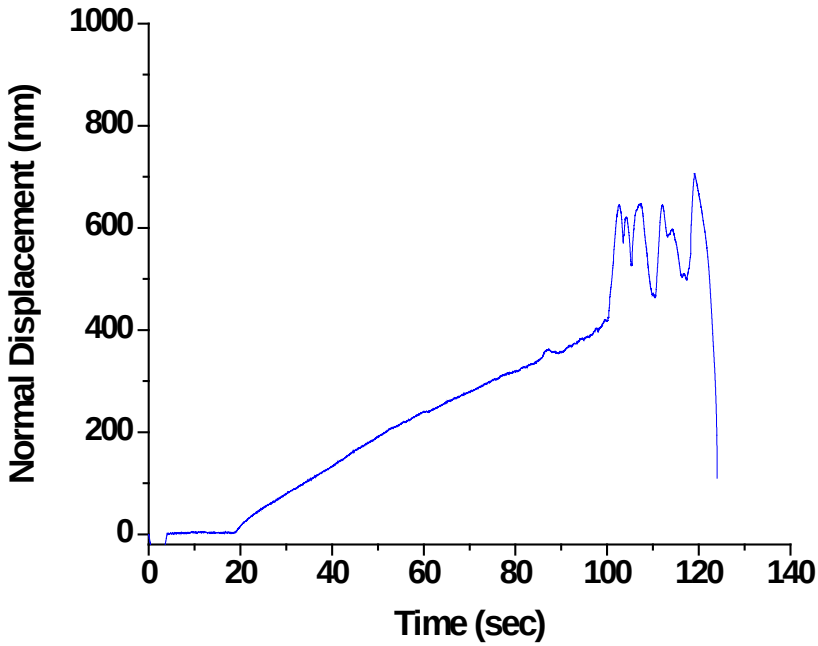

(b)

Figure 6.10 (a) SEM image of the scratch track and (b) the normal displacement vs. time curve for annealed HfB_2 deposited at substrate temperature of 300 °C.

6.3.4 Pin-on-disk Test Results

Figure 6.11 shows the friction coefficient values obtained during the tests. The friction coefficients of HfB_2 film deposited on rough 304 stainless steel (R_q=276.6 nm) gradually decreases starting from 0.76 to 0.58 after an initial run-in period of 25 sec, whereas, for the other rough HfB_2 film (R_q=13.65 nm) sharply decreases starting from 1.5 to 0.57 without any run-in periods. It is estimated that rough and smooth HfB_2 films were penetrated after 150 sec (sliding distance of 16. 5 m) and 60 sec (sliding distance of 6.6 m) of testing, respectively. Wear track scan data measured by a profilometer across the wear tracks are shown in Figure 6.12. It can be seen that both thin HfB_2 films (t=200 nm) are penetrated after a short period of testing time. It is found that the frictional behaviors of HfB_2 film measured at the macroscale are quite different from the nanoscale measurement results obtained by Chatterjee et al. (Chatterjee et al., 2008). They reported that as-deposited HfB_2 film showed favorably a low friction coefficient of 0.097 and good wear resistance.

Figure 6.13 shows the optical images of wear tracks for HfB_2 films after wear tests. Both images confirm that HfB_2 films are penetrated along the wear tracks. Microscopic investigation of wear tracks shows that both HfB_2 films were delaminated. As can be seen in Figure 6.13 (a) and (b), delaminated zone (brighter area) is observed along worn/unworn regime. Wear particles observed around the wear track in Figure 6.13 (b) look more like flaky and plate-like wear debris. These observations indicate that delamination is the main failure mechanism of HfB_2 films.

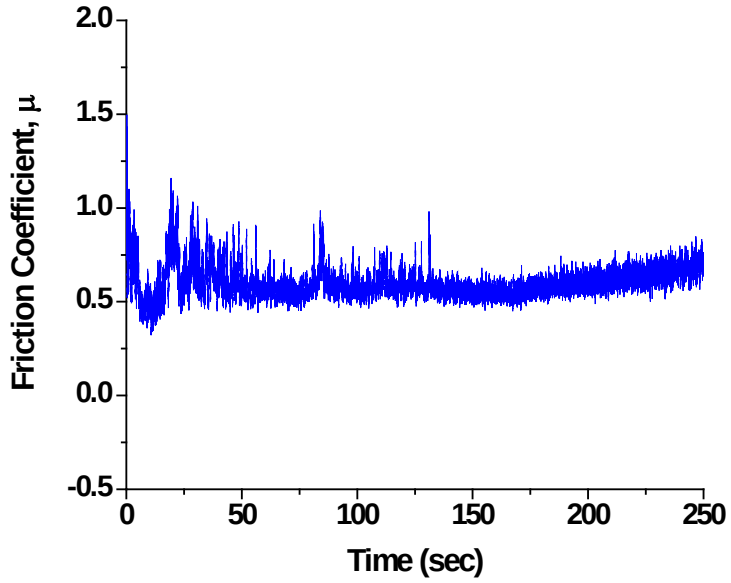

(a)

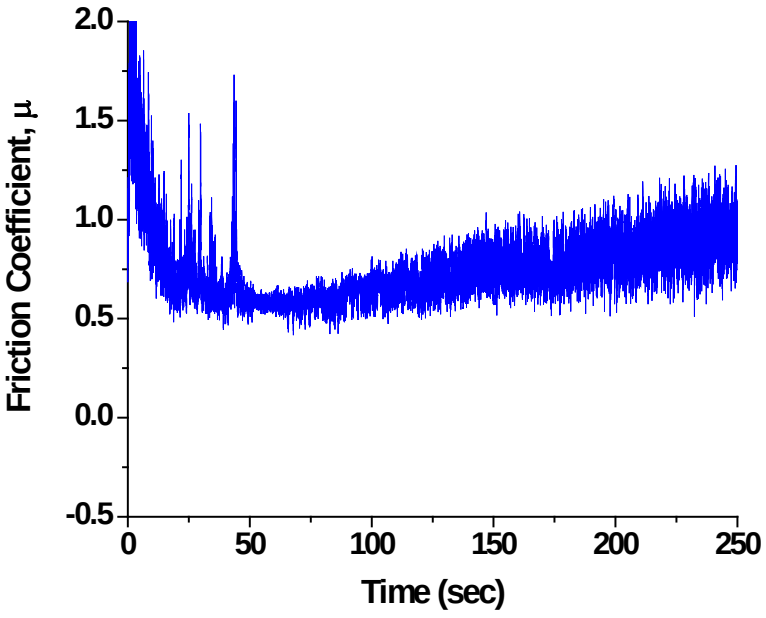

(b)

Figure 6.11 Friction coefficient plots for HfB_2 films deposited on (a) rough (R_q=276.6 nm) and (b) smooth (R_q=13.65 nm) 304 stainless steel.

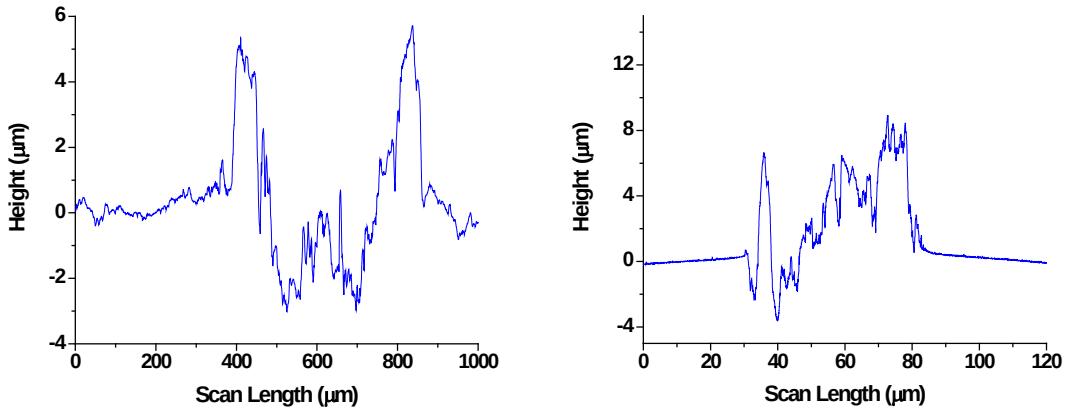

(a) (b)

Figure 6.12 Wear track scans for (a) rough (R_q=276.6 nm) and (b) smooth (R_q=13.65 nm) HfB_2 films (t= ~200 nm) deposited on 304 stainless steel.

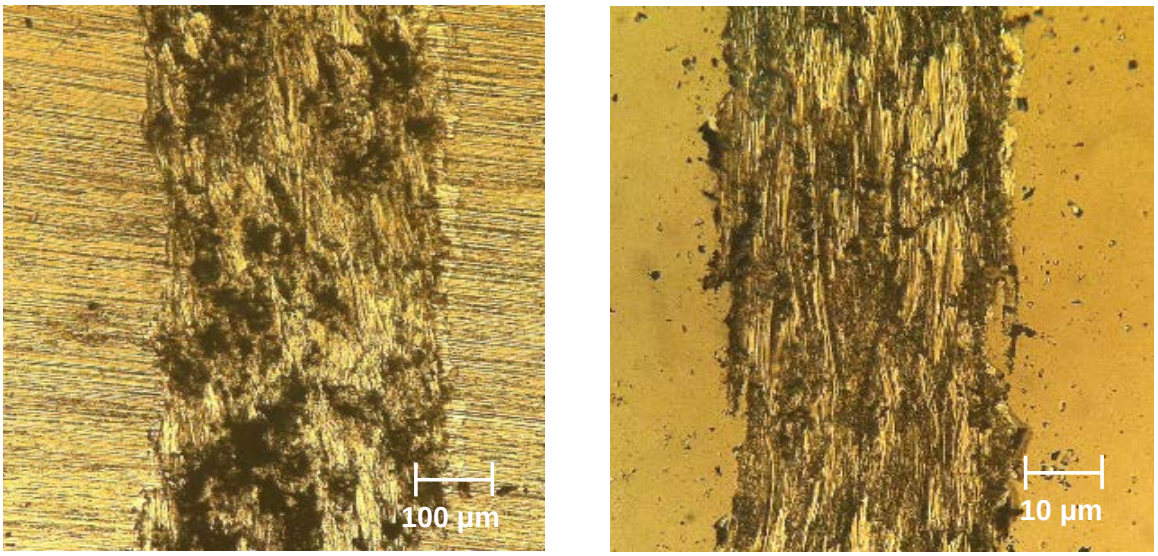

(a) (b)

Figure 6.13 Optical images of wear tracks for (a) rough (R_q=276.6 nm) and (b) smooth (R_q=13.65 nm) HfB_2 films (t= ~200 nm) deposited on 304 stainless steel.

6.4. Finite Element Modeling

With the development of new coating material, the need to evaluate the coating-substrate system increases. A number of theoretical and numerical analyses on the coating-substrate system have been made for examining the stress and strain distribution in the coating system. The influence of coating thickness, friction coefficient and material properties including elastic modulus on the elastic and elastic-plastic deformation for fully bonded layered system has been analyzed (Gupta et al., 1973; Gupta et al., 1974; Komvopoulos, 1998; Kennedy et al., 1974; Diao et al., 1992). However, Bhushan pointed out that wear of hard coating materials occurs in the form of fatigue and discrete delamination or detachment rather than in the form of removal by slow gradual wear (Bhushan, 2000).

In this work, the yielding behavior of HfB_2 films with the consideration of shear and yield strength at the interface is studied using FEA. Yield zone maps showing the critical maximum contact pressure for yielding and the location of yielding are constructed from the nanoscratch simulation results.

The commercial engineering software, ABAQUS was used to analyze the nanoscratching process of HfB_2 film coated on a silicon substrate. To validate the constructed finite element model, simulation of nanoindentation was performed beforehand and the FEA model is shown in Figure 6.14. The model is built with a quarter of the solid and the appropriate boundary condition was applied for the symmetric portion. The top part in Figure 6.14 describes the Berkovich tip widely used for

nanoindentation and assumed to be an analytical rigid body. It is approximated with a three-dimensional cone having an end radius of 150 nm and included angle of 142.3°. The bottom part in Figure 6.14 depicts the HfB_2 film coated on a silicon substrate. The top portion of the bottom part represents HfB_2 (elastic modulus, E_{HfB2}=292 GPa, yield strength, $\sigma_{y,HfB2}$=12 GPa and Poisson's ratio=0.15) with thickness of 200 nm. The interface between the HfB_2 film and the Si substrate is represented by cohesive elements (COH3D8) implemented in ABAQUS with an elastic modulus of 7 GPa and Poisson's ratio of 0.28. The cohesive zone is created with a finite thickness of 3 nm in the model. After meshing, the coordinates of the nodes in the cohesive layer are adjusted to have zero thickness. Thus, the effects of the cohesive layer thickness can be neglected. The substrate is made of silicon (elastic modulus, E_{Si}=127 GPa, yield strength, $\sigma_{y,Si}$=7 GPa and Poisson's ratio=0.28). The model is constructed with 8-node linear 3D stress elements (C3D8R) and densely meshed in the vicinity of the contact with approximately $3\times3\times3$ nm^3 element which is sufficiently small to permit adequate resolution of stress and strain fields. The density of elements becomes coarser as the point of interest moves away. The material used in the model is assumed to behave as elastic or elastic perfectly plastic and follow the von Mises yield criterion. The boundary conditions forcing the movement in all directions are assigned to the bottom plane.

Simulation of nanoindentation is performed by imposing the downward displacement to the indenter tip with a contact depth of 20 nm. After finishing the downward movement, the indenter tip is retracted until it does not make contact with the

surface. The friction coefficient is assumed to be zero during indenting. To validate the constructed finite element model, the results are compared with Hertzian analytical results.

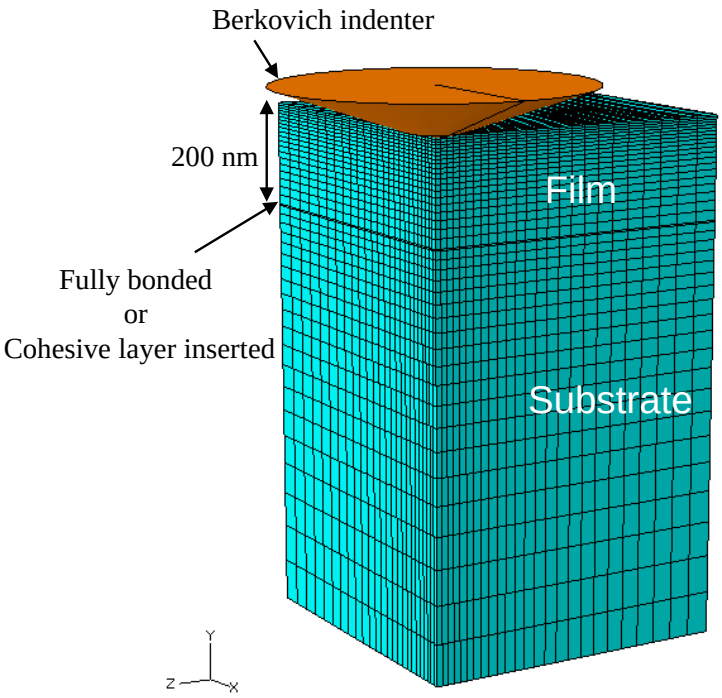

Figure 6.14 Finite element model for nanoindentation on HfB_2/Si system.

Figure 6.15 shows the model used for the simulation of the nanoscratch process. Some modifications were made from the model used for nanoindentation. Since both the normal and vertical motions of the indenter are considered in the nanoscratch process, half of the solid is modeled and the boundary condition is changed accordingly for the axisymmetric condition of the contact. The present model was simulated with actual experimental data obtained from nanoindentation and nanoscratch tests for the as-

deposited HfB_2 film deposited at a substrate temperature of 300 °C. The mechanical properties are summarized in Table 6.4. The top part in the model describes the cono-spherical tip having a sphere of radius 4.95 μm and it was simulated by undeformable rigid body. The top and bottom portion of the bottom part describes HfB_2 and Si, respectively, and are characterized as an elastic perfectly plastic material following the von Mises criterion. A fine mesh with a smallest element size of $10\times10\times10$ nm^3 was used in the coating and the substrate adjacent to the point of interest, i.e., near the contact zone. Away from the contact zone, relatively large elements were used in order to reduce computation time. The interlayer was inserted between HfB_2 film and Si substrate described with cohesive elements as in the nanoindentation model. A slightly different model without having an interlayer was also prepared and the effect of adhesion and shear strengths in the absence (fully bonded model) and the presence (cohesive zone model) of interlayer were examined. The thickness of interfacial layer was modeled to 10 nm. However, this interfacial layer effect was not considered in the calculation.

Simulation of nanoscratch was performed by imposing a downward displacement of 130 nm progressively on the indenter while the tip was moving in the horizontal direction up to 3900 nm simulating a ramp loading event. Stress profile and contact pressure at the interface and the surface at the onset of yielding were extracted. Since the purpose of this work is to construct the yield zone map considering the effect of the thickness of the coating and friction coefficient, a series of simulations were conducted with various film thickness of 50, 100, 200, 300, 400, 500, 600, 700 and 800 nm and

friction coefficient values of 0.1, 0.2, 0.3, 0.4 and 0.5. The computations were performed on a SGI Altix UV (ember) supercomputer with 2 processors (Intel® Xeon® Processor) and typical computation time was 5 hours for each run.

Table 6.4 Material properties used in the finite element model for nanoscratch.

	E (GPa)	σ_y (GPa)	ν	σ_a (GPa)	τ_c (GPa)
HfB_2 film	226.1	12	0.15		
Interface	127	7	0.28	1.1	4.5
Si substrate	127	7	0.28		

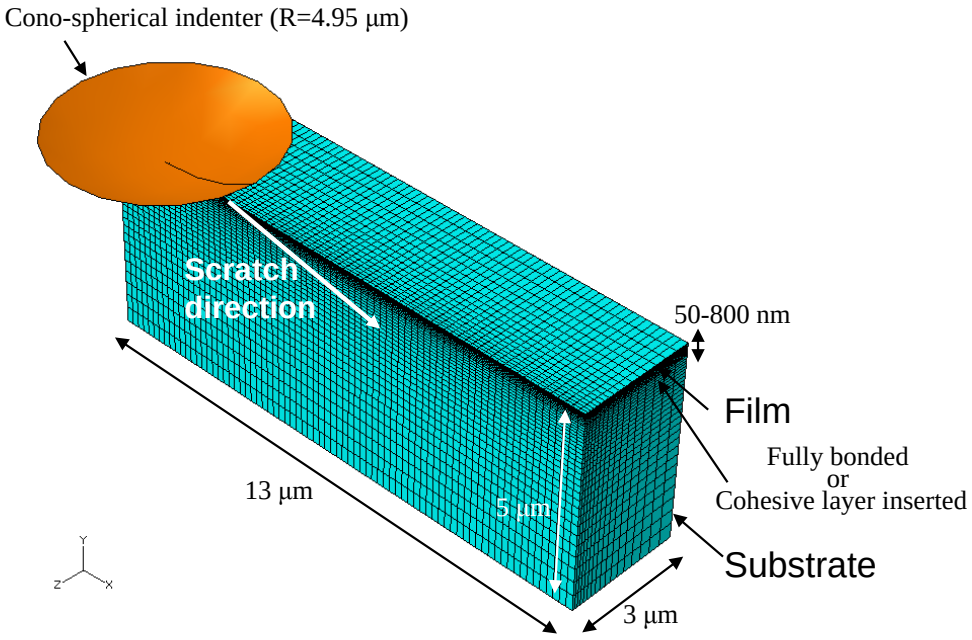

Figure 6.15 Finite element model for nanoscratch on HfB_2/Si system.

6.5. FEA Model Validation

Figure 6.15 shows the simulation results obtained from four different finite element models as well as the Hertzian analytical results. X-axis represents the normal approach between the indenter and the contacting surface normalized by the contact radius, $a_{contact}$. Y-axis represents the Hertzian contact pressure normalized by the effective elastic modulus, E^*.

It can be observed that the results obtained from four finite element models show good agreement in the elastic regime. Above the normalized normal approach of 0.27, plastic models start to deviate from Hertzian model because Hertzian theory does not account for the plastic behavior. The effect of cohesive layer was not detected because the maximum displacement given (20 nm) was not exceeded 10% of the film thickness (200 nm). It can be concluded that very good agreement has been achieved between the finite element models and the analytical solutions.

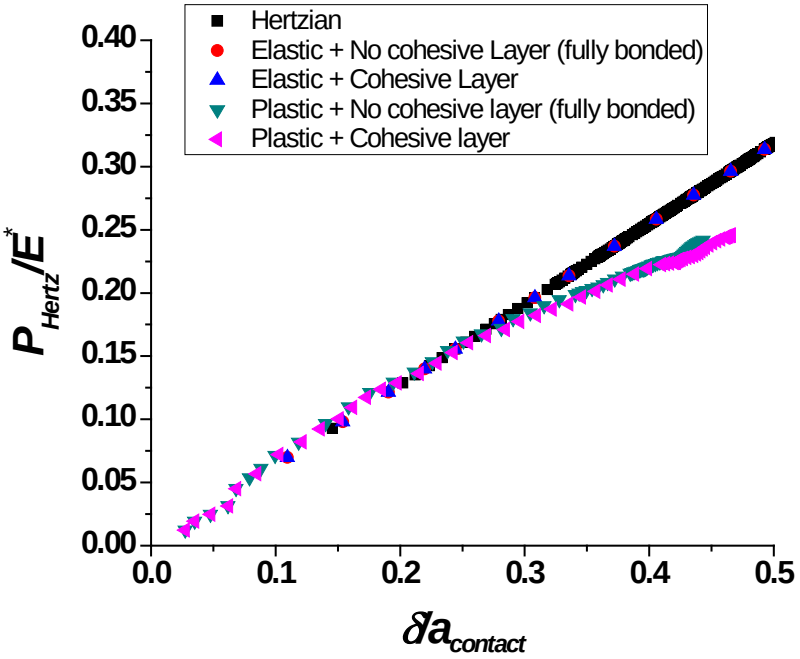

Figure 6.16 Comparison of Hertzian analytical model and finite element model for nanoindentation.

6.6. FEA Results

Figure 6.17 (a)-(d) show typical simulation results for fully bonded model of HfB_2/Si system. They depict contour plots of von Mises stress at the instant of initiation of plastic deformation. As seen from the images, the maximum stress and inception of yield occurs below the surface when the friction coefficient is low (μ=0.1) (Figure 6.17 (a)). Yield at the surface becomes dominant when the friction coefficient is high (μ=0.5) (Figure 6.17 (d)). As the thickness of HfB_2 film decreases, the stress field moves to the interface (Figure 6.17 (b)) and further moves down to the substrate (Figure 6.17 (c)). These trends also can be seen from Figure 6.18.

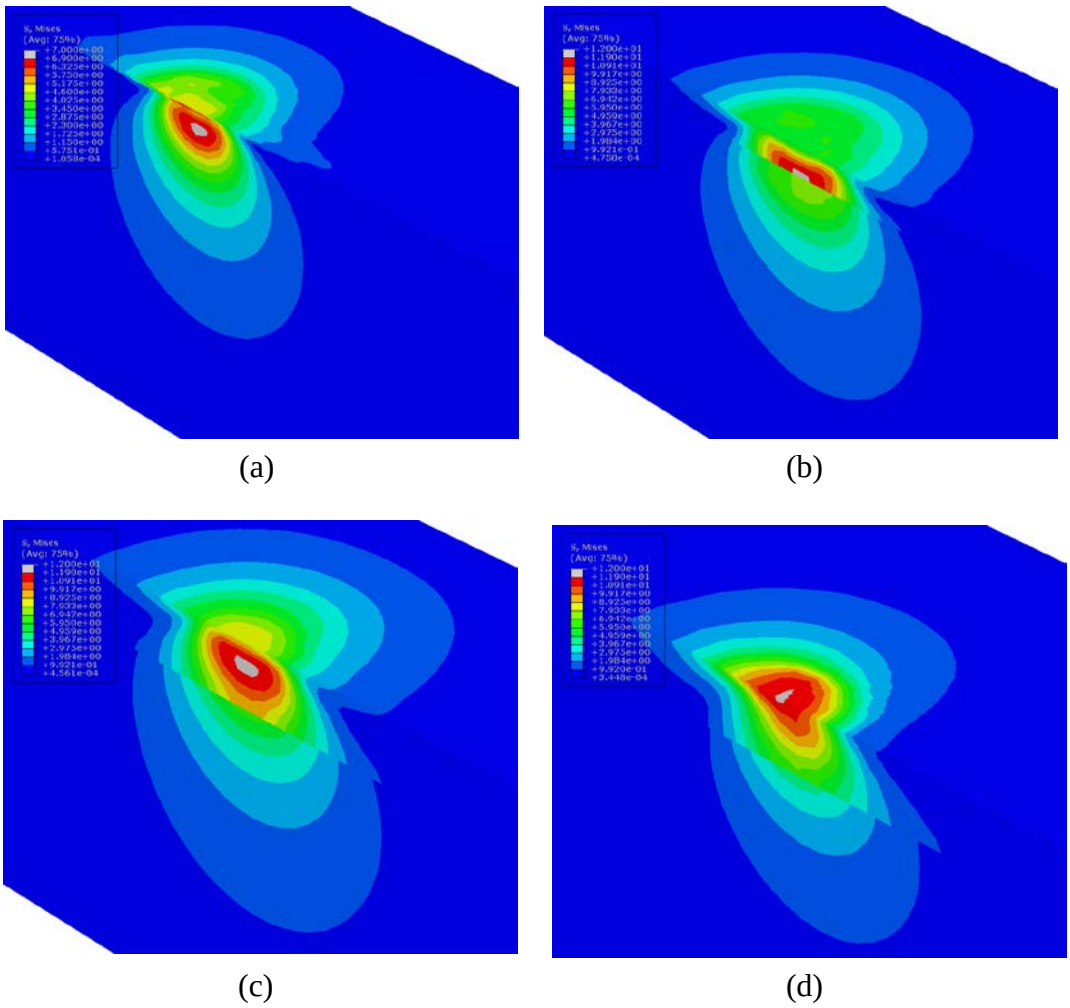

(a) (b)

(c) (d)

Figure 6.17 Contour plot of von Mises stress at the onset of yield in (a) substrate (t_{HfB2}=50 nm and μ=0.1), (b) interface (t_{HfB2} =400 nm and μ=0.1), (c) film (t_{HfB2}=800 nm and μ=0.1), and (d) surface (t_{HfB2}=700 nm and μ=0.5).

Figure 6.18 shows the relationship between the von Mises stress (interface: $\sigma_{VM,Si}$, and surface: $\sigma_{VM,HfB2}$) and the film thickness for several friction coefficient μ values obtained from fully bonded model. In the plot, σ_{VM} is normalized by the yield strengths of Si and HfB_2, respectively. In a similar way, the film thicknesses are normalized by the

half-contact width (a_y=547 nm) calculated by Hertzian theory at the inception of plastic deformation of homogeneous silicon.

It can be seen from Figure 6.18 (a) that the maximum yield strength is highly saturated at the interface. When the friction coefficient values are high or the film thicknesses are low, the location of yielding occurs away from the interface. The same trends can be verified from Figure 6.18 (b). Yielding occurs at the surface when the friction coefficient values are high.

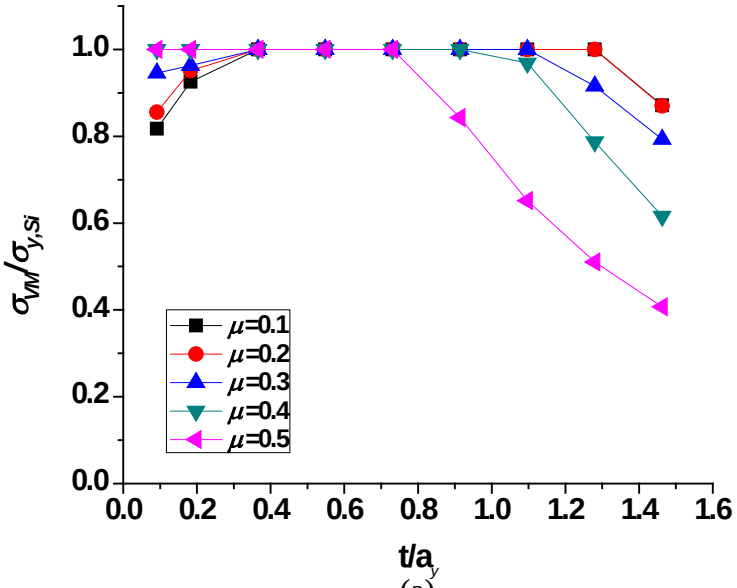

(a)

Figure 6.18 (cont. on next page)

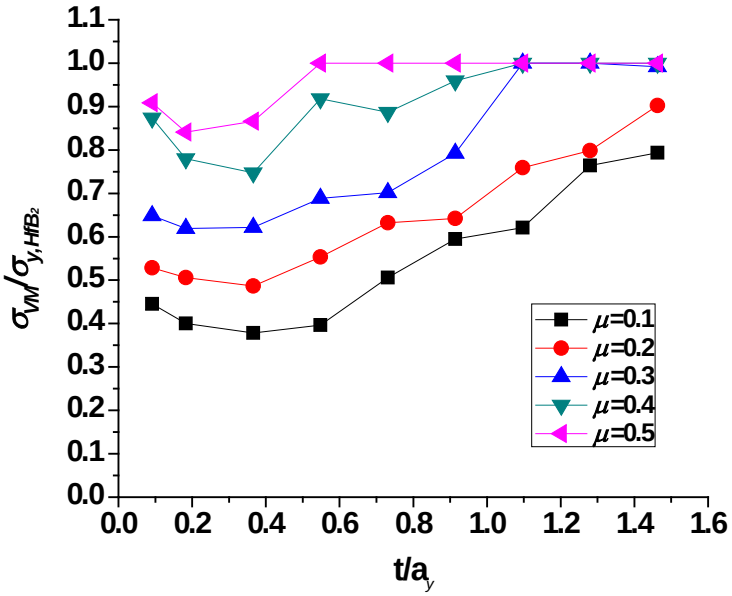

(b)

Figure 6.18 Variation of von Mises stresses at the first onset of yield at (a) interface (b) surface from fully bonded model.

Figure 6.19 shows the plots of von Mises stresses vs. the film thickness obtained from the cohesive zone model. None of the data points in Figure 6.19 were collected from the top boundary surface of silicon substrate adjacent to the interface layer. Also, the top surface of HfB_2 film is not saturated, which indicates that yielding does not occur in the HfB_2 film or silicon substrate but at the interface only. This has been clearly shown in Figure 6.20 and Figure 6.21.

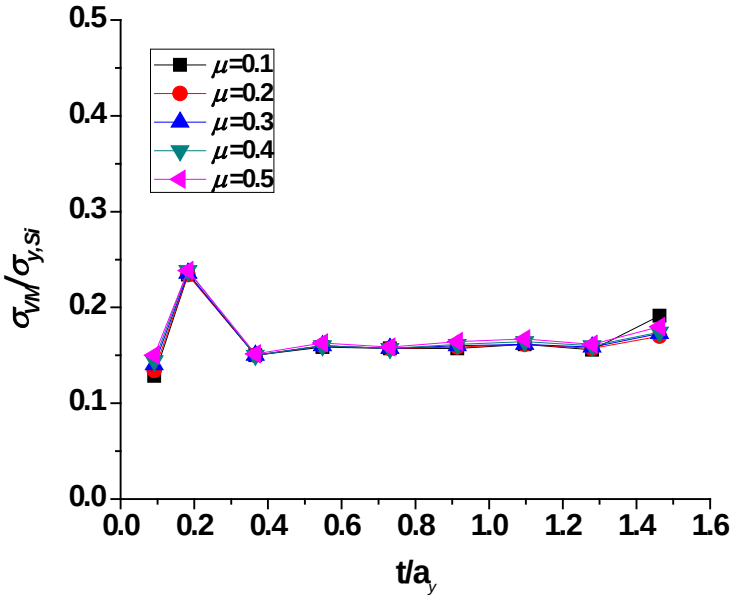

(a)

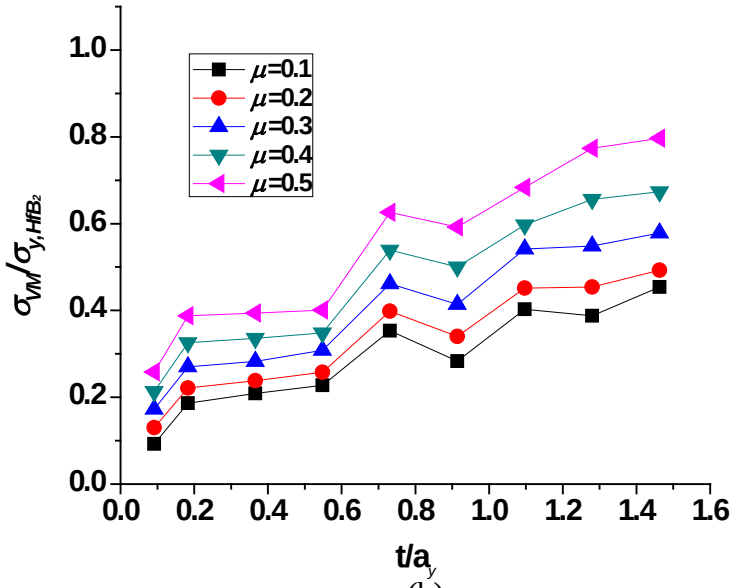

(b)

Figure 6.19 Variation of von Mises stresses at the first onset of yield at (a) interface (b) surface from cohesive zone model.

Figure 6.20 is a contour plot of maximum contact pressure, P_{cont}, required for the onset of yield obtained from a fully bonded model. This plot is overlaid with the yield zone map showing the different locations in the HfB_2/Si system where yielding initiated. Figure 6.21 was obtained in the same manner from the cohesive zone model.

Comparing these two maps, the effect of interfacial adhesion and shear strength becomes clear. When HfB_2 is assumed to be fully bonded to the substrate, the maximum pressure of 13 GPa can be obtained at the film thickness of 13 nm and the friction coefficient of 0.1. However, when it is assumed that HfB_2 is not firmly bonded to the substrate, the maximum pressure is dominated by the adhesion and shear strength (σ_a=1.1 GPa and τ_c=4.5 GPa) of the interface and a lower value of the maximum pressure of 9.07 GPa is obtained. This result is expected because yielding occurs at the interface at all given film thicknesses and friction coefficient values preceding the initiation of plastic deformation in the film or in the substrate in the case of the cohesive zone model. When the thickness of HfB_2 film increases from the current maximum thickness of 800 nm to 1.6 μm, the onset of yield in cohesive zone model occurs at the surface (μ=0.5 and Max. P_{cont}=10.63 GPa)

It is obvious that as the yield strength at the interface increases, the yield region moves from the interface to the location away from the interface as analyzed for the fully bonded model shown in Figure 6.20. Therefore, it can be concluded that the yield strength at the interface is an important factor for controlling the yielding position.

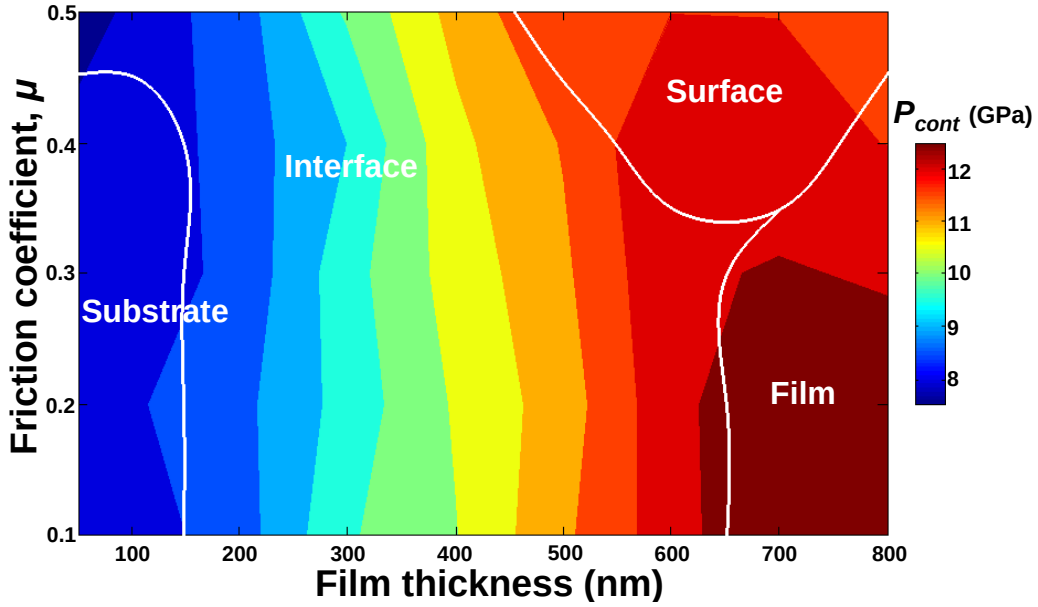

Figure 6.20 Contour plot of contact pressure at the onset of yield as a function of film thickness and friction coefficient overlaid with yield zone map for a fully bonded model.

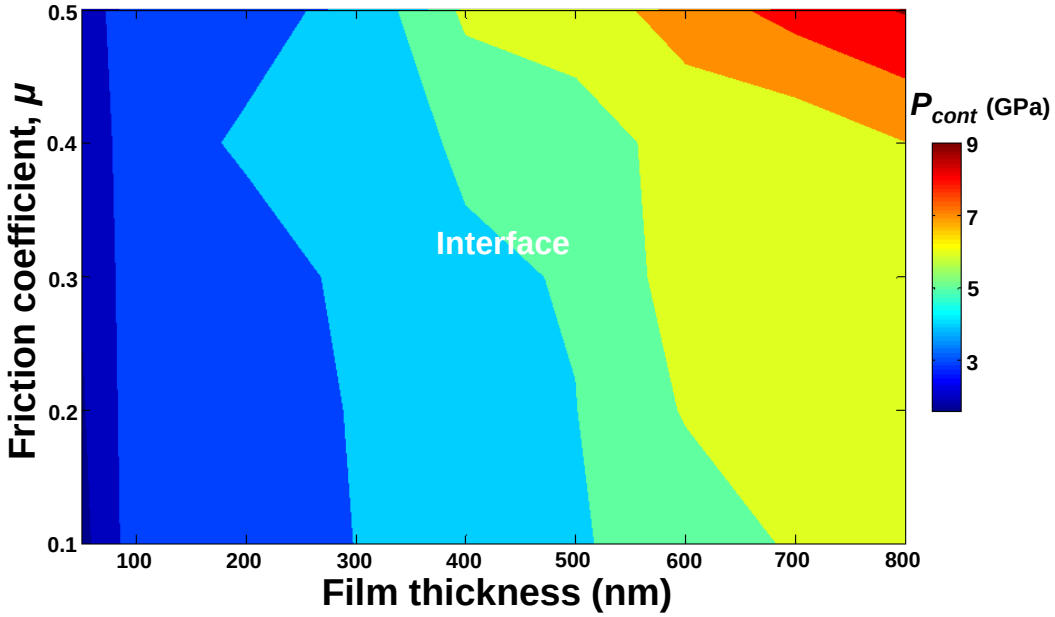

Figure 6.21 Contour plot of contact pressure at the onset of yield as a function of film thickness and friction coefficient overlaid with the yield zone map for the cohesive zone model.

6.7. Summary

The tribological behavior of the CVD-grown HfB_2 coatings was investigated. The mechanical properties of thin films deposited on a silicon substrate were measured including hardness, modulus, and surface roughness. Among a series of HfB_2 films, the films deposited at a substrate temperature of 300 °C and annealed at 700 °C for 1 hour had the highest hardness of 36.5 GPa. The smoothest film with rms roughness of 0.79 nm was obtained while deposited under conditions of precursor pressure of 0.075 mTorr and substrate temperature of 300 °C. From mesoscale pin-on-disk tests, an average value of ~0.5 friction coefficient was obtained before the ball penetrated the coating layer and the film lasted up to 16.6 m of sliding distance at 608 MPa contact pressure. This contact pressure is sufficiently low for film penetration and the coefficient of friction is high for general protective coating tribological applications. Microscale scratch testing was performed to measure the the film adhesion and the adhesion and shear strength, which was found to be 1.1 GPa and 4.5 GPa for as-deposited films and 3.5 GPa and 3.7 GPa for annealed films, respectively. In order to study the effect of adhesion strength between the film layer and the substrate, a finite element model was developed using cohesive elements with the properties as measured form the scratch experiments. The finite element analysis simulating nanoscratch revealed that the distribution of stress field and the maximum pressure required for the onset of yield are strongly dependent on the interface strength, as expected.

7. Conclusions and Future Work

This dissertation deals with tribological studies of thin solid films. Thin solid films are sufficiently thin that the substrate plays a role in determining the tribological behavior of layered system. Tribological performance of layered system cannot be easily determined by analyzing the tribological behavior of the coating material treated as a bulk material.

To understand the tribological behavior of layered system, we distinguished between four different zones, i.e., top surface, thin film layer, interface and substrate.

The top surface is the most dominant zone affecting the overall performance of layered system either by adhesion, wear or friction. We focused on the adhesion behavior of layered system in chapter 2. The experimental measurement of adhesion between two contacting surfaces was conducted under various shearing conditions.

The properties of thin film materials also have great importance. The coating material should possess a suitable combination of properties, e.g., hardness, modulus of elasticity, wear resistance, thermal conductivity and so on. In chapter 3, we showed experimental measurement results for a novel material, LCCO, deposited on substrate.

Good adhesion at the coating/substrate interface is one of important factors determining the performance of layered system. In chapter 6, material properties of hafnium diboride are measured including the shear and adhesion strengths at the interface. The measurement results taken from the experiments were implemented to FEA to predict the yielding behavior of hafnium diboride films coated on a silicon substrate.

The overall tribological performance of layered system cannot be determined only by characterizing the properties of thins films, i.e., adhesion, hardness, modulus of elasticity and shear strength at the interface. Considering that the tribological issues are always initiated from the behaviors of two bodies in contact, the contact behavior of layered system should be analyzed with the effect of substrate. The experimental study measuring the contact stiffness of layered surface with the inclusion of substrate effect was conducted and the measurement results were compared with the existing contact models (chapter 4). In chapter 5, the wear behavior of layered system was analyzed using FEA.

The main findings and future work for each corresponding chapter are summarized below.

7.1. Reversible Solid Adhesion

The experimental adhesion tests were performed with various combinations of materials and sizes under different shearing conditions. As a result of these tests, it has been found that faster motion of the bottom surface in shearing direction gives a lower pull-off force. It has been also found that the pull-off force is dependent on the material of the contacting surfaces and contact force applied as well as the ambient humidity.

The maximum ratio between the pull-off and pull-in forces obtained from a PR coated sample was 167 whereas the ratio obtained from gold coated samples was 24.2. It was found that adhesion can be controlled by the surface modification and pull-off force, and detaching two contact surfaces can be maximized and minimized with the proper aid

of shearing force.

Based on the experimental validation of solid surface adhesion, desired adhesion and pull-off adhesive force is expected to be achieved through a proper material selection (thin film and substrate material) and geometrical changes (surface roughness and surface texturing).

A pull-off force can be quantified from FEA if the top layer is modeled with a cohesive model assuming that the interface behavior between the top surface and the opposite surface depends on the cohesive energy. As far as cohesive energy can be obtained from a separate experiment (for example, a bulk fracture test), it is also expected a cohesive zone model can account for debonding and inelastic deformation occurring at the interface properly.

7.2. Nanomechanical and Nanotribological Characterization of Magnetic-mode Oxide Thin Films for Thermal Management

The nanomechanical properties of stoichiometric LCCO thin films grown on Si substrate using PLD technique were investigated using nanoindentation and nanoscratch techniques. X-Ray diffraction analysis revealed b-axis texturing in all films. The highest hardness obtained was 11.3 GPa. The lowest friction coefficient was ~0.1. It was found that LCCO thin films can be an attractive candidate as a nanothermal layer substituting for widely used DLC in a sense that these materials meet the demands that require sufficient thermal conductivity, modulus of elasticity, hardness and wear resistance, all of which are the critical factors in MEMS and hard disks.

It is required to investigate the nanomechanical properties of c-axis oriented LCCO thin films in the next step. It is expected that thermal conductivity as well as nanomechanical properties such as hardness and modulus will be changed with different crystalline orientation.

7.3. Effect of Roughness on the Contact of Microscale Thin-films: Experimental Study and Comparison with Existing Models

An experimental investigation was carried out using two different testers, namely, a dynamic stiffness tester and a nanoindentation tester with a flat-ended indenter to explore the contact of extremely smooth layered surfaces used in micromechanical applications. The experimental results have been compared with several existing contact models. It was found that the contact stiffness results for a thin film material which has compliant material on a stiffer substrate are closer to those of the GW model with asperity interaction effect in the elastic regime. When some asperities in the sample undergo plastic deformation, discrepancy was observed. For a better comparison, a contact model which accounts for plastic deformation of asperity as well as asperity interaction is needed. The contact stiffness results for a thin film material with a stiff top on a compliant substrate show that Yeo et al. model agrees with contact stiffness values obtained experimentally at extremely low loads. But at high contact load, the measured contact stiffness values are closer to those of GW with asperity interaction model.

An experimental approach measuring the contact stiffness between two contacting surfaces was very hard to carry out due to the difficulties in aligning the two surfaces to

make a perfect parallel contact. However, such measurements are likely to be of great importance in understanding the contact behavior of layered surface. The current experimental setup could be improved with the use of self-aligning device. One may fail to obtain an accurate result if a mechanical self-aligning device is used. A self-aligning device that involves compliant structures will change the contact stiffness values to be obtained. Therefore, it is recommended to use an electrical component such as a MEMS-based capacitive tilt sensor. To avoid the misaligning issue between the sensor and the sample, it is recommended to be fabricated together as one piece with the actual sample to be tested. It is expected that with the introduction of a tilt sensor, the initial tilt could be corrected, and stable measurements that is not affected by the initial contacting condition would be achieved. In addition, the effect of curvature or waviness of the sample needs to be considered in obtaining accurate results.

7.4. Wear Modeling and Analysis of Head Overcoat on Protruded Pole Tip due to Contact with Thermal Asperities

A finite element model was developed to simulate the sliding interaction between the protruded pole tip and a rigid asperity residing on a disk surface. The wear depth was obtained following a method suggested by Shankar et al. and using a wear coefficient was obtained experimentally by Machcha et al.. The obtained value of wear depth was unrealistically high. A new approach, termed deformed area of asperity and plastically deformed area of substrate was proposed. It was found that the wear behavior of the layered system under the sliding contact behavior was mainly dependent on the contact

force and elastic modulus of the substrate. These results were then incorporated into an Archard-type wear model, and a wear coefficient model was obtained. The wear coefficient values obtained from this study are higher than the typical wear coefficient values, because the wear area is estimated from the deformed area of asperity and plastically deformed area (which does not involve the actual removal of material). This clearly demonstrates that despite the most advanced computational techniques, direct linking between wear and material basic properties has been very difficult.

Future work will involve the development of a FEA model allowing actual detachment of wear particles for accurate prediction of wear behavior of a pole tip. For this, we can have a clue from Slack et al. on modeling spall formation. They realized material removal from FEA using the theory of damage mechanics (Slack et al., 2010).

7.5. Synthesis and Tribological Behavior of Hafnium Diboride Coatings

The tribological behavior of CVD-grown HfB_2 coatings was investigated. Nano mechanical properties of thin films deposited on a silicon substrate were measured including hardness, modulus, and surface roughness. Among a series of HfB_2 films, the highest hardness obtained was 36.5 GPa. The smoothest film has a roughness of 0.79 nm. An average friction coefficient value of ~0.5 was measured from meso scale pin on disk tests. Measured adhesion and shear strength from the nanoscratch tests for as-deposited films were 1.1 GPa and 4.5 GPa, respectively. It is found from the finite element analysis simulating nanoscratch that yielding at the interface was a dominant failure mechanism of hard hafnium diboride thin films.

It is expected that a quantitative description of growth of a crack initiated at the interface can be obtained with an introduction of energy release rate as an additional physical parameter of material behavior. For a full description of crack growth reaching the top coating layer from FEA, it is suggested to use cohesive elements for the coating layer with a proper assignment of properties such as fracture toughness and energy release rate.

Future work will involve the development of new coating materials such as Hf-B-N and synthesis of multilayer composites such as the repeat unit of HfB_2/HfB_xN_y. Measurement of hardness, elasticity and friction coefficient will be a good starting point estimating the tribological performance of new materials. However, a basic measurement of a developed material is not good enough to evaluate the tribological performance of new material. Hence, it is suggested to develop a new approaching method to find a critical factor that may affect the coating performance. This will be a challenging task including the understanding of the fundamental physical and chemical mechanisms that control the behavior of a coated surface. If this is successful, the tribological behavior of thin solid films will be predicted with the changes in parameters like coating thickness, hardness, modulus of elasticity, and adhesion strength at the interface.

Appendix: Calculation of Contact Stiffness from Different Analytical Models

A. Discrete Greenwood and Williamson (GW) model (Greenwood et al., 1966)

The original GW model has been developed to account for elastic contact of asperities using a statistical normal distribution. In this study, the single asperity model is implemented into a discrete GW rough surface contact model. A set of asperities is generated, which follows the normal (Gaussian) distribution and then the contact force F_{ci} of each asperity was determined from the Hertzian contact as follows:

$$F_{ci} = \begin{cases} \frac{4}{3} E^* R^{1/2} h_i^{3/2} & (\delta_i > 0) \\ 0 & (\delta_i \le 0) \end{cases} \tag{A.1}$$

where R is the average radius of asperities, h_i is the interference height of the each contacting asperity and E^* is the equivalent Young's modulus of elasticity given by

$$\frac{1}{E^*} = \frac{1-\nu_1}{E_1} + \frac{1-\nu_2}{E_2} \tag{A.2}$$

where E is the Young's modulus and ν is the Poisson's ratio. Subscript 1 and 2 denotes surface 1 and 2 respectively. The total contact force F_{tc} of the rough surfaces in contact is calculated by summing up all the contact forces of each asperity. Then the contact stiffness is obtained by differentiating the total contact force F_{tc} with respect to approach h, i.e.,

$$K_{c,GW} = \frac{dF_{tc}}{dh} \tag{A.3}$$

B. Discrete Greenwood and Williamson (GW) with asperity interaction model

The discrete GW model is extended to include the effect of asperity interaction. To account for asperity interaction, bulk deformation of the substrate is taken into account as Iida and Ono did (Iida et al., 2003). The bulk deformation of the substrate is obtained by the solution of Hertzian pressure on a circular region of an elastic half-space given by (Johnson, 1985)

$$U_z = \frac{F_c}{4\pi r_b^{\,3} E^*}\left[\left(2r_b^2 - r^2\right)\sin^{-1}\left(r_b / r\right) + r^2\left(r_b / r\right)\sqrt{\left(1 - r_b^2 / r^2\right)}\right], \quad (r \geq r_b) \tag{B.1}$$

where U_z is the normal displacement of neighboring asperities, r_b is the radius of an individual asperity sitting on the flat surface given by

$$r_{bi} = \sqrt{(2R - a_{hi}) \times a_{hi}} \tag{B.2}$$

where a_{hi} is the individual asperity heights. Then all interactions between asperities were calculated by adjusting the normal position of each asperity iteratively until equilibrated normal position of the surface is determined from all asperity interactions.

Once equilibrated normal position of the surface is obtained, interference height of each asperity in Eq. (A.1) is modified accordingly to get contact force for discrete GW with asperity interaction model and then contact stiffness $K_{c,GW\,w/int}$ for discrete GW with asperity interaction model can be obtained in the same manner as in Eq. (A.3).

C. Ciavarella, Greenwood and Paggi (CGP) model **(Ciavarella et al., 2006)**

The CGP model is an improved version of the GW model with the inclusion of interaction between asperities. In this model, asperity interaction is calculated by treating

the contact pressures from asperity contacts distributed uniformly over the apparent contact area resulting in the deformation ($=P_{nom}A^{1/2}/E^{*}$) of compacting area. The nominal pressure p_{nom} introduced by Greenwood and Williamson is

$$p_{nom} = \frac{4}{3}\eta E^{*} R^{1/2} \sigma^{3/2} F_{3/2}(\frac{d}{\sigma}) \tag{C.1}$$

where η is the asperity density, σ is the standard deviation of asperity heights, d is the separation between the rough surface and the contacting rigid plane, and $F_{3/2}$ is the function expressed as follows

$$F_{3/2}(h) \equiv \frac{1}{\sqrt{2\pi}} \int_{h}^{\infty} (s-h)^{3/2} \exp(-0.5s^{2}) ds \tag{C.2}$$

where s is the height of asperity measured from the mean of asperity heights. Hence, the effect of asperity interaction is to modify Eq. (C.1) to

$$p_{nom} = \frac{4}{3}\eta E^{*} R^{1/2} \sigma^{3/2} F_{3/2}(\frac{d}{\sigma} + \frac{p_{nom}\sqrt{A_n}}{E^{*}\sigma}) \tag{C.3}$$

where A_n is the nominal contact area. The obtained nominal pressure after solving iteratively in Eq. (C.3) can be used to get contact force and then contact stiffness $K_{c,CGP}$ for the CGP model can be calculated using the same method in Eq.(A.3)

D. Chang, Etsion and Bogy (CEB) model **(Chang et al., 1987)**

The CEB model is an elastic-plastic asperity contact model of rough surfaces whereas the GW model deals with elastic asperity contact. This model is based on volume conservation of an asperity control volume during plastic deformation. In this model, contact force of individual asperity in an elastic regime is same as shown in Eq.

(A.1). Contact force of individual asperity deformed plastically is given by the following equation

$$F_{ci} = \pi R\omega(2 - \frac{\omega_c}{\omega})KH \tag{D.1}$$

where ω is the interference, ω_c is the critical interference at the interception of plastic deformation and K is the maximum contact pressure factor. Contact stiffness $K_{c,CEB}$ for the CEB model can be acquired in a similar manner as in Eq. (A.3)

E. Yeo, Raja, Lee and Polycarpou (Yeo et al.) model **(Yeo et al., 2009; Yeo et al., 2010)**

The Yeo et al. model is the one that treats elastic contact of rough surface including the effect of asperity interaction. The reason that this analytical model is more unique than other contact models listed above is that it can be used when there is a stiffer layer on top of softer substrate. To account for the combined effect of thin film layer on bulk substrate, two springs in series concept are introduced. Elastic asperity deformation δ_a is expressed as a function of applied displacement and given by

$$\delta_a = \frac{\delta}{1 + \kappa\xi\sqrt{\frac{\delta}{1 + \kappa\xi\sqrt{\delta/(1+\kappa)}}}} \tag{E.1}$$

where κ is the physical parameter of the elastic modulus ratio between asperity and substrate, ξ is the geometrical parameter determining the asperity size.

The contact force for an individual asperity is calculated by Yeo et al. [11] and given by

$$F_{ci} = k \times \delta \tag{E.2}$$

where δ is the normal applied displacement and k is the combined asperity and bulk stiffness given by

$$k(\delta) = \left[\frac{1}{k_a(\delta)} + \frac{1}{k_b} \right]^{-1} \tag{E.3}$$

where k_a is the stiffness of asperity and k_b is the stiffness of substrate given by

$$k_a = 2\sqrt{R} E_a \sqrt{\delta_a} \tag{E.4}$$

$$k_b = \frac{4}{3} r_b E_b \tag{E.5}$$

respectively where E_a is the elastic modulus of asperity and E_b is the elastic modulus of bulk substrate. Using the contact force equation for an individual asperity in Eq. (E.2), the effect of asperity interaction is calculated in the same method used in appendix B.

Bibliography

Androulakis, J., Klini, A., Manousaki, A., Violakis, G., and Giapintzakis, J., 2004, "Growth of $LaNi_xCo_1$-xO_3 (x = 0.3, 0.5) thin films by pulsed laser deposition: possible candidate for electrodes in ferroelectric devices," *Applied Physics A*, **79**, p. 671.

Archard, J. F., 1953, "Contact and rubbing of flat surfaces," *Journal of Applied Physics*, 24 (8), pp. 981-988.

Ashcroft, I. A. and Derby, B., 1993, "Adhesion testing of glass-ceramic thick films on metal substrated," *Journal of Materials Science*, **28**, pp. 2989-2998.

Asif, S. A. S., Colton, R. J., and Wahl, K. J., 2001, "Nanoscale surface mechanical property measurements: force modulation techniques applied to nanoindentation," *ACS Symposium Series*, **781**, pp.198-215.

Athanasopoulos, G.I., Svoukis, E., Pervolaraki, M., Saint-Martin, R., Revcolevschi, R., and Giapintzakis, J., 2010, "Thermal conductivity of Ni, Co, and Fe-doped $La_5Ca_9Cu_{24}O_{41}$ thin films measured by the 3ω method," *Thin Solid Films*, **518**, pp. 4684-4687.

Benjamin, P., and Weaver C., 1960, "Measurement of adhesion of thin films," *Proceedings of the Royal Society A*, **254**, pp. 163-176.

Benz, M., Rosenberg, K. J., Kramer, E. J., and Israelachvili, J. N., 2006, "The deformation and adhesion of randomly rough and patterned Surfaces," *Journal of Physical Chemistry B*, **110**, pp. 11884-11893.

Berasategui, E. G., and Page, T. F., 2003, "The contact response of thin Si-C-coated silicon systems-characterisation by nanoindentation," *Surface and Coatings Technology*, **163-164**, pp.491-498.

Berger, M., and Hogmark, S., 2002, " Tribological properties of selected PVD coatings when slid against ductile materials," *Wear*, **252**, pp. 557-565.

Berger, M., and Hogmark, S., 2002, "Evaluation of TiB2 coatings in sliding contact against aluminum," *Surface and Coatings Technology*, **149**, pp.14-20.

Bhushan B., 2002, "Introduction to tribology," *Wiley*.

Bhushan, B., 2000, "Modern tribology handbook, Vol. II" *CRC Press*.

Black, E. J., Bain, J. A., and Schlesinger, T.E., 2007, "Thermal management in heat-assisted magnetic recording," *IEEE Transactions on Magnetics*, **43 (1)**, pp. 62-65.

Bowden, F. P., and Tabor, D., 1973, "An Introduction to Tribology," *Anchor Press/Doubleday*.

Buckle, H., 1965, "Mikroharteprufung und Ihre Anwendung," *Berliner Union Verlag*, Stuttgart.

Bull, S. J., and Rickerby, D. S., 1988, "The use of scratch adhesion testing for the determination of interfacial adhesion: The importance of frictional drag," *Surface and Coating Technology*, **36**, pp. 503-517.

Bull, S. J., 2005, "Nanoindentation of coatings," *Journal of Applied Physics*, **38**, R393-R413.

Castaing, J., and Costa, P., 1972,"Spin fluctuation effects in nearly antiferromagnetic vanadium and chromium diborides," *Journal of Physics and Chemistry of Solids*, **33**, pp. 533-547.

Chandross, M., Lorenz, C. D., Grest, G. S., Stevens, M. J., and Webb III, E. B., 2005, "Nanotribology of anti-friction coatings in MEMS," *Journal of the Minerals*, **57 (9)**, pp.55-61.

Chang, W. R, Etsion, I., and Bogy D. B., 1987, "An elastic-plastic model for the contact of rough surfaces, "*ASME Journal of Tribology*, **109**, pp.257-263.

Chatterjee, A., Jayaraman, S., Gerbi, J. E., Kumar, N., Abelson, J. R., Bellon, P., Polycarpou, A. A., and Chevalier, J. P., 2006,"Tribological behavior of hafnium diboride thin films," *Surface & Coating Technology*, **201**, pp. 4317-4322.

Chatterjee, A., Kumar, N., Abelson, J. R., Bellon, P., and Polycarpou, A. A., 2008, "Nanoscratch and nanofriction behavior of hafnium diboride thin films," *Wear*, **265**, pp. 921-929.

Chatterjee, A., Kumar, N., Abelson, J. R., Bellon, P., and Polycarpou, A. A., 2010, "Nanowear of hafnium diboride thin films," *Tribology Transactions*, **53**, pp. 731-738.

Chatterjee, A., Polycarpou, A. A., Abelson, J. R., and Bellon, P., 2010, "Nanoscratch study of hard HfB_2 thin films using experimental and finite element techniques, " *Wear*, **268**, pp. 677-685.

Ciavarella, M., Greenwood, J. A., and Paggi, M., 2008, "Inclusion of "interaction" in the

Greenwood and Williamson contact theory," *Wear*, **265**, pp.729-734.

Colaco, R., 2009, "An AFM study of single-contact abrasive wear: the Rabinowicz wear equation revisited," *Wear*, **26**7, pp. 1772-1776.

Cui, Z., Dixit, G., Xia L.-Q., Demos, A., Kim, B. H., Witty, D., M'saad, H. and Dauskardt R. H., 2005, "Benchmarking four point bend adhesion testing: the effect of test parameters on adhesion energy," *AIP conference proceedings*, **788**, p. 507.

Cumpson, P. J., Hedley, J., and Zhdan, P., 2003, "Accurate force measurement in the Atomic force microscope: a microfabricated array of reference springs for easy cantilever calibration," *Nanotechnology*, **14**, pp.918-924.

D'Haen, J, Quaeyhaegens, C.. and Stals, L. M., 1993, "Interface study of physical vapour deposition TiN coatings on plasma-nitrided steels," *Surface and Coatings Technology*, **61**, pp.194-200.

Dauskardt, R. H., Lane, M., Ma, Q.. and Krishna, N., 1998, "Adhesion and debonding of multi-layer thin film structures," *Engineering Fracture mechanics*, **61**, pp. 141-162.

Diao, D. F., Kato, K.. and Hayashi, K., 1992, "The local yield map of hard coating under sliding contact," *Proceedings of the 19th Leeds-Lyon Symposium*.

Eid, H., and Adams, G. G., 2007, "An elastic-plastic finite element analysis of interaction asperities in contact with a rigid flat," *Journal of Physics D: Applied Physics*, **40**, pp.7432-7439.

Faulkner, A., and Arnell, R. D., 2000, "The development of a finite element model to simulate the sliding interaction between two, three-dimensional, elastoplastic, hemispherical asperities," *Wear* **242**, pp. 114-122.

Ferrari, A. C., 2004, "Diamond-like carbon for magnetic storage disks," *Surface and Coating Technology*, **180-181**, pp. 190-206.

Gage, D. M., Kim, K., Litteken, C. S., and Dauskardt, R. H., 2005, "Effects of friction and loading parameters on four-point bend adhesion measurements of low-k thin film interconnect structures," *Proceedings of the IEEE 2005 International*, pp. 42-44.

Gao, H., and Wu, T., 1993, "A note on the elastic contact stiffness of a layered medium," *Journal of Material Research*, **8 (12)**, pp. 3229-3232.

Gardelis, S., Androusakis, J., Giapintzakis, J., and Buckle, P. D., 2004, "Structural,

magnetic and transport properties of NiMnSb thin films grown on InSb by pulsed laser deposition," *Applied Physics Letters*, **85**, p. 3178.

Goerke, D., and Willner, K., 2008, "Normal contact of fractal surfaces-experimental and numerical investigations," *Wear*, **264 (7-9)**, pp.589-598.

Goglia, P. R., Berkowitz, J., Hoehn, J., Xidis, A., and Stover, L., 2001,"Diamond-like carbon applications in high density hard disc recording heads, " *Diamond and Related Materials*, **10 (2)**, pp.271-277.

Gong, Z.-Q., and Liu J. J., 2005, "Pole-tip protrusion effect on head–disk interface at low flying clearance," *IEEE Transactions on Magnetics*, **41 (10)**, pp. 3019-3021.

Green I., 2005, "Poisson ratio effects and critical valus in spherical and cylindrical hertzian contacts," *International Journal of applied mechanics and engineering*, **10 (3)**, pp. 451-462.

Greenwood, J. A., and Williamson, J. B. P, 1966, "Contact of nominally flat surfaces," *Proceedings of the Royal Society A*, **295**. pp. 300-319.

Gui, J., 2003, "Tribology challenges for head-disk interface toward 1 TB/in2," *IEEE Transactions on Magnetics*, **39 (2)**, pp. 716-721.

Gupta, B. K., Young, K., Chilamakuri, S., and Menon, A. K., 2000, "Head design considerations for lower thermal pole tip recession and alumina overcoat protrusion," *Tribology International*, **33**, pp. 309-314.

Gupta, P. K., and Walowit, J. A., 1974, "Contact stresses between an elastic cylinder and layered elastic solid," *Journal of Lubrication Technology*, **96**, pp. 250-257.

Gupta, P. K., Walowit, J. A. and Finkin, E. F., 1973,"Stress distribution in plane strain layered elastic solids subjected to arbitrary boundary loading," *Journal of Lubrication Technology*, **95**, pp. 427-433.

Hamilton, G. M., and Goodman, L. E., 1966, "The stress field created by a circular sliding contact," *Journal of Applied Mechanics*, **33**, pp. 371-376.

Hamilton, H., Goodsen, K., Baldwin, C., and Anderson, R., 1992, "Contact perpendicular recording with integrated head/flexure," *Concepts in Contact Recording*, **TRIB-3**, pp. 13–23.

Hanchi, J., Polycarpou, A. A., and Boutaghou, Z., 1999, "Tribology of contacting head-

disk interfaces," in Proceedings, *Symposium Interface Tribology Towards 100 Gb/in2*, **Trib. 9**, pp.17–22.

Hara, H., Sugi, S., Akita, T., and Yokota, K., 1998, "A study on read-back signal degradation of a pseudo-contact head during seek motion of a hard disk drive," *Tribology Letters*, **5**, pp. 275-282

Harris, S. J., Weiner, A. M., and Meng W.-J., 1997, "Tribology of metal-containing diamond-like carbon coatings," *Wear*, **211**, pp. 208-217.

Heinze, M., 1998, "Wear resistance of hard coatings in plastics processing," *Surface and Coating Technology*, **105**, pp.38-44.

Herr, W., and Broszeit, 1997, "Effect of an annealing process on the tribological properties of sputtered hard coating," *Surface and Coating Technology*, **97**, pp. 669-674.

Hess, C., Baumann, C., Ammerashl., Buchner, B., Hiedrich-Meisner, F., Brenig, W., and Revcolevschi, A., 2001,"Magno heat transport in (Sr, Ca, La)$_{14}$Cu$_{24}$O$_{41}$," *Physical Review B*, **64**, 184305.

Höling, A., Hultman, L., Odén, M., Sjölén, J., and Karlsson, L., 2005, "Mechanical properties and machining performance of $Ti_{1-x}Al_xN$-coated cutting tools," *Surface and Coating Technology*, **191 (2-3)**, pp. 384-392.

Holmberg, K. and Matthews, A., 1994, "Coating tribology: Properties, mechanisms, techniques and applications in surface engineering," *Tribology and Interface Engineering Series*, **56**, Elsevier.

Holmberg, K., Matthews, A. and Ronkainen, H., 1998,"Coating tribology-contact mechanisms and surface design," *Tribology International*, **31 (1-3)**, pp. 107-120.

Holmberg, K., Ronkainen, H. and Matthews, A., 2000, "Tribology of thin coatings," *Ceramics International*, **26**, pp. 787-795.

Hu, J., Xiao X.-D., Ogletree, D. F., and Salmeron, M., 1995, "Imaging the condensation and evaporation of molecularly thin films of water with nanometer resolution," *Science*, **268** (5208), pp. 267-269.

Hugel, T., and Seitz, M., 2001, "The study of molecular interactions by AFM force spectroscopy," *Macromolecular Rapid Communications*, **22**, pp. 989-1016.

Iida, K., and Ono, K., 2003, "Design consideration of contact/near-contact sliders based

on a rough surface contact model," *Transactions of the ASME*, **125**, pp. 562-570.

Imbeni, V., Martini, C., Lanzoni, E., Poli, G., and Hutchings, I. M., 2001, "Tribological behavior of multi-layered PVD nitride coatings," *Wear*, **251**, pp. 997-1002.

Israelachvili, J. N., 1985, "Intermolecular and surface forces," *Academic Press*, New York.

Jayaraman, S., Gerbi, J. E., Yang, Y., Kim, D. Y., Chatterjee, A., Bellon, P., Girolami, G. S., Chevalier, J. P., and Abelson, J. R., 2006, "HfB_2 and Hf-B-N hard coatings by chemical vapor deposition," *Surface and Coating Technology*, **200**, pp. 6629-6633.

Jayaraman, S., Yang, Y., Kim, D. Y., Girolami, G. S., and Abelson, J. R., 2005, "Hafnium diboride thin films by chemical vapor deposition from a single source precursor," *Journal of Vacuum Science and Technology A*, **23 (6)**, pp. 1619-1625.

Jhi, S.-H., Ihm, J, Loule, S.G., and Cohen, M.L., 1999, "Electronic mechanism of hardness enhancement in transition-metal carbonitrides," *Nature*, **399 (6732)**, pp. 132-134.

Johnson, K. L., 1985, "Contact Mechanics," *Cambridge University Press*, Cambridge.

Ju, Y., and Linquing, Z., 1992, "A full numerical solutions for the elastic contact of three-dimensional real rough surfaces," *Wear*, **157**, pp. 151-161.

Kendall, K., 1994, "Adhesion: molecules and mechanics," *Science*, 263 (5154), pp. 1720–1725.

Kennedy, F. E., and Ling, F. F., 1974,"Elastic-plastic indentaion of a layered medium," *Journal of Engineering Materials and Technology*, **96**, pp. 97-103.

Kieffer, R., and Benesovsky, F., 1963, "Harstoffe," *Springer-Verlag*.

King, R. B., 1987, "Elastic anlaysis of some punch problems for a layered medium," *International Journal of Solids Structures*, **23 (12)**, pp. 1657-1664.

Kogut, L., and Etsion, I., 2002, "Elastic-plastic contact analysis of a sphere and a rigid flat," *ASME Journal of Applied Mechanics*, **69**, pp.657-662.

Komvopoulos, K., 1988, "Finite element analysis of a layered elastic solid in normal contact with a rigid surface," *Journal of Tribology*, **110**, pp.477-485.

Konca, E., Cheng Y.-T., Weiner, A. M., Dasch, J. M., Erdemir, A., and Alpas, A. T., 2005, "Transfer of 319 Al alloy to titanium diboride and titanium nitride based (TiAlN, TiCN, TiN) coatings: effects of sliding speed, temperature and environment," *Surface and Coating Technology*, **200**, pp. 2260-2270.

Laugier, M. T., 1984, "An energy approach to the adhesion of coatings using the scratch test," *Thin Solid Films*, **117**, pp.243-249.

Lee, S. C., and Polycarpou, A. A., 2004, "Adhesion forces for Sub-10nm flying-height magnetic storage head disk interfaces," *ASME Journal of Tribology*, **126**, pp. 334-341.

Lee, S.C., and Polycarpou, A.A., 2004, "Tri-state dynamic model and adhesive effect on flying-height modulation for ultra-low flying head disk interfaces," *Microsystem Technology*. **10**, pp. 649-661.

Li, H., Liu, B., and Chong T.-C., 2006, "Interface solution for writing-induced nano-deformation of slider body," *Journal of Magnetism and Magnetic Materials*, **303**, pp. e86-e90.

Li, X., and Bhushan, B., 2000, "Development of continuous stiffness measurement technique for composite magnetic tapes," *Scripta Materialia*., **42**, pp. 929-935.

Li, Y., and Menon, A. K., 1994, "A theoretical analysis of breakaway friction measurement," *ASME Journal of Tribology*, **116 (2)**, pp. 280-286.

Liu, B., Liu, J., and Chong T.-C., 2005, "Slider design for sub-3nm flying height head-disk systems," *Journal of Magnetism and Magnetic Materials*, **287**, pp. 339-345.

London F., 1936, "The General Theory of Molecular Forces," *Transactions of the Faraday Society*.

Luo, J. F., Liu, Y. J. and Berger, E. J., 2000, "Interfacial stress analysis for multi-coating systems using an advanced boundary element method," *Computational Mechanics*, **24**, pp. 448-455.

Machcha, A. R., Azarian M. H. and Talke F. E., 1996, "An investigation of nano-wear during contact recording," *Wear*, **197**, pp. 211-220.

Malzbender, J., den Tooder, J. M. J., Balkenende, A. R., and de With, G., 2002, "Measuring mechanical properties of coatings: a methodology applied to nano-particle-filled sol-gel coatings on glass," *Materials Science and Engineering*, **R 36**, pp.47-103.

McCool, J. I., 2000, "Extending the capability of the Greenwood Williamson microcontact model," *ASME Journal of Tribology*, **122**, pp. 496-502.

Mittal, K. L., 1976, "Adhesion measurement of thin films," *Electrocomponent Science and Technology*, **3**, pp. 21-42.

Mitterer, C., 1997, "Borides in thin film technology," *Journal of solid state chemistry*, **133**, pp. 279-291.

Mitterer, C., 2008, "Metastable transition metal nitride coatings for wear protection," Scitopics.

Morales, P., DiCiano, M., and Wei, J. Y. T., 2005, Selective epitaxial growth of submicron complex oxide structures by amorphous $SrTiO_3$," *Applied Physics Letters*, **86**, p. 192509.

Oliver, W.C., 1992, "An improved technique for determining hardness and elastic modulus using load and displacement sensing indentation experiments," *Journal of Materials Research*, **7 (6)**, pp.1564-1583.

Ono, K., Iida, K., and Takahashi, K., 1999, "Effects of design parameters on bouncing vibrations of a single-DOF contact slider and necessary design conditions for perfect contact sliding," *ASME Journal of Tribology*, **121**, pp. 596-603.

Pervolaraki, M., Athanasopoulos, G. I., Saint-Martin, R., Revcolevschi, A., and Giapintzakis, J., 2009, "KrF pulsed laser deposition of La5Ca9Cu24O41 thin films on various substrates," *Applied Surface Science*, **255**, pp. 5236-5239.

Pervolaraki, M., Singh, S., Athanasopoulos, G. I., Saint-Martin, R., Revcolevschi, A., and Giapintzakis, J., 2010, "Pulsed laser deposition of homo- and hetero-epitaxial thin films of the exotic $La_5Ca_9Cu_{24}O_{41}$ compound on oxide and Si substrates," *Journal of Optoelectronics and Advanced Materials*, **12 (3)**, pp. 641-645.

Podra, P., and Andersson, S., 1999, "Simulating sliding wear with finite element method," *Tribology International*, **32**, pp. 71-81.

Polonsky, I. A., and Keer, L. M., 2000, "A fast and accurate method for numerical analysis of elastic layered contacts," *Transactions of the ASME*, **122**, pp. 30-35.

Pullen, J., and Williamson, J. B. P., 1972, "On the plastic contact of rough surfaces," *Proceedings of the Royal Society A*, **327**, pp. 159-173.

Rigney, D.A., 1988, "Sliding wear of metals," *Annual Review of Materials Research*, **18**, pp. 141-163.

Salib, J., Kligerman, Y., and Etsion, I., 2008, "A model for potential adhesive wear particle at sliding inception of a spherical contact," *Tribology Letters*, **30**, pp. 225-233.

Schuh, C. A., Packard, C. E., and Lund, A. C., 2006, "Nanoindentation and contact-mode imaging at high temperatures," *Journal of Materials Research*, **21 (3)**, pp. 725-736.

Serpe, C. I., 1999, "The role of contact compliance in the deformation, wear and elastic stability of metallic sliding rings: Experiments and computational analysis," *Ph. D. Dissertation, State University of New York at Buffalo*, NY.

Shankar, S., and Mayuram, M. M., 2008, "Sliding interaction and wear studies between two hemispherical asperities based on finite element approach," *International Journal of Science and Engineering*, **2**, pp. 71-83.

Shi, X., 2005, "Fundamental modeling and experimental investigation of dynamic friction at the meso and micro scales," *Ph. D. Dissertation, University of Illinois at Urbana-Champaign*.

Shi, X., and Polycarpou, A. A., 2005, " An elastic-plastic hybrid adhesion model for contacting rough surfaces in the presence of molecularly thin lubricant," *Journal of Colloid and Interface Sciences*, **290 (2)**, pp. 514-525.

Shi, X., and Polycarpou, A. A., 2005, "Measurement and modeling of normal contact stiffness and contact damping at the meso scale," *Journal of Vibration and Acoustics*, **127 (1)**, pp. 52-60.

Shi, X., and Polycarpou, A.A., 2009, "Investigation of contact stiffness and contact damping for magnetic storage head-disk interfaces," *ASME Journal of Tribology*, **130**, pp. 1-9.

Slack, T., and Sadeghi F., 2010, "Explicit finite element modeling of subsurface initiated spalling in rolling contacts," *Tribology International*, **43 (9)**, pp. 1693-1702.

Sologubenko, A. V., Gianno, K., and Ott, H. R., 2001, "Heat transport by lattice and spin excitations in the spin-chain compounds $SrCuO_2$ and Sr_2CuO_3," *Physical Review B*, **64**, 054412.

Solzak, T. A. and Polycarpou, A. A., 2006, "Tribology of WC/C coatings for use in oil-less piston-type compressors," *Surface and Coatings Technology*, **201**, pp. 4260-65.

Solzak, T. A., and Polycarpou, A. A., 2010, "Tribology of hard protective coatings under realistic operating conditions for use in oil-less piston-type and swashplate compressors," *Tribology Transactions*, **53 (3)**, pp. 319-328.

Song, D., Kvitek, R., and Schnur, D., 2006, "Inspection of pole tip diamondlike carbon wear due to heater-induced head-disc contact," *Journal of applied Physics*, **99**, 08N107.

Sourty, E., Sullivan, J. L., and Bijker, M. D., 2003, "Chromium oxide coatings applied to magnetic tape heads for improved wear resistance," *Tribology International*, **36**, pp. 389-396.

Spence, D. A., 1975, "The Hertz contact problem with finite friction," *Journal of Elasticity*, **5**, pp. 297-319.

Suh, A. Y., and Polycarpou, A. A., 2003, "Adhesion and pull-off forces for polysilicon MEMS surfaces using the sub-boundary lubrication model," *ASME Journal of Tribology*, **125**, pp. 193-199.

Suh, A. Y., Lee, S. C., and Polycarpou, A. A., 2004, "Adhesion and friction evaluation of textured slider surfaces in ultra-low flying head-disk Interfaces," *Tribology Letters*, **17 (4)**, pp. 739-749.

Suh, A. Y., and Polycarpou, A.A., 2006, "Digital filtering methodology used to reduce scale of measurement effects in roughness parameters for magnetic storage supersmooth hard disks," *Wear*, **260 (4-5)**, pp.538-548.

Suk, M., Dennig, P., and Gillis, D., 2000, "Magnetic erasures due to impact induced interfacial heating and magnetostriction," *Journal of Tribology*, **122**, pp. 264-268.

Suk, M., Miyake, K., Kurita, M., Tanaka, H., Saegusa, S., and Robertson,N., 2005, "Verification of thermally induced nanometer actuation of magnetic recording Transducer to overcome mechanical and magnetic spacing challenges," *IEEE Transactions on Magnetics*, **41 (11)**, pp. 4350-4352.

Sun, Y., Bloyce, A., and Bell, T., 1995, "Finite element analysis of plastic deformation of various TiN coating/substrate systems under normal contact with a rigid sphere," *Thin Solid Films*, **271**, pp.122-131.

Suzuki, M., Watanabe, T., Tanaka, A., and Koga, Y., 2003, "Tribological properties of diamond-like carbon films produced by different deposition techniques," *Diamond and Related Materials*, **12**, pp. 2061-2065.

Suzuki, S., and Kennedy, F.E. Jr., 1989, "Measurement of flash temperature and contact between slider and magnetic Recording disk," *IEEE Transactions on Magnetics*, **25**, pp. 3728-3730.

Tabor, D., 1951, "The hardness of metals," Oxford University Press.

Tan, M., Yan, Y., Zhang, H., Han, X., Zhu, J., Han, J., and Ma, H., 2009, "Corrosion protection of ultra-thin ta-C films for recording slider applications at varied substrate bias," *Surface and Coating Technology*, **203**, pp. 963-966.

Tayebi, N., and Polycarpou, A. A., 2005, "Reducing the effects of adhesion and friction in microelectromechanical Systems (MEMS) through surface roughening: comparison between theory and experiments," *Journal of Applied Physics*, **98 (7)**, 073528.

Timoshenko, S., and Goodier, J. N., 1951, "Theory of elasticity," *McGraw-Hill*, New York.

Tran, P., Kandula, S. S., Geubelle, P. H. and Sottos, N. R., 2011, "Comparision of dynamic and quasi-static measurements of thin film adhesion," *Journal of Applied Physics*, **44**, 034006.

Vijay, P., and Talke, F. E., 2000, "Wear and hardness of carbon overcoats on magnetic recording sliders, *Wear*, **243**, pp. 18-24.

Voevodin, A. A., Walck, S. D. and Zabinski, J. S., 1997, "Architecture of multilayer nanocomposite coatings with super-hard diamond-like carbon layers for wear protection at high contact loads," *Wear*, **203-204**, pp.516-527.

Williams, J. A., 2005, "Wear and wear particles-some fundamentals," *Tribology International*, **38**, pp. 863-870.

Wood, R., 2000, "The feasibility of magnetic recording at 1 terabit per square inch," *IEEE Transactions on Magnetics*, **36 (1)**, pp. 36-42.

Xue, X., and Polycarpou, A. A., 2007, "An improved meniscus surface model for contacting rough surfaces," *Journal of Colloid and Interface Science*, **311**, pp. 203-211.

Yeack-Scranton, C.E., Kahnna, V.D., Etzold, K.F., and Praino A.P., 1990, "An active slider for practical contact recording," *IEEE Transactions on Magnetics*, **26 (5)**, pp. 2478-2483.

Yeo, C.-D., Katta, R. R., Lee J., Polycarpou, A. A., 2010, "Effect of asperity interactions on rough surface elastic contact behavior: hard film on soft substrate," *Tribology International*, **43 (8)**, pp. 1438-1448.

Yeo, C.-D., Lee, S.-C., and Polycarpou, A. A., 2008, "Dynamic adhesive force measurements under vertical and horizontal motions of interacting rough surfaces," *Review of Scientific Instruments*, **79**, 015111

Yeo, C.-D., 2008, "Rough surface interactions at micro/nano-scale contact systems," *Ph.D. Thesis, University of Illinois at Urbana-Champaign*.

Yeo, C.-D., Sullivan, M., Lee, S.-C., and Polycarpou, A. A., 2008, "Friction force measurements and modeling in hard disk drives," *IEEE Transactions on Magnetics*, **44 (1)**, pp.157-162.

Yoder, K.B., Stone, D. S., Hoffman, R. A., and Lin, J. C., 1998, "Elastic rebound between an indenter and a layered specimen: part II. using contact stiffness to help ensure reliability of nanoindentation measurements," *Journal of Materials Research*, **13 (110)**, pp. 3214-3220.

Yu, N., Bonin, W. A., and Polycarpou, A. A., 2005, "High-resolution capacitive load-displacement transducer and its application in nanoindentation and adhesion force measurements," *Review of Scientific Instruments*, **76 (4)**, 045109.

Yu, N., Polycarpou, A. A., and Hanchi, J. V., 2008, "Elastic contact mechanics-based contact and flash temperature analysis of impact-induced head disk interface damage," *Microsystem Technologies*, **24**, pp. 215-227.

Yu, N., and Polycarpou, A.A., 2010, "Thermomechanical finite element analysis of slider-disk impact in magnetic storage thin film disks," *Tribology International*, **43 (4)**, pp. 737-745.

Zhao, Y., and Chang, L, 2001, "A model of asperity interactions in elastic-plastic contact of rough surfaces," *ASME Journal of Tribology*, ***123***, pp. 857-64.

Zhou, L., Kato, K., Umehara, N., and Miyake, Y., 2000, "Friction and wear properties of hard coating materials on textured hard disk sliders," *Wear*, **243**, pp. 133-139.